HYBRID INERTIAL MICROWAVE REFLECTOMETRY FOR MM-SCALE TRACKING IN RFID SYSTEMS

A Dissertation
Presented to
The Academic Faculty

by

Muhammad B. Akbar

In Partial Fulfillment
of the Requirements for the Degree
Doctor of Philosophy in the
School of Electrical and Computer Engineering

Georgia Institute of Technology
August 2016

HYBRID INERTIAL MICROWAVE REFLECTOMETRY FOR MM-SCALE TRACKING IN RFID SYSTEMS

Approved by:

Professor Gregory D. Durgin, Advisor
School of Electrical and Computer Engineering
Georgia Institute of Technology

Professor Paul G. Steffes
School of Electrical and Computer Engineering
Georgia Institute of Technology

Professor David G. Taylor
School of Electrical and Computer Engineering
Georgia Institute of Technology

Professor Neal Patwari
School of Electrical and Computer Engineering
University of Utah

Professor Andrew F. Peterson
School of Electrical and Computer Engineering
Georgia Institute of Technology

Date Approved: 16 June 2016

To my parents, siblings and,

To Kalsoom, Eshaal, and Enaya.

ACKNOWLEDGEMENTS

First of all, I sincerely thank Almighty Allah for all His blessings, especially the opportunity and strength to achieve this milestone in life.

I want to thank my advisor, Prof. Gregory Durgin, for his support, encouragement, wisdom and guidance at every single step to make this journey possible. I learned a great deal from him, not just about the research that we worked on, but also about the steps one needs to take in order to formulate and solve problems in general. He considers all of his students part of his family and goes out of the way to assist them in any problem they face. In this sense, he taught me by leading by example, and for that, I'm grateful.

I would also like to thank Prof. David Taylor for teaching me about some fundamental topics in Systems and Controls, and for his worthy help in my research. I am extremely grateful to my other committee members, Prof. Andrew Peterson, Prof Paul Steffes, and Prof. Neal Patwari for their time, helpful comments, and valuable feedback.

I owe a great deal of thanks to my colleagues from the Propagation Group for their support and assistance throughout my work. James Steinberg and Kevin Pham, two outstanding personalities of ECE department, deserve special mention for their extraordinary support and cheerful helping attitude. I also thank all my friends from Paksitan House and from Pakistani community at Georgia Tech for making my life in US joyful and colorful.

Finally, I am grateful to most valuable people of my life: my parents, wife, siblings, and kids. There is no way to acknowledge and thank them for their countless support and prayers. Their sacrifice and patience is the greatest cost of my education at Tech.

Especially, I am highly indebted to my wife and children, for their unconditional support, patience and tolerance of my mood swings and unusual working routines during the entire duration of my PhD. Kalsoom, Eshaal, and Enaya, it became possible only with your affectionate help and support.

TABLE OF CONTENTS

LIST OF TABLES

LIST OF FIGURES

SUMMARY

Despite the numerous wireless position estimation schemes in the patent and research literature, motion capture grade localization with RF has eluded engineering practice. Motion capture localization with cm-scale accuracy or better is typically performed optically, with limited range, high setup time, and environmental limitations (e.g. infrared systems that do not work outdoors). Today's true RF-based motion capture technology involves sensing low-frequency or DC fields using bulky sensor boxes – with ranges of only a few meters. In this work, we achieved long-range, motion-capture grade localization with extraordinarily low-powered HIMR tags.

Localization and tracking are some of the most important applications of RFID technology. This work proposes a new fine-scale (millimeter level) radio localization and tracking scheme—Hybrid Inertial Microwave Reflectometry (HIMR)—for radio frequency identification and other wireless systems. The scheme fuses the information from the backscattered radio frequency signal properties, such as received signal strength and received signal phase, along with reflected inertial data from a tag-mounted, 9-axis inertial sensor to yield millimeter level localization accuracy. Experimental results yielded a positional accuracy in the range of 2 mm and 20 mm, respectively, for one- and two-dimensional tracking of a fast-moving tag. The HIMR-scheme does not require reference tags or external system for localization, instead all the information is extracted from the RFID-based radio link and fused in novel HIMR-algorithm without performing mathematical integration or differentiation to achieve position and tracking.

CHAPTER I

RESEARCH REVIEW

The objective of the this research is to develop a new fine-scale (millimeter level) radio localization and tracking scheme (L&T) – Hybrid Inertial Microwave Reflectometry (HIMR) – for radio frequency identification (RFID) and other wireless systems. The scheme makes use of RF signal properties such as received signal phase and received signal strength (RSS) along with reflected inertial data from a low-cost, low-power, tag-mounted 9-axis inertial sensor. It will be demonstrated that this scheme yields millimeter level accuracy as compared to conventional techniques. Conventional techniques for tracking of tagged-objects yield a tracking accuracy between 0.1 to 5 meters while HIMR-based position estimation results in accuracies as low as 3 mm. Unlike most RFID location tracking techniques [6–43, 49], HIMR does not require reference tags and third-party radio sources. Instead, all the information is retrieved from a single radio link. The accuracy results demonstrated in this work suggest the possibility for a 3D *motion capture grade* tracking system based on RF rather than DC, magnetoquasistatic, or optical techniques [50–52].

The proposed HIMR-based localization method relies on an RFID system that works in the 5.725 - 5.875 GHz Industrial, Scientific and Medical (ISM) frequency band but can also be extended in other RF frequency bands. HIMR can be applied for precise robotic wayfaring, remote motion capture, and tracking on a sports field. Used in a sports helmet or other head-mounted device, the nature and position of traumatic brain injury due to concussions could be diagnosed. Such fine-scale motion capture could also enhance the gaming industry by incorporating virtual reality – places where traditional radio L&T and motion capture systems do not function well

due to range and/or accuracy limitations.

1.1 Basic Methods for Position Estimation

Most of the basic methods for position estimation utilize triangulation or trilateration approach to estimate the position. The triangulation approach is illustrated in Figure 1, where the location of the target is approximated by the intersection of two or more incident angles measured at the reference points [6]. The trilateration approach is depicted in Figure 2, where the location of the target is estimated by the intersection of three or more circles. These circles are formed by evaluating the target object's distance using its received signal strength or time-of-flight information [6]. The fundamental methods for localization of objects are listed below [1, 6, 7, 53].

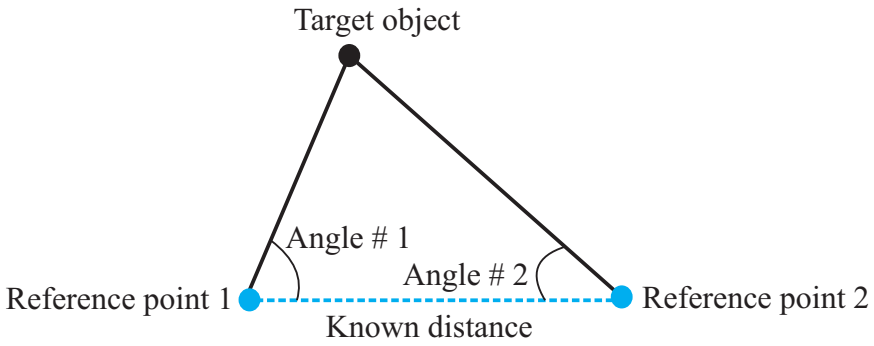

Figure 1: In the triangulation approach the location is estimated by the intersection of the angles formed between the reference points and the target object [6].

1 **Time-of-Arrival (TOA) Estimation** Time-of-arrival (TOA) allows the measurement of an object distance by combining the signals from three or more base nodes. In TOA, it is assumed that the position of the base nodes is known and all nodes have synchronized clocks. The transmitted signal from the target is labeled with a time stamp to determine the time at which the signal originated from the target node. In addition, this technique requires line of sight (LOS) for minimal error.

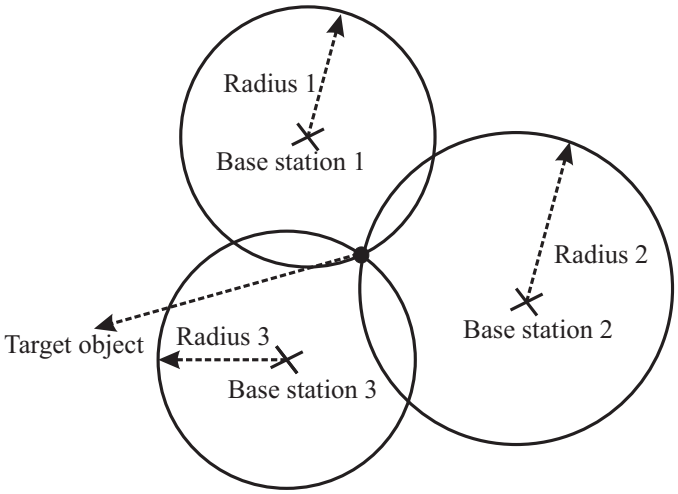

Figure 2: In the trilateration approach the location is estimated by intersection of the three or more circles formed by evaluation of the target object's distance using its received signal strength [6].

2 **Time Difference of Arrival (TDOA) Estimation** TDOA computes the difference of the arrival time of signals at the base nodes with known locations. The base station that first receives the signal is considered as the reference node while the measurements at the subsequent base stations are made with respect to the reference base station. Unlike TOA, this technique does not require the time synchronization of the target node with the base nodes, however, clocks for all base nodes are synchronized. In this technique, the transmitted signal also does not require to time stamp its transmission making signal transmission less complex and works best in LOS scenario.

3 **Angle-of-Arrival (AOA) Estimation** In this technique, base nodes determine the angle-of-arrival by using the triangulation approach. Similar to the TOA and TDOA, the base nodes locations are known apriori. Each node is equipped with antenna arrays and RF front end resulting in higher costs, higher power consumption, and complexity. AOA estimation is also sensitive to the availability of clear LOS.

4 **Received Signal Strength (RSS) Estimation** In an RSS estimation, the signal strength of the received signal is measured to compute the distance covered by the signal. Better results are achieved if multiple base nodes cooperate to localize a target via trilateration. This technique works in both LOS and Non-LOS (NLOS) scenarios.

5 **Return Time of Flight (RTOF) Measurements** RTOF measurements follow the path of direct distance measurement using two-way communication between the units. One unit sends an interrogating signal to one or more units in range and they reply with their independent ID encoded in the signal to estimate the distance using round-trip TOF.

1.2 Overview of Position Estimation Systems

There are many position estimation systems that employ the aforementioned localization methods. Some of the systems are explained below:

1 **Global Positioning System (GPS)** The GPS is based on 27 medium earth orbiting satellites at a height of 20,200 km from the earth's surface. Using these satellites, a person or an object can determine its position in terms of latitude, longitude, and altitude. GPS can be used for many navigational applications but it is not capable of positioning inside buildings and mines. GPS performance is also severely affected in scattering environments such as urban areas. Further details on the operation of GPS can be found in [2]. GPS has a very expensive infrastructure and complex communication protocols.

2 **Inertial Navigation System (INS)** The INS positioning system uses inertial motion sensors, accelerometers and gyroscopes, to track the position, velocity and orientation of an object relative to a known initial conditions. The new position, velocity, and orientation is computed by integrating the information

obtained from inertial sensors. The inertial motion sensors measurements may contain noise or offset error. When integrating these quantities, the errors in the measured values are propagated to the subsequently calculated position and orientation values. The localization error can be adjusted to zero by a merger of the INS with other positioning systems such as GPS. [1].

3 **Radio Frequency Identification System (RFID)** The RFID is a wireless system that identifies tags attached to an object of interest. An RFID system consists of a reader and RFID tags. The RFID systems are divided in three categories, according to whether they use *passive*, *semi-passive*, or *active* tags [54]. *Passive* RFID tags are activated by rectifying and harvesting the power from the incident RF signal, and are suitable for short range applications. An *active* RFID tag is a full transceiver system including RF front end, processors, antennas, and a power source. A *semi-active* tag does not contain RF front end or signal rectifying and power harvesting circuitry; instead, it is battery powered and suitable for long range applications as compared to a *passive* tag. An RFID system can be used to localize the position of a target object as shown in the literature [6–43, 49]. These systems are relatively inexpensive as compared to the other systems.

4 **Wireless Local Area Network (WLAN)** The WLAN is used for position estimation and identification of objects in a limited range by using RSSI to localize the position of an object. The strength of the signal that a wireless device or target object sends out is measured at multiple receivers to calculate the position. The WLAN position estimation system consists of base stations and mobile nodes. Mobile nodes periodically broadcast time stamped packets, while a base station records the received signal strength, time difference between signal transmission and reception, and base station identification. Using this

information, the location is determined by combining empirical measurements with signal propagation models [3].

5 **Vision-based Localization System** In vision based localization system, two or more cameras are used to localize the target object. Assuming that the distance between the cameras and the focal length of the cameras is known, the distance of the object from the lens plane of the cameras can be calculated. Given known positions of the cameras and the calculated distance, the target object can be localized [4].

6 **Radar** The Radar is used to localize the position of a target (typically an aircraft) in the surrounding areas by transmitting a short burst of energy and processing its reflection from the target. Radar estimates the distances by computing the round trip time of the short energy burst which reflects off the surface of the target and combines it with the AOA of the received signal [5].

This work will focus on RFID-based localization system. A brief literature survey of L&T technique utilizing RFID technology is presented in section 1.4.

1.3 Comparison of Positioning Systems

Table 1 compares different positioning systems based on their accuracy, power consumption, operation in LOS and NLOS conditions, operating environment (Indoor (I) / Outdoor (O)), and number of base stations. The following observations can be made from Table 1:

1 Most of the systems that operate in LOS scenarios are more accurate. Thus, relying solely on NLOS introduces error in the calculation, decreasing the accuracy.

2 Many existing positioning systems employ multiple base nodes to localize the target node increasing the overall system cost.

Table 1: Comparison of positioning systems [1–7]. O = Outdoor, I = Indoor

Positioning system	Ranging accuracy (m)	LOS NLOS	Operating environment	Power consumption (W)	Number of base stations
GPS	1-5	LOS	O	$\leq$1	4
INS	5-50	Both	O,I	10-200	-
RFID	0.1-5	Both	O,I	1-10	3
WLAN	2-30	Both	O,I	1-10	3
Vision	1-100	LOS	O,I	10-50	1
Radar	1-5	LOS	O	>200	1

3 Many positioning systems are well-suited for both outdoor and indoor environments.

1.4 Literature Survey

Localization is the process of finding the position and bearing of an object with respect to a reference point. Tracking, on the other hand, is identifying, observing, and monitoring the path followed by an object. The aim of object tracking using RFID technology is to gather information from RFID-tagged objects in the vicinity of a reader and making observations to estimate their current position, predict and correct future positions, and solve for a path in real time [55]. The information gathered consists of the characteristics of backscattered RF signals such as received signal strength (RSS), received signal phase, object identity, and any additional sensory information from the RF tag [56–58]. The flexibility of combining the identity of an object with its location makes RFID technology a very powerful tool for localizing and tracking.

The taxonomy of location and tracking systems can be classified as shown in Figure 3, [6–43]. Location and tracking (L&T) systems can generally be divided into two broad categories, RF-based and non-RF-based [8]. RF-based location includes systems such as radar, RFID, cellular networks, Global Positioning System (GPS),

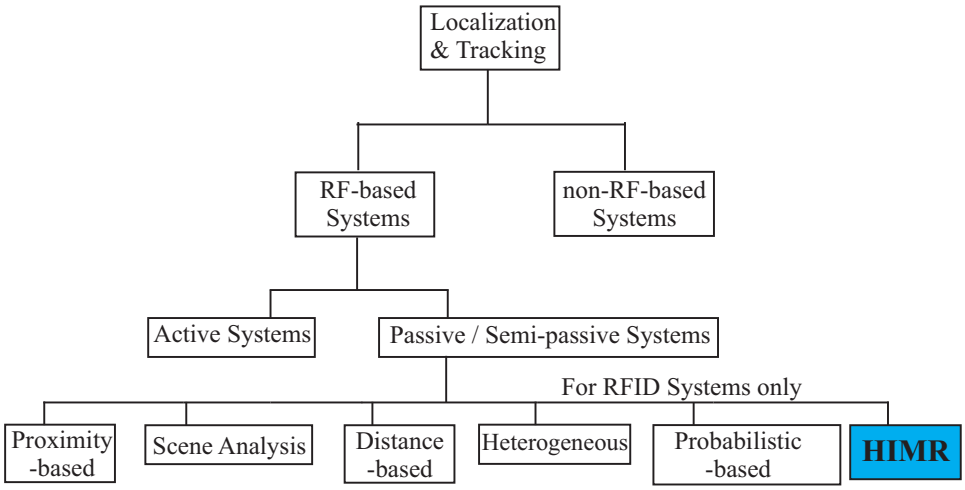

Figure 3: Taxonomy of localization and tracking techniques for RFID Systems [6–43]. The techniques in the last row are arranged in no particular order.

WiFi, Bluetooth, and ZigBee. The non-RF-based category includes systems based on cameras / optics, infrared [9], odometry, lasers, inertial, and ultrasound [10, 11]. Although these can be further classified into many sub-categories, in this article we will only consider the chain that includes RFID-based systems. This category can be split into active and passive branches. Cellular networks are a classic example of an active RF-based localization system in which the nodes (cellphones) and the base stations (towers) communicate with each other to determine a position. RFID systems and radar are examples of RF-based passive or semi-passive systems in which the target nodes (RF tags, airplanes) reflect the RF waves to fixed receivers (readers, radars, etc.). The offshoots from the passive systems branch in Figure 3 highlight and summarize L&T techniques strictly used by RFID systems.

A comparison of the listed RFID L&T techniques based on their accuracy is presented in Figure 4. It can be observed that the HIMR provides better and finer accuracy in the range of 1 to 20 mm, as compared to other schemes. Figure 4 clearly depicts the superiority of the HIMR scheme over the existing schemes. L&T techniques based on scene analysis, distance-based, and probabilistic approaches have

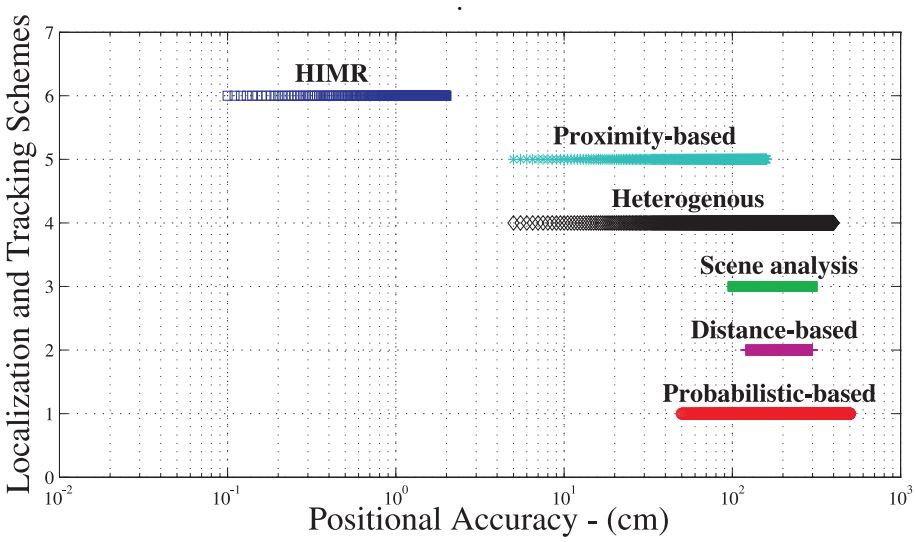

Figure 4: Range accuracy comparison of the existing L&T techniques with HIMR [6–46].

an accuracy range above 100 cm. Proximity and Heterogeneous - based techniques have a wide range of accuracy between 5–400 cm. The HIMR accuracy has been determined through simulation and experimental results which shall be presented in later sections. The accuracy range of the other schemes is reported in the text [6–46] and summarized in Figure 4.

1.4.1 Proximity-based L&T

The *proximity-based* L&T technique is easy-to-implement. It uses the reference tags (RTs) which are pre-installed at known locations in some known pattern grid inside an area of interest. The location on the grid and identification sequence of each RT is stored in the database of the target reader. When the target object, which contains a reader, is in the vicinity of an RT, it can identify its own position on the grid by matching the tag ID and its corresponding location with the database. In some cases, depending upon the type of installation of RTs at known locations, the target object can also compute its angle with respect to the reference tag. In another method for implementation of the proximity technique, the installation pattern can

be reversed. Instead of RTs, the RFID readers can be installed at known locations in the region under consideration. The position of the RFID tagged object can be narrowed in a zone when sensed by the reader receiving maximum signal strength. This scheme gives an accuracy in the range of 5–160 cm. Several examples of the proximity-based technique have been referenced in [12–14].

1.4.2 Scene-Analysis-based L&T

In the *scene-analysis-based* L&T technique, the received signal strength (RSS) of the domain of interest is mapped with RTs, and single or multiple RFID readers are installed overlooking the desired domain. The RSS and other parameters, such as estimated direction of arrival (DOA), of each reference tag are measured and pre-stored in the reader. When the object of interest with the installed tag moves inside the domain, its RF fingerprints, i.e. RSS and DOA, are matched with the database to estimate the location. If the result overlaps the zone of more than one tag, well known algorithms such as LANDMARC or its improved versions are used to estimate the location. Often, instead of physically installing the RTs, the user maps the entire domain virtually to define an approximate RSS of an RT, and the same procedure is repeated to approximate the location. *Scene analysis* examples such as LANDMARC, VIRE, L-VIRT among others are included in citations from [15–19]. As given in Figure 4, these techniques yield an accuracy in the range of 100–300 cm.

1.4.3 Distance-based L&T

The *distance-based* approach is the most commonly used localization technique. This approach uses numerous methods such as triangulation, multi-lateration, interferometry, and RSS to estimate the distance between tag and reader. In a few applications, the information obtained from the aforementioned methods acts as an input into a probabilistic approach to obtain a more refined distance estimation. Several examples for distance based approaches are given in [20–26]. Using this scheme

results in accuracy on the order of 120–300 cm (Figure 4).

1.4.4 Heterogeneous L&T

The *heterogeneous* technique makes use of a combination of another RF or non-RF-based source along with an RFID system to estimate the position of the tag and to perform its tracking. The information from two systems can be used in a variety of ways. For example, in [27], a robot explores its vicinity using an RFID system to get a crude position, and it then uses information from ceiling mounted cameras to refine its location. In another example, Papapostolou and Chaouchi [30] carry out simultaneous user-based and network-based localization using RFID and WLAN systems. The data from both schemes are combined to overcome the individual pitfalls of each scheme and to get better accuracy. Some of the external sources mentioned in the literature that have been used along with the RFID systems include WiFi, laser sensors, odometry sensors, and ZigBee. Examples are given in [27–32]. Since the heterogeneous techniques are a combination of a variety of sources, the accuracy varies in a wide range from 5–400 cm as illustrated in Figure 4.

1.4.5 Probabilistic Approach

Multipath fading, interference, measurement and system noise are environmental dependent factors that change with time, and affect the RSS and phase of received RF signals. Predefined environmental models can be used along with statistical filters such Kalman or particle filters to mitigate the effect of these variations. Such filters have also been implemented for RFID-based L&T [41–43]. These have been classified under the *probabilistic approach* in this work and have a reported accuracy in the range of 50–500 cm (Figure 4). However, the L&T algorithms developed using the probabilistic approach are complex and difficult to implement in real scenarios.

Unlike heterogeneous schemes where two different radio systems are combined to get the location, HIMR combines RSS and phase information from the backscattered

RF signal, and low-power, tag-mounted inertial sensor data, to get the position and tracking of the RF tag—all as part of the same RFID system without additional reference tags. Conventional techniques and their applications presented in [6–43, 59–61] use either RSS, phase, or both to perform L&T. Some schemes make use of an external system and thus are classified as a *heterogeneous approach*. No existing techniques for L&T have combined the aforementioned information in a single scheme to achieve localization. Parr et. al. in [38] combined acceleration from the RFID-reader-mounted inertial sensor and received signal phase to estimate the location. But the approach presented in this work is fundamentally different; first, in this scheme the inertial sensor is installed on an RF-tag instead of on the RFID-reader, and its information is part of the backscattered data packets. Installation of the inertial sensor on the object allows us to measure and wirelessly transmit the sensor information to the reader base station. This would be useful for the wireless motion capture applications mentioned below. Secondly, no differentiation or integration operation is performed on the phase or acceleration data; differentiation amplifies the harmful influence of sensor noise, and integration leads to drift due to measurement bias, so neither of these operations is consistent with the goal of decaying error. Lastly, HIMR uses three pieces of information (RSS, phase and inertial) as opposed to just two pieces of information (phase and inertial) in [38].

CHAPTER II

ONE-DIMENSIONAL L&T USING HIMR

2.1 RFID System Description

A UHF/microwave RFID system is similar to a radar system that illuminates its target with RF power. This power reflects back from the target, is received, and processed to extract the desired information. An RFID system works in an identical fashion, retrieving digital information from an illuminated RFID *tag* using a *reader*. A generic block diagram of an RFID system is shown in Figure 5.

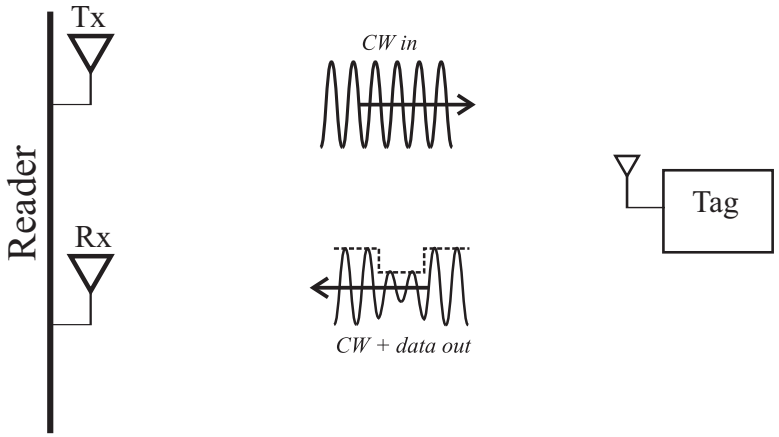

Figure 5: Block diagram of a generic bi-static backscatter system employing backscatter modulation.

The reader in Figure 5 transmits (Tx) continuous electromagnetic waves at the operating frequency towards the tag, which in turn modulates these waves using *load modulation* and reflects them back to the reader's receiver (Rx) antenna. The reflection of the data from the tag is known as *backscattering*. This mode of communication is so power efficient that some RFID tags can be purely *passive*, operating solely on energy harvested from the incident RF field [54]. *Semi-passive* or *battery-assisted*

tags employ small, long-lived batteries which allow operation at long ranges with peripheral sensor circuitry.

The HIMR technique uses a *battery-assisted* RF tag that is equipped with an accelerometer, which senses the acceleration of the moving tagged object and backscatters the acceleration information in the form of a customized packet. The RFID system considered in this paper is a prototype system used to validate the HIMR scheme concept. Therefore, the communication protocol considered in this system is also customized and does not follow the EPCGlobal Gen2 standard. However, in a commercialized system, tags capable of working with existing RFID standard communication protocols could be built. In the current prototype system, the information packet encoding scheme and data rate are also customized to incorporate the acceleration information and to achieve long range. The data structure of the customized packet is shown in Table 2. It consists of a three-byte preamble, a unique two-byte tag ID, three-dimensional sensed acceleration data in six bytes, and one-byte cyclic redundancy check (CRC) information. Each bit in the data packet is encoded using a binary-offset carrier (BOC) modulated signal with 64 transitions per data bit. The tags have a switching rate of 5 Mcps (corresponding to a maximum transmission rate of 78.1 kbit/s), which results in an average packet rate of about 300 packets per second when accelerometer measurement and input/output times are considered. Complete details on the data packet structure and the protocol used for its packetizing is given in [58]. A picture of the tag used for one-dimensional HIMR testing is provided in Figure 6.

In its current form, the prototype tag continuously backscatters inertially sensed data, consuming 9.3 mW of power using a coin cell battery with 3 V, 240 mAh ratings. During laboratory tests, it was found that in continuous operation the prototype tag lasts for 72–77 hours; when the tag switching rate was reduced to 2 MHz, resulting in 100 packets per sec transmission rate, tag power consumption decreased to 6.6 mW

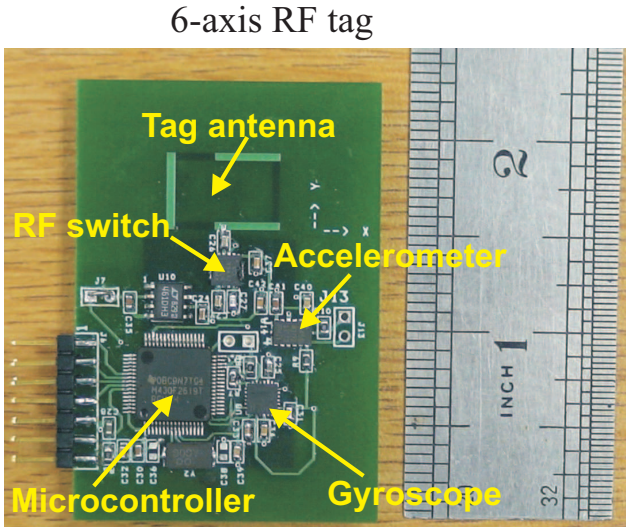

Figure 6: 6-axis RF tag used for one-dimensional HIMR testing. Only the accelerometer was used for preliminary measurements [47, 48], however, in multi-dimensional-HIMR tests accelerometer together with rotation (gyroscope) and orientation (magnetic compass) sensors will be utilized for localization and tracking.

with continuous backscattering. In a commercialized version, the battery life could be increased by optimally reducing the RF packet transmission rate and introducing tag sleep, wake-up, and interrogation cycles. Moreover, if required, a customized RFID chip complying with EPCGlobal Gen2 protocol and containing an inbuilt inertial sensor may also be considered in a final product, thereby further increasing battery life. References [62–65] discuss methods for taking data gathered from external sensors and relaying their information through EPCGlobal Gen2-compliant RF tags.

Table 2: Structure of a backscattered data packet in the HIMR-scheme.

Preamble	Tag ID	Accelerometer Data	CRC
Three bytes	Two bytes	Six bytes	One byte

2.2 HIMR Setup

For simplicity of understanding, one-dimensional linear motion along the z-axis will be considered in this chapter. It is assumed that the location of the reader is known and is taken to be the origin. The tag is installed on one of the arms of a high-speed positioner, which can simultaneously move its three mutually perpendicular arms in three dimensions. The entire system with reader, tag, and positioner is illustrated in Figure 7. Three types of information are sensed at the reader when the RF tag backscatters the data: the received signal amplitude $H(z)$ which will be used to compute the approximate position of the tag z relative to the reader; absolute phase $\phi_p(z)$ which will be used to calculate the approximate tag velocity $\dot{z}$; and the decoded acceleration data $\ddot{z}$.

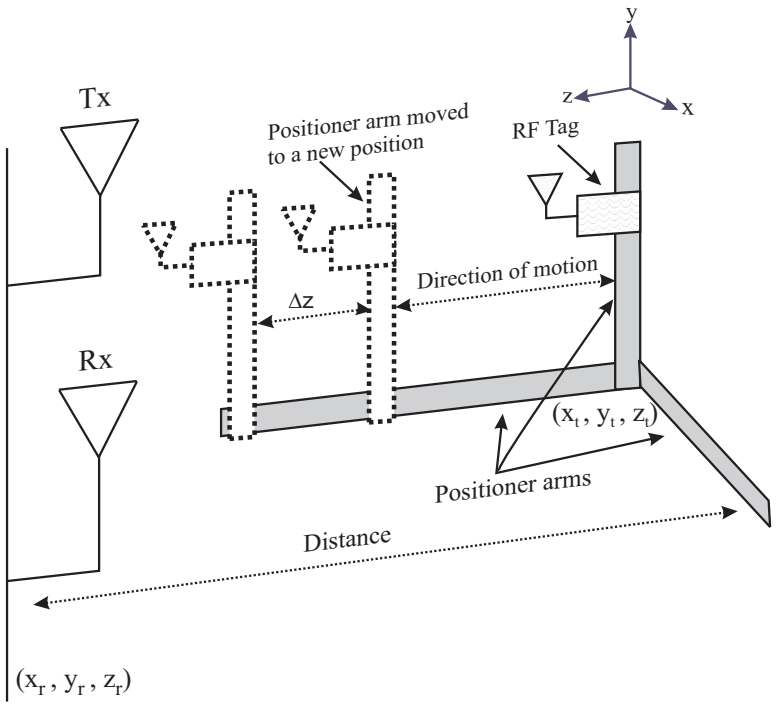

Figure 7: Three dimensional positioner setup. The tag moves towards the reader along the z-axis. The dotted arm shows its positions after the positioner movement.

2.2.1 Signal Description

The RF tag switches between two loads to modulate the acceleration information on the carrier signal and reflects it back to the reader. An inherent advantage of RFID reader systems is the phase coherence of the carrier frequency because the same oscillator is used in both the transmitter chain and the receiver chain. Therefore, the received complex baseband signal $\tilde{S}(z,t)$ after the demodulation by the coherent carrier signal can be written as:

$$\tilde{S}(z,t) = H(z)\exp\left(-j\left[\frac{4\pi z}{\lambda} + \phi_m(t) + \phi_o\right]\right) \tag{1}$$

where $H(z)$ is the distance-dependent amplitude of the signal, λ is wavelength, ϕ_o is the accumulated phase offsets from the channel, $\phi_m(t)$ is the time varying phase modulation, switching between 0 and π to represent binary 1s and 0s and $\frac{4\pi z}{\lambda}$ is the absolute phase of the signal due to its propagated distance. In a complex baseband representation, the real part represents the time-varying output of the in-phase channel and the imaginary part represents the time-varying output of the quadrature channel of the down-converted (and filtered) backscattered signal.

2.3 Hybrid Inertial Microwave Reflectometry - Sensed Quantities

2.3.1 Position

The amplitude, $H(z)$, of the received signal is dependent on the distance z. It increases when the tag moves towards the reader and decreases when the tag moves away from the reader. The received signal amplitude, $H(z)$, can be related to root mean squared (rms) received power, P_{rms}, through the following relation:

$$P_{rms}(z) \approx \frac{H^2(z)}{2R} \tag{2}$$

where, R is the impedance of the system. The RMS received power for a co-located bi-static reader system is given by [66]:

$$P_{rms}(z) \approx \frac{P_T G_T G_R {G_t}^2 \lambda^4 X^2 M}{(4\pi z)^4} \tag{3}$$

where P_T is the reader's transmitted power, G_T is the reader's transmitter antenna gain, G_R is the reader's receiver antenna gain, G_t is the tag's antenna gain, λ is wavelength of the carrier frequency, X is the polarization mismatch between the reader's and the tag's antennas, M is the load modulation factor of the tag, z is the separation distance between the reader and the tag. Equation (2) together with (3) are rearranged to approximate the position as follows:

$$z \approx \sqrt[4]{\left(\frac{2P_T G_T G_R {G_t}^2 \lambda^4 X^2 M R}{(4\pi)^4 H^2(z)}\right)} \tag{4}$$

Using received signal amplitude alone has not resulted in fine-scale localization. Several L&T techniques relying on the received signal amplitude have been referenced and summarized under the *proximity-based*, *scene analysis* and *distance-based* categories in section I; their ranging accuracy varies widely from 5–300 cm [8-23] as illustrated in Figure 4.

2.3.2 Velocity

The phase, $\phi_p(z) = \frac{4\pi z}{\lambda}$, of the received signal in (1) is closely related to the motion of the tag. In this work, the change in propagated phase, $\Delta\phi_p(z)$, is one of the quantities that will be used to track the motion of a tagged object by calculating its approximate, $\dot{z}$, with respect to the direction of motion. These are related by the following:

$$\dot{z} \approx \frac{\lambda}{4\pi}\frac{\Delta\phi_p(z)}{\Delta t} \tag{5}$$

Although the velocity in (5) can accurately discern changes in position but in the absence of other measurements it is prone to aliasing for fast-moving tags or radio

channels that have fading or burst noise. Therefore, the additional quantities such as received signal amplitude and the acceleration of the object are required to track the positional changes and correct for phase aliasing.

2.3.3 Acceleration

The acceleration $\ddot{z}$ of a tagged object may be measured using an inertial sensor. In this paper, the RF tag is equipped with a low-power, three-axis accelerometer chip that provides an approximation of tag acceleration. The acceleration information is packetized and backscattered along with the tag ID, as described in Table 2 and in Section 2.3 of [58]. The acceleration information is retrieved from the demodulated received signal, and it is converted from the body-frame-axis to absolute coordinates by using a standard rotation matrix.

In principle, acceleration information can be used to track an object by integrating over time, but the resulting integrator drift will result in poor accuracy. The HIMR scheme does not involve integration of acceleration data; instead, it fuses all three pieces of information together to overcome their individual drawbacks, resulting in fine-resolution L&T.

2.3.4 Sensors

The acceleration sensor located on the tag, along with the velocity and position sensing formulas (4) and (5) evaluated on the reader, constitute a set of measurements that approximately describes tag motion. If the sensory information obtained from these sources was sufficiently accurate, then the goal of wirelessly detecting the position trajectory would be achieved without additional signal processing (e.g. only the position sensing formula would be needed). In reality, all three sensed signals are corrupted by noise, and hence their direct use cannot fulfill the objective of fine-scale L&T. In the following section, a mathematical model governing the evolution of the

true motion signals (z, $\dot{z}$, $\ddot{z}$) will be provided, along with analysis of a state estimation scheme that systematically fuses the sensor outputs so as to enable high-accuracy position tracking.

2.4 Hybrid Inertial Microwave Reflectometry - Scheme

2.4.1 Modeling

The tagged object is modeled as a point mass experiencing one-dimensional motion in a direction orthogonal to gravity. The equation of motion is therefore

$$m\ddot{z} = f \tag{6}$$

where m denotes the mass of the object, f denotes the resultant of forces applied to the mass, and z denotes the position of the mass; consequently, the velocity and acceleration of the mass are denoted by $\dot{z}$ and $\ddot{z}$ respectively. The motion of the tagged object is determined by the ratio of f and m, but neither f nor m is known or measured. Sensors intended to measure z, $\dot{z}$ and $\ddot{z}$ are assumed to be available, but the measurements provided by these sensors are corrupted by noise.

The tagged object and its sensing system may be expressed in state-space form by [67]

$$\dot{\mathbf{x}} = \mathbf{A}\mathbf{x} + \mathbf{B}\mathbf{w} \tag{7}$$

$$\mathbf{y} = \mathbf{C}\mathbf{x} + \mathbf{v} \tag{8}$$

where the state variables are $x_1 = z$, $x_2 = \dot{z}$ and $x_3 = \ddot{z}$, $\mathbf{w} = \dot{f}/m$ denotes a scalar disturbance, $\mathbf{y}$ denotes a vector of sensor output signals, and $\mathbf{v}$ denotes a vector of sensor noise signals. The coefficient matrices are

$$\mathbf{A} = \begin{bmatrix} 0 & 1 & 0 \\ 0 & 0 & 1 \\ 0 & 0 & 0 \end{bmatrix}, \quad \mathbf{B} = \begin{bmatrix} 0 \\ 0 \\ 1 \end{bmatrix}, \quad \mathbf{C} = \begin{bmatrix} 1 & 0 & 0 \\ 0 & 1 & 0 \\ 0 & 0 & 1 \end{bmatrix} \tag{9}$$

where $\mathbf{C}$ is shown for the case where approximate sensing systems are available for position, velocity and acceleration. It is apparent that there are two types of uncertainty which will ultimately influence the state estimation process; the disturbance signal $\mathbf{w}$ and the noise signal $\mathbf{v}$.

2.4.2 Estimation

The state estimator will be constructed by neglecting the presence of $\mathbf{w}$ and $\mathbf{v}$ in (7) and (8), since these signals are not known or measured. The estimated value of the imperfectly measured state vector $\mathbf{x}$, which is denoted by $\hat{\mathbf{x}}$, will be obtained by solving the differential equation

$$\dot{\hat{\mathbf{x}}} = \mathbf{A}\hat{\mathbf{x}} + \mathbf{L}\left(\mathbf{y} - \hat{\mathbf{y}}\right) \tag{10}$$

$$\hat{\mathbf{y}} = \mathbf{C}\hat{\mathbf{x}} \tag{11}$$

as time evolves. The estimator state equation (10) incorporates a copy of state equation (7) with $\mathbf{w} = 0$, and the estimator output equation (11) is a copy of output equation (8) with $\mathbf{v} = 0$. The assignable gain matrix L multiplies the output error $\mathbf{y} - \hat{\mathbf{y}}$, and hence two terms combine in (10) to determine future values of $\hat{\mathbf{x}}$; neither of these terms is sufficient individually, since one neglects $\mathbf{w}$ and one neglects $\mathbf{v}$. Gain matrix $\mathbf{L}$ may be adjusted to trade off these competing imperfections; larger $\mathbf{L}$ is desired if $\mathbf{w}$ is larger than $\mathbf{v}$, and smaller $\mathbf{L}$ is desired if $\mathbf{w}$ is smaller than $\mathbf{v}$. A signal flow diagram of the motion system and its estimator is shown in Figure 8.

The role of $\mathbf{L}$ may be more fully understood by considering the state estimation error, defined by $\mathbf{e} = \mathbf{x} - \hat{\mathbf{x}}$. Differentiating $\mathbf{e}$, and substituting (7) and (10) into the result, yields

$$\dot{\mathbf{e}} = \left(\mathbf{A} - \mathbf{LC}\right)\mathbf{e} + \mathbf{Bw} - \mathbf{Lv}. \tag{12}$$

According to (12), the estimator will be stable if and only if all eigenvalues of $\mathbf{A} - \mathbf{LC}$ are located in the open left half of the complex plane. Once the sensors have been

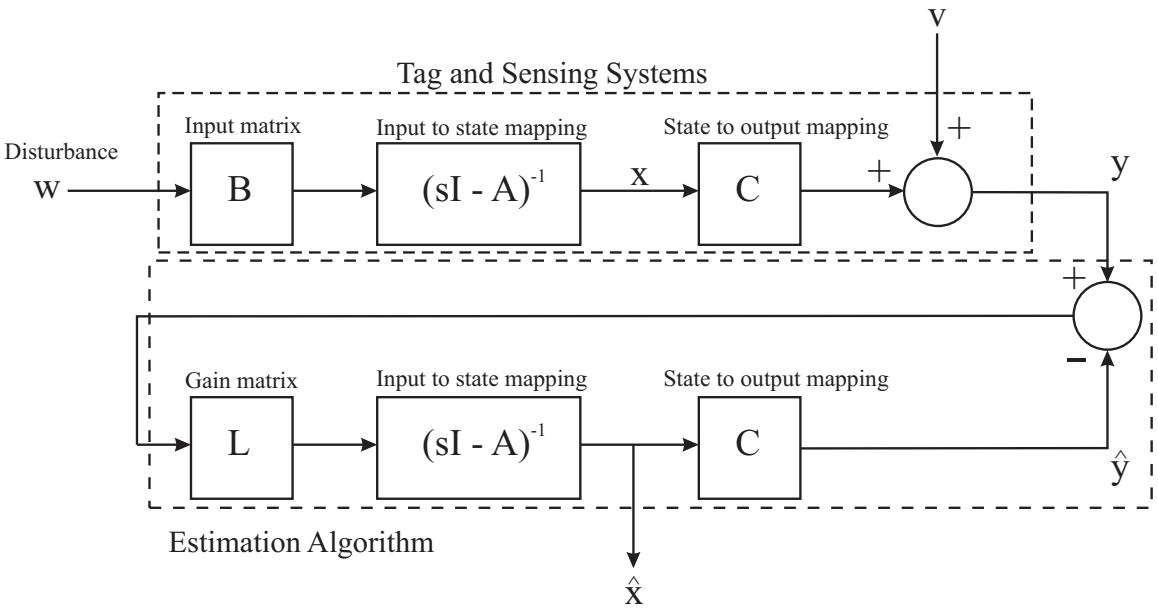

Figure 8: The motion system, characterized by disturbance input $\mathbf{w}$, imperfectly measured state $\mathbf{x}$, and sensor noise $\mathbf{v}$, and the associated motion estimator which generates state estimate $\hat{\mathbf{x}}$.

selected both $\mathbf{A}$ and $\mathbf{C}$ will be known, but $\mathbf{L}$ remains as a design variable that may be adjusted to meet this stability requirement. Determining a stabilizing $\mathbf{L}$, given $\mathbf{A}$ and $\mathbf{C}$, is always possible provided that the matrix pair $(\mathbf{A}, \mathbf{C})$ satisfies a property known as observability, which will now be defined. Assuming that $\dim\{\mathbf{x}\} = n$ and $\dim\{\mathbf{y}\} = p$, the so-called observability matrix

$$\mathbf{O} = \begin{bmatrix} \mathbf{C} \\ \mathbf{CA} \\ \vdots \\ \mathbf{CA}^{n-1} \end{bmatrix} \tag{13}$$

has np rows and n columns. The matrix pair (A, C) is observable if and only if $\text{rank}\{\mathbf{O}\} = n$.

2.4.3 Sensing

The matrix $\mathbf{A}$ has three eigenvalues, all at $s = 0$, since $\det(s\mathbf{I} - \mathbf{A}) = s^3$; all three of these eigenvalues are located on the boundary of the stability region, and hence they must all be relocated into the interior of the stability region in order to achieve stable estimation. The desirable feature of stable estimation is that, if $\mathbf{w} = 0$ and $\mathbf{v} = 0$, the estimated $\hat{\mathbf{x}}$ will converge to the imperfectly measured $\mathbf{x}$ at an exponential rate determined by $\mathbf{L}$, for arbitrary initial conditions; even if $\mathbf{w} \neq 0$ and $\mathbf{v} \neq 0$, stable estimation guarantees exponential convergence of the estimation error to some non-zero residual level that scales with the size of $\mathbf{w}$ and $\mathbf{v}$.

It is of interest to understand how estimator stability will be influenced by the choice of which sensors are actually used in the estimation process. Considering all possible permutations of sensors from among those assumed to be available, Table 3 summarizes the results of observability analysis. The number of assignable coefficients in the matrix $\mathbf{L}$ depends on the number of sensors being used; one sensor leads to three coefficients, two sensors leads to six coefficients, and three sensors leads to nine coefficients. The rank of observability matrix $\mathbf{O}$ measures the extent to which the eigenvalues of $\mathbf{A} - \mathbf{LC}$ can be made different from the eigenvalues of $\mathbf{A}$; a rank of one indicates that one estimator eigenvalue can be made stable, a rank of two indicates that two estimator eigenvalues can be made stable, and a rank of three indicates that three estimator eigenvalues can be made stable. The analysis shows that stable estimation is possible if and only if the estimator incorporates a position sensor. In this work, all available sensors are used, as indicated by the choice of $\mathbf{C}$ in (9).

2.4.4 Tuning

According to (12), both $\mathbf{w}$ and $\mathbf{v}$ induce estimation error, the former through $\mathbf{B}$ and the latter through $\mathbf{L}$; moreover, $\mathbf{L}$ also influences the eigenvalues of the estimation error dynamics. Hence, the choice of $\mathbf{L}$ involves a fundamental trade-off:

Table 3: Influence of Sensor Set on Estimator Stability

Set	x_1	x_2	x_3	$\text{rank}\{\mathbf{O}\}$	$\dim\{\mathbf{L}\}$	$\#\lambda\{\mathbf{A}-\mathbf{LC}\}=0$
0				0	—	3
1			✓	1	3×1	2
2		✓		2	3×1	1
3		✓	✓	2	3×2	1
4	✓			3	3×1	0
5	✓		✓	3	3×2	0
6	✓	✓		3	3×2	0
7	✓	✓	✓	3	3×3	0

1. If unmodeled disturbance $\mathbf{w}$ is large compared to sensor noise $\mathbf{v}$, then improved estimation accuracy will result if $\dot{\hat{x}}$ in (10) depends less on $\mathbf{A}\hat{\mathbf{x}}$, which neglects the influence of $\mathbf{w}$, and more on $\mathbf{L}\,(\mathbf{y}-\hat{\mathbf{y}})$, which introduces the influence of $\mathbf{v}$; this situation calls for large $\mathbf{L}$.

2. If sensor noise $\mathbf{v}$ is large compared to unmodeled disturbance $\mathbf{w}$, then improved estimation accuracy will result if $\dot{\hat{\mathbf{x}}}$ in (10) depends less on $\mathbf{L}\,(\mathbf{y}-\hat{\mathbf{y}})$, which introduces the influence of $\mathbf{v}$, and more on $\mathbf{A}\hat{\mathbf{x}}$, which neglects the influence of $\mathbf{w}$; this situation calls for small $\mathbf{L}$.

Determining a suitable choice of $\mathbf{L}$ for a given system involves a tuning process, and in this work a three-step Riccati equation based tuning process is used.

1. Assign tuning matrices $\mathbf{W}$ and $\mathbf{V}$ satisfying

$$\mathbf{W}=\mathbf{W}'>0,\quad \mathbf{V}=\mathbf{V}'>0. \tag{14}$$

2. Obtain matrix Y by solving

$$\mathbf{A}\,\mathbf{Y}+\mathbf{Y}\mathbf{A}'-\mathbf{Y}\mathbf{C}'\mathbf{V}^{-1}\mathbf{C}\mathbf{Y}+\mathbf{W}=0. \tag{15}$$

3. Obtain matrix $\mathbf{L}$ by solving

$$\mathbf{L}=\mathbf{Y}\mathbf{C}'\mathbf{V}^{-1}. \tag{16}$$

The matrices $\mathbf{W}$ and $\mathbf{V}$ are supposed to be real-valued, symmetric and positive definite; this means that (i) the quadratic forms $\alpha'\mathbf{W}\alpha$ and $\alpha'\mathbf{V}\alpha$ evaluate to strictly positive scalar values for every nonzero real-valued vector α, and (ii) the eigenvalues of $\mathbf{W}$ and $\mathbf{V}$ are all real-valued and strictly positive. Any choices satisfying (14) will guarantee estimator stability, so even diagonal matrices may be used in practice, as shown in the experimental results below. If unmodeled disturbance $\mathbf{w}$ and sensor noise $\mathbf{v}$ have been statistically characterized, then $\mathbf{W}$ and $\mathbf{V}$ may be interpreted as corresponding covariance matrices, in which case the matrix $\mathbf{L}$ determined in (16) can be shown to minimize the steady-state covariance of the estimation error. Once $\mathbf{W}$ and $\mathbf{V}$ have been statistically evaluated or otherwise assigned, $\mathbf{Y}$ is obtained by solving the continuous-time algebraic Riccati equation (15); numerical methods for this calculation are available, e.g. function `care` of the MATLAB Control System Toolbox.

For the experimental results reported herein, the tuning matrices were chosen as

$$\mathbf{W} = 5 \times 10^4 \begin{bmatrix} 3 & 0 & 0 \\ 0 & 1 & 0 \\ 0 & 0 & 1 \end{bmatrix}, \quad \mathbf{V} = \begin{bmatrix} 1 & 0 & 0 \\ 0 & 1 & 0 \\ 0 & 0 & 1 \end{bmatrix}. \tag{17}$$

In this case, the weights along the diagonal of $\mathbf{W}$ are large compared to the weights along the diagonal of $\mathbf{V}$, suggesting that the size of $\mathbf{w}$ is large compared to the size of $\mathbf{v}$; this should lead to relatively large gain and relatively fast eigenvalues. Completing the computations outlined above leads to estimator gain matrix

$$\mathbf{L} = \begin{bmatrix} 387.3 & 0.366 & 0.00052 \\ 0.366 & 223.6 & 0.5 \\ 0.00052 & 0.5 & 223.6 \end{bmatrix} \tag{18}$$

and estimator eigenvalue locations

$$s = -387.3, -223.6 \pm j0.5 \tag{19}$$

with corresponding settling times on the order of 10 ms.

2.4.5 Implementation

The physical system is a continuous-time system, but its estimation should be performed on a discrete-time processor. This unavoidable continuous-discrete mismatch may be dealt with in either of two ways: (i) derive a continuous-time estimator for the continuous-time physical system, and then approximate the continuous-time estimator by a discrete-time estimator; (ii) approximate the continuous-time physical system by a discrete-time model, and then derive a discrete-time estimator for the discrete-time model. Both approaches require approximation, and both approaches will yield similar results under similar hypotheses. In this work, the first approach is taken, as it allows the continuous-time nature of the physical system to remain in focus until the final step of estimator implementation.

The estimation algorithm (10)–(11) has been derived using a continuous-time model of the system, but its implementation requires a discrete-time formulation. To this end, the state equation of the estimator is transcribed from a differential equation to a difference equation. There are many methods for doing this, but in the present work the simplest method, known as the forward Euler method, has been used. The result of this procedure is

$$\hat{\mathbf{x}}[k+1] = \hat{\mathbf{x}}[k] + T\left(\mathbf{A}\hat{\mathbf{x}}[k] + \mathbf{L}\left(\mathbf{y}[k] - \hat{\mathbf{y}}[k]\right)\right) \tag{20}$$

$$\hat{\mathbf{y}}[k] = \mathbf{C}\hat{\mathbf{x}}[k] \tag{21}$$

where T is the fixed time increment between difference equation updates and k is the iteration index. For each increment of k, new measurements $\mathbf{y}$ arrive and new estimates $\hat{\mathbf{x}}$ are computed. Although matrices $\mathbf{A}$, $\mathbf{C}$ and $\mathbf{L}$ are unchanged by this transcription procedure, their influence on estimator updates is scaled by T.

2.4.6 Extensions

In (6), the tagged object has been modeled as a point mass experiencing one-dimensional motion in a direction orthogonal to gravity. The motivation behind this

simplifying assumption is to reveal, in the simplest possible context, the fundamental issues involved when estimating tag motion from disparate sensor measurements. Nevertheless, it is appropriate to briefly comment on possible extensions of the technique introduced in this work to other, more general, scenarios. The point of departure would be a reformulation of (6) to account for multiple axes of tag translation and the possibility of tag rotation. From this reformulation of tag dynamics, along with a specification of a more comprehensive sensor set (e.g. incorporating multiple axes of inertial sensor measurements), a new higher-dimension state-space model of the form (7)–(8) would be developed. Although a new observability analysis would be required to guarantee the suitability of the proposed sensor set, the methods reported in this work so far would still apply since they do not inherently rely on an assumption of one-dimensional motion.

2.5 Simulation Results

The simulation[1] analysis of a HIMR system was carried out in Matlab for a tag and positioner setup as shown in Figure 9. The positioner is capable of moving its arm in three dimensions and follows trapezoidal motion profiles. For simulations, the trapezoidal motion profiles were generated in Matlab. The generated profiles are similar to the actual motion undertaken by the positioner shown in Figure 9. It was assumed that accelerometer mounted tag is installed on one of the arms and backscatters inertially sensed acceleration data back to the reader. The purpose of simulations is to explain the effectiveness of HIMR against realistic noisy measurements. The simulation is done in the following steps:

1 The reference velocity, and acceleration profiles were generated in Matlab. These profiles are identical to the velocity and acceleration profiles of a 3-D positioner available at Georgia Tech (Figure 9). It is assumed that the tag

[1]This work has been published in [47].

moves away from reader along the x-axis with the accelerometer-mounted-tag. The tag initially located at a distance of 1 meter from the reader and travels a distance of 0.61 meters away from the reader. Starting from rest, the tag accelerated at 7.35 m/s^2 (0.75 g) to attain a velocity of 1.2 m/s and then moved at this constant speed (zero acceleration) for 355 ms before decelerating at a constant rate of -7.35 m/s^2 (0.75 g), decreasing the velocity to zero. This is illustrated by distance, velocity, and acceleration curves given in Figure 10.

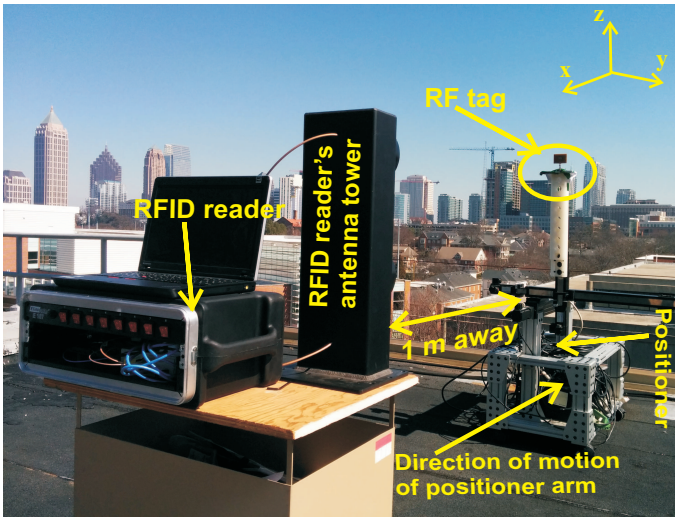

Figure 9: A picture of the 3-D positioner setup at Georgia Tech. In simulations, it is assumed that the positioner arm with tag moves a distance of 0.61 m, away from the reader station along the straight line in one direction and follows a trapezoidal kind of motion profile during the movement.

2 Additive white Gaussian noise of $\mathcal{N}(0, 1)$ was added to all three profiles as shown in Figure 11. The scale factors for the noise were randomly picked as 0.03, 0.08, and 0.05 for noise addition in amplitude, phase difference, and acceleration profiles respectively. The purpose of adding the noise is to simulate the three quantities as noisy measurements in the actual system. It is pertinent to note that the motion profiles explained above are unknowns in the experiment. The HIMR scheme has no knowledge of the these profiles and only initial conditions

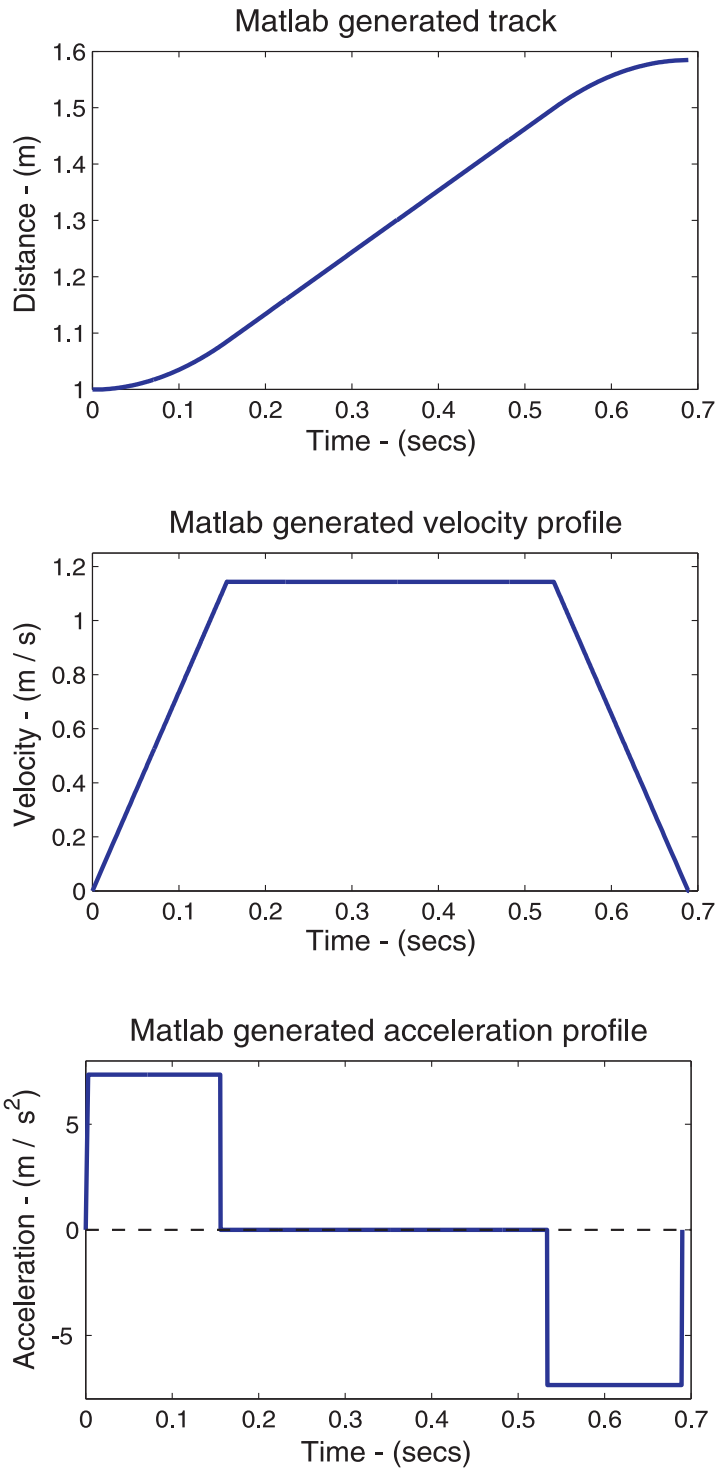

Figure 10: This figure illustrates the reference profiles generated in the Matlab.

are given to the HIMR scheme.

3 The discrete form of the HIMR scheme at (20) is run to estimate the states using the noisy profiles. The HIMR scheme both estimates the states and also reduces the error to make the system track the actual states. It can be observed from Figure 12 that noise has been reduced and the simulated curves closely follow the original reference profile curves. Especially, the resultant distance profile curve at the top of the Figure 12 leads to the inference that HIMR is capable of giving millimeter-level accuracy in tracking the position of the object.

2.6 Integration

An important aspect of HIMR technique is that it does not involve integration or differentiation operation on the sensed information to extract and track the position. If one chooses to use the acceleration or velocity alone to get the resulting position using integration, then a slight offset or noise on the sensed data will result in accumulated drift over time. To illustrate this fact, the noisy acceleration data generated in the simulation setup was integrated to get the position. As presented in Figure 13, a drift of 2.5 cm was observed from the actual position over 0.6 m distance. The accumulated error will increase if observed over a longer time duration. Therefore, extracting positional information using mathematical integration of the sensed acceleration data is not a viable option for mm-scale L&T.

2.7 Experimental Results

To substantiate the HIMR simulation results, an experiment was conducted using the test setup as illustrated in Figure 9. The tests were conducted outdoor on a roof top and the setup was comprised of a 5.8 GHz RFID system with 9.5 dBi transmit and receive antenna gains respectively, while a motion capture tag installed with an accelerometer is mounted on one of the arms of the positioner. The tag-installed

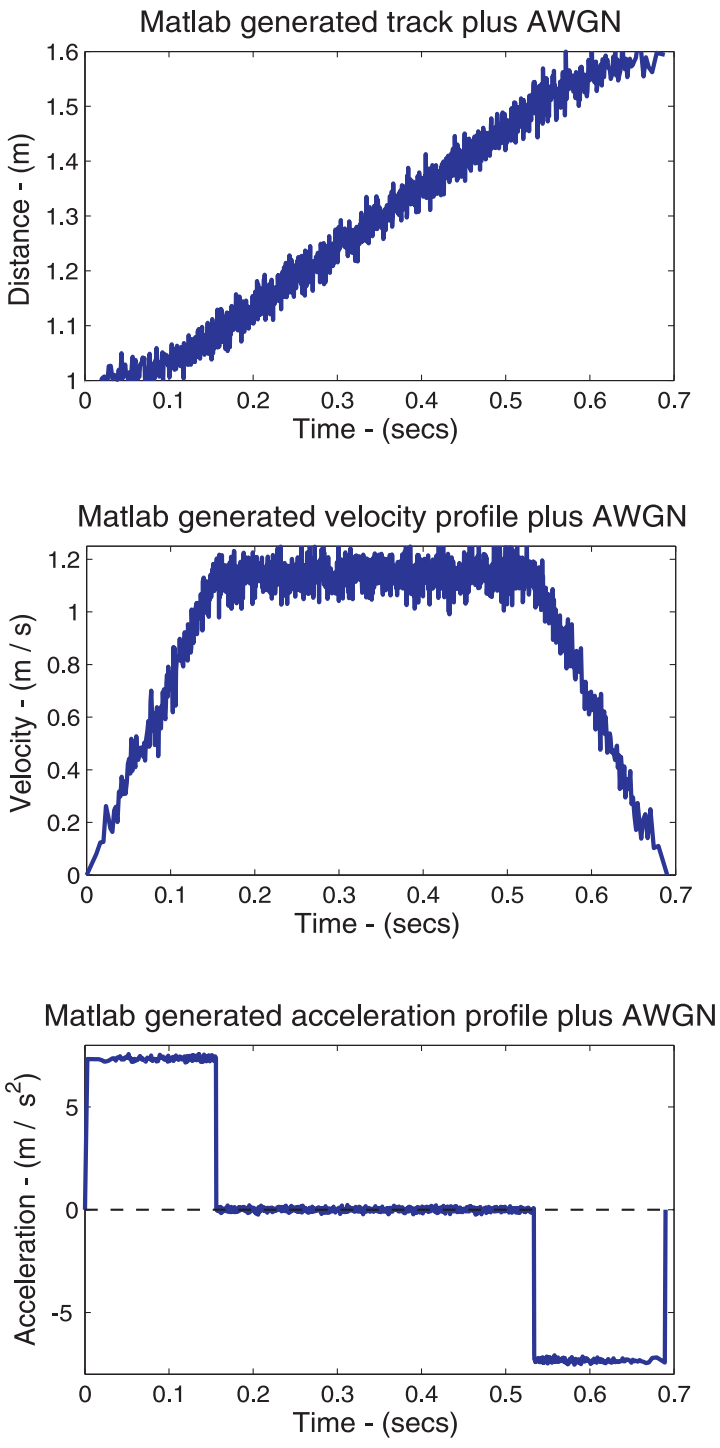

Figure 11: Gaussian white noise was added to all three profiles. The scale factors for the noise were randomly picked as 0.03, 0.08, and 0.05 for noise addition in amplitude, phase difference, and acceleration profiles respectively.

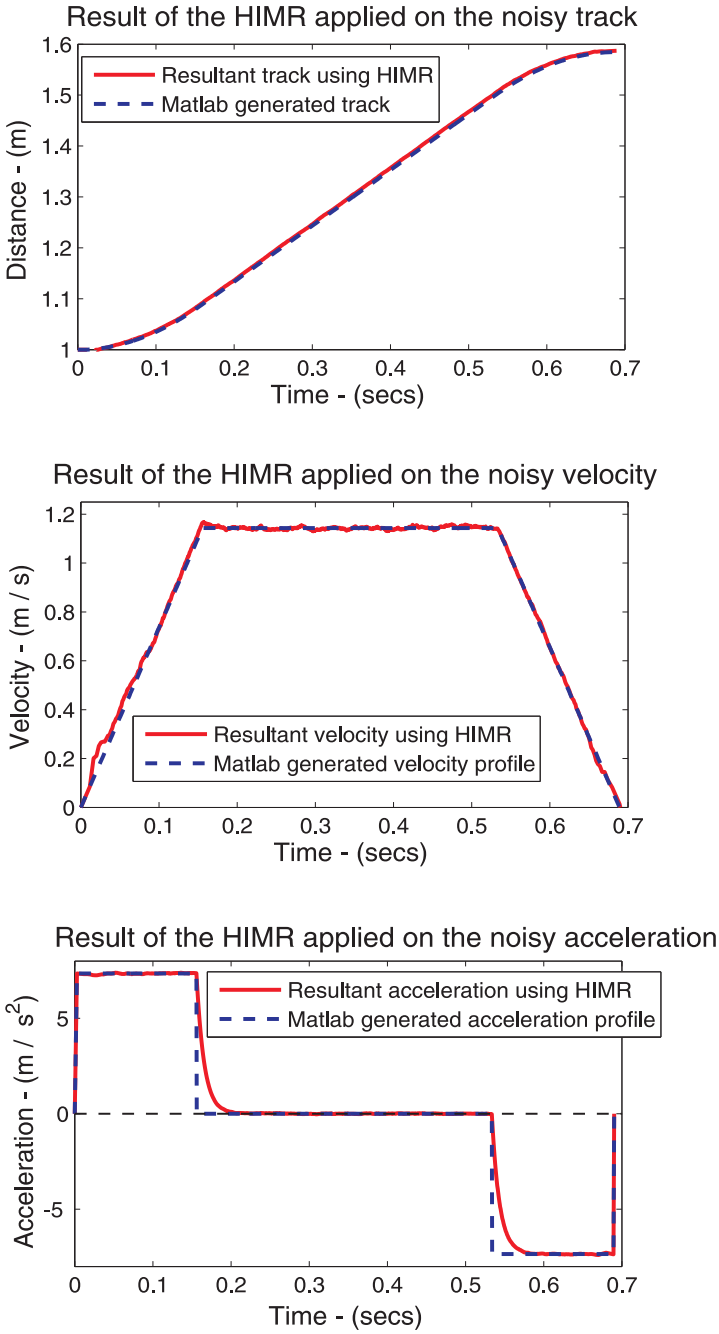

Figure 12: This figure shows the resultant curves after applying the HIMR scheme on the noisy data. The red curves closely follow the reference generated curves (blue) depicting an error of 1 mm in the position track. In practical scenario, the amount of positional error may increase but it is expected to stay within 1 - 10 mm [48].

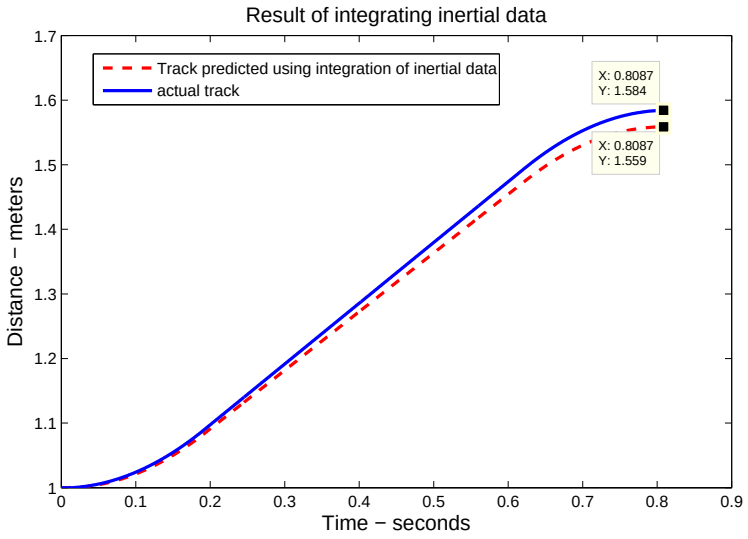

Figure 13: The noisy acceleration data generated in the simulation setup was integrated to get the position. A drift 2.5 cm was observed from the actual position over 0.6 m distance. The accumulated error will increase if observed over longer time duration.

positioner arm moves a distance of 0.61 m along a straight line away from the reader following the velocity and acceleration specifications outlined in section 2.5. It is relevant to mention that the HIMR scheme has no knowledge of the motion specifications as these are only fed as inputs to the positioner. Another important point to note is the SNR of the received signal at both end points of the motion. At a distance of 1 m away from the reader, the SNR of the received signal was 31.6 dB, while at the other end (1.61 m away) the SNR was 29.4 dB, therefore, we can safely assume this to be a high SNR scenario. The measured position, velocity and the demodulated acceleration as approximated from the received signal amplitude, packet-to-packet phase difference and backscattered accelerometer data are reproduced in Figure 14. For comparison, the measured approximated position, velocity and acceleration are plotted with the actual motion parameters undertaken by the positioner. In the next step, measured data was fed as input to the HIMR algorithm and the results are

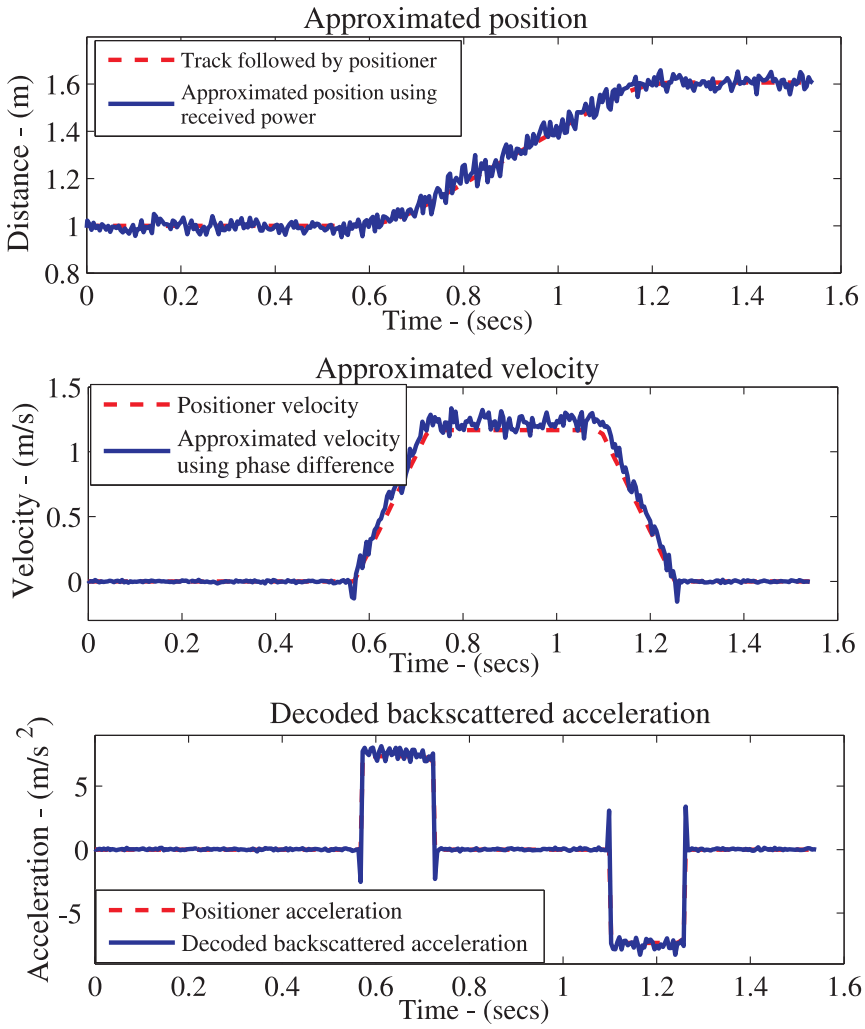

Figure 14: Comparison of measured results vs actual motion undertaken by the positioner.

plotted in Figure 15. It can be observed that the data fusion under the HIMR algorithm has smoothed the curves and reduced the error. The resultant curves closely follow the actual motion undertaken by the positioner. Since we are more interested in tracking the tagged-object, therefore we will focus on the resultant localization error. The error was computed by subtracting the actual position followed by the positioner from the position resulted using HIMR. The analysis shows a peak error of 9 mm as presented in Figure 16. The results depict that the HIMR scheme can be

used for fine-scale localization. The error margin may vary a little over longer range but a feature of the HIMR algorithm is that it continuously tries to minimize the error by predicting and correcting its estimates. It is, therefore, expected that the error will stay within millimeters of the ground truth for very long time durations.

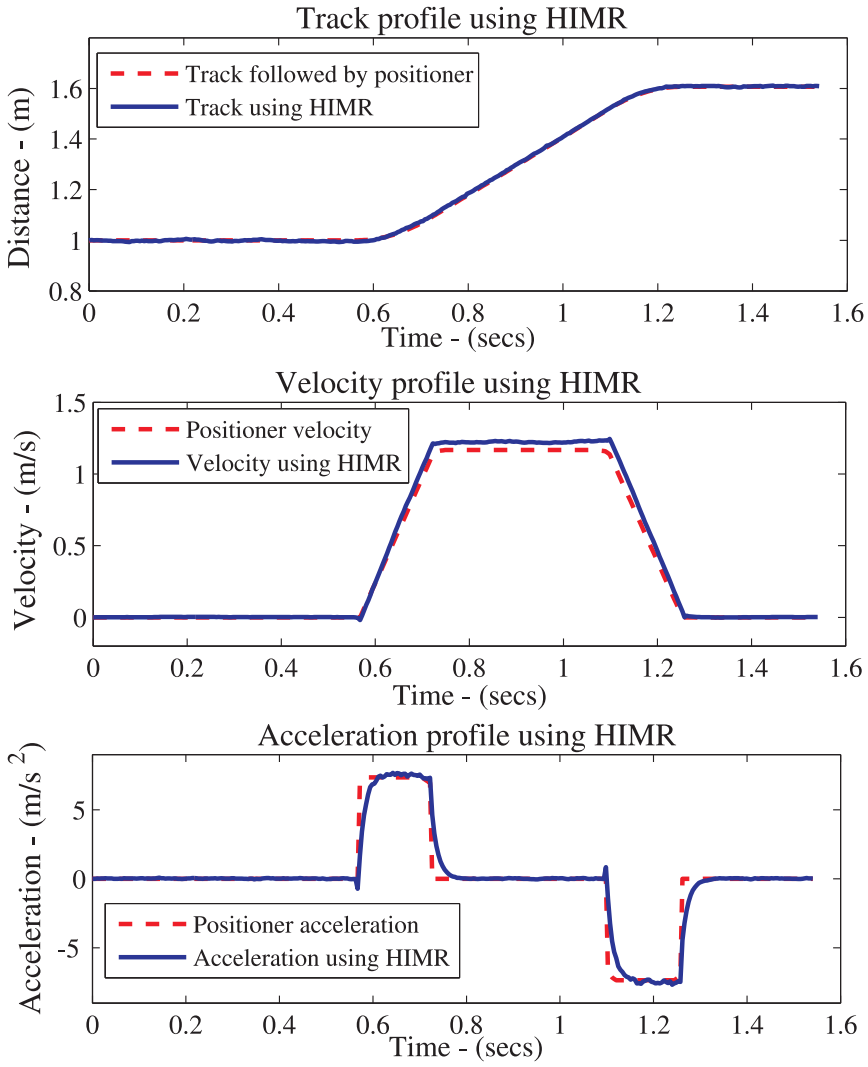

Figure 15: Co-processing the positional, velocity and acceleration data under the HIMR scheme has smoothed the measured curves and reduced the error.

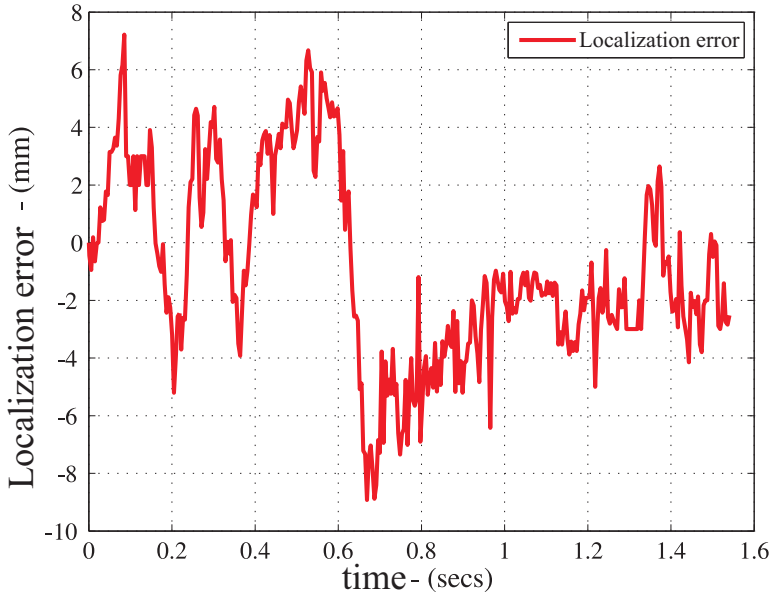

Figure 16: The error analysis on the positional data shows a peak error of 9 mm in position estimation. The results depict that the HIMR scheme can be used for fine-scale localization.

2.8 Conclusion

In this chapter, HIMR-based one-dimensional L&T scheme has been presented. The 1D-HIMR technique fused the information from three different sensors and resulted in fine-scale localization of the object without the aid of reference tags or external systems. The chapter also delved into the modeling, implementation of the HIMR scheme with hints on its extension to higher dimensions. A simulation based analysis of the HIMR scheme under noisy parameter estimation was also presented. In the end, the scheme was tested by moving the HIMR tag along a straight line using a linear positioner and analyzing its backscattered data. It was observed that the HIMR-based RFID tracking provides millimeter-scale positional tracking.

CHAPTER III

TWO-DIMENSIONAL MOTION ESTIMATION

3.1 Background

This chapter details the extension of the one-dimensional (1D) hybrid inertial microwave reflectometry (HIMR)-based object L&T scheme to two-dimensions (2D). We have presented key differences between the 1D- and 2D-HIMR schemes, design of a new 9-axis tag, the two-dimensional motion estimation setup, the theoretical model of 2D-HIMR, and the observability analysis.

Localization of objects in a plane using radio frequency identification (RFID) technology is a very useful and vital application. We briefly present an additional literature review for multi-dimensional position estimation techniques using RFID technology. A number of approaches have been proposed for multi-dimensional localization and identification using RFID technology such as [68–75]. [68] estimated the position of a surface acoustic wave (SAW)-based RFID tag by calculating the time-difference-of-arrival (TDOA) of the reflected signal from a SAW tag on three receiver stations. The receivers were installed on the corners of the field of observation and the tag position was estimated by determining the point of intersection of the ellipses drawn from each antenna. The radii of ellipses were estimated by using time delay information of the received signals. [69] presented a robot localization and orientation scheme which used a combination of RFID tags installed on the floor at known locations with angle and distance sensors installed on the robot's tag readers. Robots calibrated their on-board sensor based position by reading the tag IDs installed at known coordinates. [70, 71] introduced a complicated 2D MIMO-based localization technique of an object by simultaneously evaluating phase-of-arrival (PoA) of the backscattered

Table 4: Summary of localization accuracy.

Reference #	Accuracy range	Tag Type	Technique
Bechteler *et al.* [68]	14–21 cm	SAW tag	TDOA
Munishwar *et al.* [69]	25 cm	Gen2	Hybrid
Scherhaufl *et al.* [70, 71]	1.1–4 cm	Gen2	PoA
Miesen *et al.* [76]	2 cm	Gen2	SA
Arumugam *et al.* [73–75]	12–110 cm	MQS tag	CI theory

signals from an array of tags using an antenna array on a single reader. [76] used the concept of phase-based synthetic apertures (SA) to localize the tagged object. In this technique, the phase of the backscattered signal was pre-measured using reference tags at each location of the area of interest creating a synthetic phase picture of the area that is pre-stored into the reader. When the tagged object moved over the pre-mapped area, the phase of received signal is compared to the stored value to estimate the location. Moreover, it was assumed that the tag motion trajectory is fixed and known.

The performance of RFID tags degrades in the vicinity of lossy objects; to overcome this [72–75] proposed a multi-dimensional localization technique utilizing a low frequency quasi static magnetic field which is undisturbed in the presence of lossy objects such as a human body. In this technique, a magnetoquasistatic (MQS) field emitting loop was installed on the object of interest and a grid of receiving loops was used to measure and estimate the position using complex image (CI) theory. Table 4 summarizes the localization accuracy using the techniques mentioned above.

Besides the aforementioned position estimation techniques, a detailed breakdown of existing tag L&T schemes has been presented earlier in chapter 1 and in [48].

The 2D HIMR-scheme differs from existing L&T schemes in that it does not require reference tags, it does not require the pre-knowledge of the tag's trajectory, and it does not require the pre-mapping of the phase or amplitude behavior in the area of interest. It also does not utilize SAW or MQS tags, and it does not need antenna

arrays on the reader. Instead it uses a customized tag mounted with inertial sensors (accelerometer, gyroscope, and compass) whose data are received at three basestation readers. The HIMR tag backscatters the inertially measured data in the form of packets to the basestation readers, which decode this information and fuse it with received signal strength based radial distances, and packet-to-packet phase difference based radial velocities, to output the planar position/orientation coordinates. Later in this work, it will be shown through narrowband experiments at 5.8 GHz that the localization accuracy of 2D-HIMR converges to 1-2 cm when the tagged object is observed for two or more seconds. It is also of significance to highlight the key features that differentiate 2D-HIMR from 1D-HIMR:

1. In the formulation of 1D-HIMR modeling, the tag was considered as a point mass object whereas in the 2D-HIMR the tag will be considered a rigid body. This allows us to equip the tag with additional sensors such as a gyroscope and a magnetometer to sense the rotation and orientation of the object in addition to an accelerometer for acceleration sensing. This capability will provide extra degrees of freedom to locate and track tagged object in planar motion profile.

2. For 1D L&T using HIMR, a single pylon was used for modeling and measurements (a pylon, in these experiments, is a transmitter and receiver reader antenna and the corresponding reader hardware that connects them). The two-dimensional HIMR requires three pylons to track the tagged object in any type of planar motion. The need for three pylons ensures system observability at every possible 2D position, to aid in object localization in the plane, and to add accuracy and redundancy. For the three-dimensional HIMR experiments in the future, a four-pylon setup will be explored which allows long-range position estimation in 2D and 3D. The ability to get absolute position with mm-precision from each of the four pylons indicates operation of a 3D localization system that far surpasses any existing technology in terms of accuracy, simplicity, size,

and range.

3. As will be evident later, the mathematical model for 2D-HIMR involves nonlinearities as compared to simple linear model for the 1D case.

4. Since the 2D-HIMR requires three pylons, and additional inertial sensor therefore, the amount of sensory information for 2D L&T is more than in the 1D case.

5. The 1D-HIMR experiments are based on a 5.8 GHz backscatter tag with 6-axis accelerometer and gyroscope sensors, depicted in Figure 6. Newer integrated circuits now exist that simultaneously measure 9-axes of information: 3 dimensions of gyrometry, accelerometry, and magnetometry each. A key goal of this research is to fold these new and extra degrees of measurement into a next-generation HIMR technique.

3.2 Sensors

Pictorially the difference between 1D- and 2D-HIMR algorithm inputs is presented in Figure 17. The one-dimensional HIMR takes in three noisy inputs, approximated position, velocity, and decoded acceleration. Position and velocity is approximated using the received signal strength and packet-to-packet phase difference, while the acceleration is decoded from the accelerometer data which is part of backscatterd packet. The two dimensional HIMR uses three pylons, with the radial distance from each pylon approximated using received signal strength at each reader. Similarly, the radial velocity at each reader is approximated by evaluating packet-to-packet phase difference at each reader. In addition, three inertially sensed quantities, i.e. acceleration, angular velocity, and orientation, act as input to the 2D-HIMR algorithm. Together these nine quantities - three radial distances, three radial velocities, and

three inertially sensed quantities - are fused to output a fine-scale position coordinates estimate.

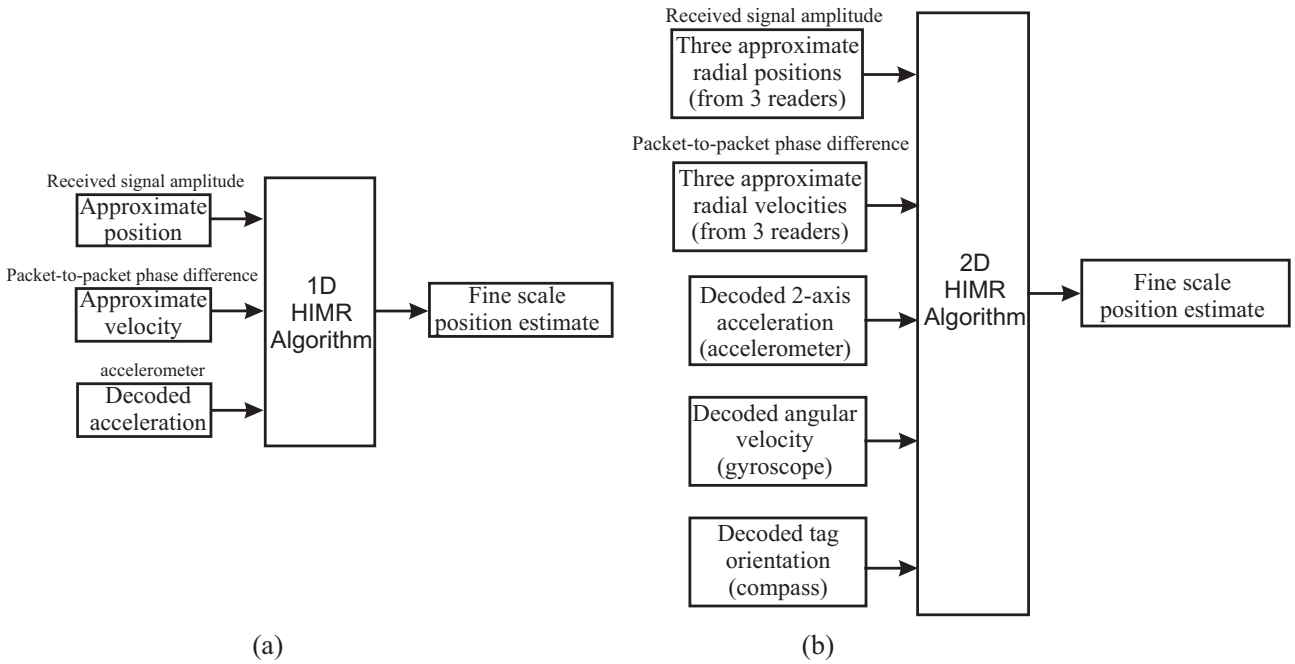

Figure 17: This figure highlights the input difference between the one- and two-dimensional HIMR scheme(a) Inputs for 1D-HIMR algorithm (b) Inputs for 2D-HIMR algorithm

3.3 New 9-axis HIMR tag

A new low power RF tag capable of sensing nine inertial quantities, i.e. three axis acceleration using a triaxial accelerometer, three axis angular rotation using a triaxial gyroscope, and three axis orientation using a triaxial magnetic compass, has been developed for multi-dimensional L&T using 2D-HIMR. A block diagram of the nine-axis HIMR tag sensor is presented in Figure 18. The tag is equipped with a single chip sensor which is connected to a microcontroller through an I2C interface. The 2D-HIMR uses a *battery-assisted* tag that periodically backscatters the data packets and expends a power of 15 mW using a 3 V, 240 mAh coin cell battery. However, the battery drainage can be reduced by introducing handshake, sleep and wake-up cycles

in an industrial or commercialized system. An InvenSense, MPU9250, 9-axis MEMS inertial device is mounted on the tag to measure nine inertial quantities mentioned above. Whereas, a Texas Instruments, MSP430F2619, microcontroller extracts the data from the inertial sensor, organizes and encodes the data in a packet form, and then backscatters the data by toggling the tag antenna through an RF switch between two known RF load states, i.e. open and short. The measured data is arranged in a structured packet illustrated in Table 5. It comprises pf a three-bytes header, a unique two-bytes tag identification code, 18-bytes inertial data, and a single-byte cyclic redundancy check (CRC) to validate the packet integrity. The packet is encoded using Binary-offset carrier (BOC) with 8 transitions per data bit. The tag chip rate is 4 Mcps with a packet rate of 141 packets per second. A data encoding scheme is desired not only to prevent bit errors but also to add coding gain to achieve a long range on the backscatter link [77].

Table 5: Arrangement of a 9-DOF backscattered data packet in the 2D-HIMR scheme.

Header	Tag ID	Accelerometer data	Gyroscope data	Compass data	CRC
3-bytes	2-bytes	6-bytes	6-bytes	6-bytes	1-byte

A photo of the developed 9-DOF tag is given in Figure 19. The size of the developed tag is 3.5 $\times$ 4.6 cm, with a connectorized antenna port to attach different kinds of directional or omni-directional antennas for testing purposes. The tag was designed and fabricated on a four layer board of FR408 substrate with $\epsilon_r = 3.66$ and $\tan\delta = 0.0127$ at 5 GHz. The layer stackup for four layer board is given in Table 6.

3.4 Two-dimensional Motion Estimation Setup

Before formulating the mathematical model for the 2D-HIMR scheme, it is necessary to understand the two dimensional motion estimation setup illustrated in Figure

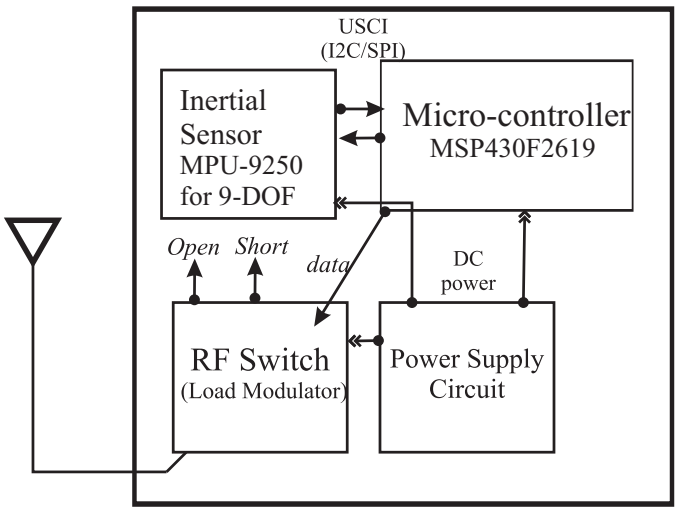

Figure 18: Block diagram of 9-DOF RF tag with single chip 9-axis sensor. A Texas Instruments, MSP430F2619, microcontroller extracts the data from the inertial sensor, MPU9250, organizes and encodes the data in a packet form, and then backscatters the data by toggling the tag antenna through an RF switch between open and short load states.

20. As mentioned earlier, the two-dimensional HIMR uses three pylons, to simultaneously receive the backscattered packets from the tag moving in a plane. At each instant of the tag's planar motion, the three pylons compute approximate radial distance and radial velocity, and decode triaxial acceleration, angular velocity and orientation angle from the received backscattered signal. Each pylon can be considered a sensory basestation that senses aforementioned quantities.

In the 2D-HIMR setup, the tag moves in a fixed coordinate system denoted by $(x,\, y)$, the location of three pylons is fixed and known, with $(x_1,\, y_1)$, $(x_2,\, y_2)$, and $(x_3,\, y_3)$ as their coordinates, respectively. The tag is considered to be a rigid body whose body axes, which are aligned with the on-board sensor's axes, are represented by $(x^B,\, y^B)$. Since the tag can rotate during planar motion, its orientation angle is of importance in its tracking. The orientation of the tag body axis with respect to the fixed plane is designated by θ_z. Accordingly, for a tag rotating around its z-axis, the angular velocity is given by ω_z. The tag accelerations along its body axes are

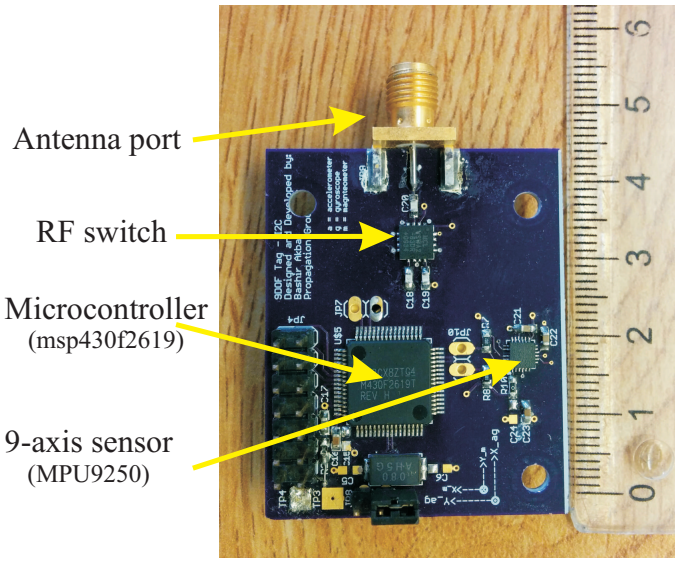

Figure 19: A photo of the developed 9-DOF RF tag with single chip 9-axis sensor. The tag was developed on a four layer board with FR408 substrate with $\epsilon_r = 3.66$ and $\tan\delta = 0.0127$ at 5 GHz.

given by a_x and a_y, which can be converted into the fixed coordinate system using a rotation matrix based on the orientation angle θ_z. The radial distance of the tag from all three readers is indicated by r_1, r_2 and r_3, respectively. The rates at which the radial distances between the tag and reader pylons changes during the tag movement are given by $\dot{r}_1$, $\dot{r}_2$ and $\dot{r}_3$, respectively.

3.4.1 Radial Distance

After introducing the aforementioned quantities, it is also essential to highlight and recap how to extract these quantities from the backscatterd signal. The radial distance between the tag and readers can be approximated using the freespace Friis equation optimized for backscatter communication given by

$$r_u \approx \sqrt[4]{\left(\frac{2P_T G_T G_R {G_t}^2 \lambda^4 M R}{(4\pi)^4 H_u^2}\right)}, \quad u = 1, 2, 3 \tag{22}$$

The transmitted power is indicated by P_T; G_T, G_R, and G_t represent the transmit, receive, and tag antenna gains; λ is the wavelength; M is the modulation index of the

Table 6: Four layer board stackup of the RF tag.

Thickness	Layer	Tolerance
1 mil	Solder resist	± 0.2 mil
1.4 mil	1 oz copper	
6.7 mil	FR408 prepreg	± 0.67 mil
0.7 mil	0.5 oz copper	
47 mil	FR408 core	± 4.7 mil
0.7 mil	0.5 oz copper	
6.7 mil	FR408 prepreg	± 0.67 mil
1.4 mil	1 oz copper	
1 mil	Solder resist	± 0.2 mil

RFID tag; R is the impedance of the RFID system; and H_u is the amplitude of the received signal at reader u. Note that in 1D-HIMR [48], the equation similar (22) was used to approximate the linear distance between the reader and the tag moving along a straight line, however, in 2D-HIMR we call it a radial distance. Approximating the radial distance alone cannot guarantee the fine-scale position estimation of the tag, as the received signal amplitude is noise-polluted. Moreover, unlike the conventional triangulation based localization where the position of an object is determined by finding a point of intersection of three ellipses or curves drawn from each receiver based on the approximated radial distances, the 2D-HIMR scheme directly relates the radial distance from each pylon to the tag's and pylon's position coordinates, respectively, and makes it part of the estimation process which will be evident in the HIMR modeling section.

3.4.2 Radial Velocity

The radial velocity of the tag, which is the rate of change of the radial distance of the tag with respect to each pylon, is approximated by computing the packet-to-packet phase difference of the backscattered signal. The RFID systems are phase coherent by nature, i.e. the phase of the backscattered signal stays constant if the tag is static and varies when the tag moves, which can be used to compute the radial

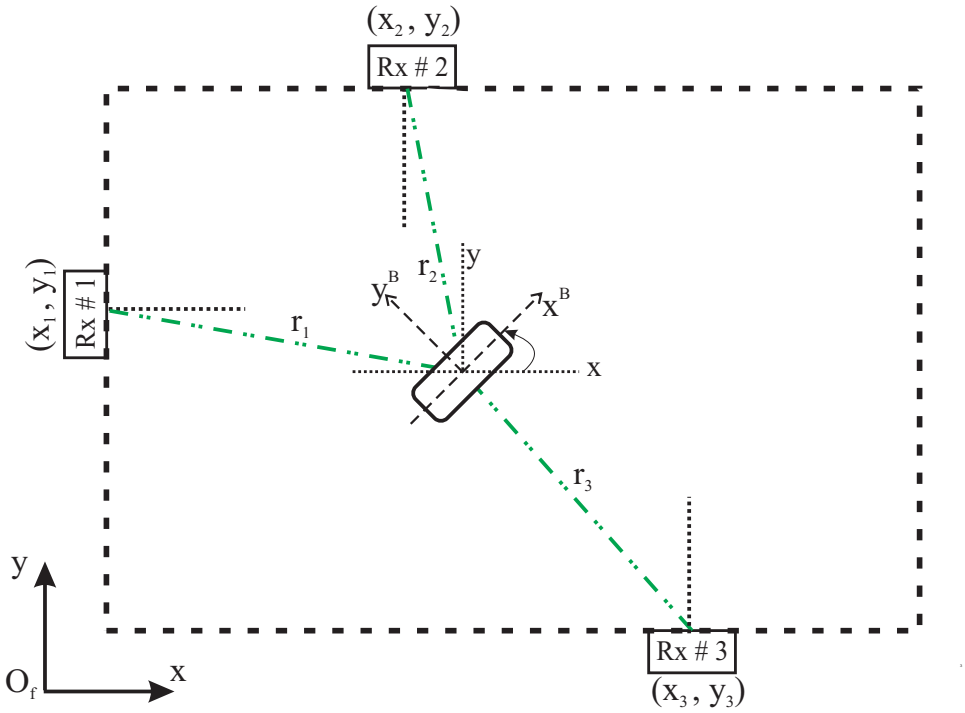

Figure 20: Two-dimensional motion estimation setup. The three 5.8 GHz RFID reader pylons are installed at known locations in a pre-defined area with fixed coordinates whose origin is defined by O_f. An RF tag considered as a rigid body with its own body axes moves in the plane. The radial distance to the tag from each pylon is defined by r_1, r_2 and r_3 respectively.

velocity of the tag by using:

$$\dot{r}_u \approx \frac{\lambda}{4\pi}\frac{\Delta\phi_{p,u}}{\Delta t}, \quad u = 1, 2, 3 \tag{23}$$

where $\Delta\phi_{p,u}$ is the propagated phase difference at reader u over the time interval Δt. Phase, in itself, is vulnerable to aliasing for a tag moving at high speeds, however, in the presence of other sensor quantities such as received signal strength and inertial measurements, the aliasing can easily be calibrated out.

3.4.3 Inertial Sensors: acceleration, angular Velocity, and orientation

In the 2D-HIMR, a low power, 9-axis sensor chip provides an approximation of triaxial acceleration, triaxial angular velocity, and orientation of the tag. The information from these sensors is part of the backscattered data packet received at each

reader. The inertial information is retrieved by demodulating and decoding the received packet; although all readers receive backscattered data packets, the inertial information need only be retrieved from one of the readers. To ensure the integrity of each packet, the CRC of the each packet is verified before the demodulation. In theory, provided the initial position and orientation are known, the acceleration and angular velocity can be integrated to get the position and angle position along the motion path but this operation will add integration drift that will increase over time. Hence, in 2D-HIMR all the noise contaminated measured quantities will be fused in a single algorithm to locate and track the tag.

3.4.4 Required Inertial Quantities

Since the tag is in a planar motion in xy-plane, in essence only the accelerations a_x and a_y along the tag's body-axes will be required, however, the information of z-axis acceleration is necessary since that is used to verify that the tag did not bump up or down during the motion, affecting the z-axis acceleration. Similarly, for a planar motion in the xy-plane, only the angular velocity ω_z around the z-axis is required. However, the angular velocities around the other two axes can be used to establish that the tag did not twist or rotate around the other two axes. Likewise, magnetometer measurements will be used to approximate the orientation θ_z of the tag during the motion.

3.5 2D HIMR–Scheme

This section explains the modeling, estimator, error dynamics, and observability analysis of the 2D-HIMR scheme.

3.5.1 Modeling

The tag is considered as a rigid body whose motion in the plane is governed by Newton's Law with respect to the fixed inertial plane in the form

$$m\ddot{x} = F_x \tag{24}$$

$$m\ddot{y} = F_y \tag{25}$$

$$I_z\ddot{\psi} = T_z \tag{26}$$

where m indicates the mass of the rigid body, $\ddot{x}$ and $\ddot{y}$ are the accelerations along the x and y-axes of the fixed inertial plane, F_x and F_y are the resultant forces applied to the mass along the x and y-axes, $\ddot{\psi}$ is the angular acceleration, and I_z and T_z are the inertial moment and resultant torque around the z-axis, respectively. The force/mass and torque/inertia ratios determine the multi-dimensional tag motion, but these are not measured or known. Moreover, this new scenario for multi-dimensional object tracking complicates the system model by adding output nonlinearities, resulting in the state-space model

$$\dot{\mathbf{x}} = \mathbf{A}\mathbf{x} + \mathbf{B}\mathbf{w} \tag{27}$$

$$\mathbf{y} = \mathbf{h}(\mathbf{x}) + \mathbf{v} \tag{28}$$

where the $\mathbf{x}$ vector is composed of the position and orientation state variables and the corresponding velocity and acceleration state variables, $\mathbf{y}$ denotes the vector of noisy sensor outputs, vector $\mathbf{h}(\mathbf{x})$ describes the nonlinear dependence between system states and noise-free sensor outputs, $\mathbf{A}$ is a 9×9 coefficient matrix, $\mathbf{B}$ is a 9×3 coefficient matrix, $\mathbf{w}$ is the disturbance vector which accounts for the forces $(\frac{\dot{F}_x}{m}, \frac{\dot{F}_y}{m})$ and torques $(\frac{\dot{T}_z}{I_z})$ causing tag motion, and $\mathbf{v}$ is vector of sensor noise signals.

The state and output vectors $\mathbf{x}$ and $\mathbf{y}$ are written as

$$\mathbf{x} = \begin{bmatrix} x & \dot{x} & \ddot{x} & y & \dot{y} & \ddot{y} & \psi & \dot{\psi} & \ddot{\psi} \end{bmatrix}'$$

$$\mathbf{y} = \begin{bmatrix} r_1 & \dot{r}_1 & r_2 & \dot{r}_2 & r_3 & \dot{r}_3 & \theta_z & \omega_z & a_x & a_y \end{bmatrix}'$$

where x and y denote the position coordinates and ψ denotes the noiseless orientation

angle, expressed in the fixed reference frame. According to Figure 20, the state-to-output map has the form

$$\mathbf{h}(\mathbf{x}) = \begin{bmatrix} h_1 & \dot{h}_1 & h_2 & \dot{h}_2 & h_3 & \dot{h}_3 & h_4 & h_5 & h_6 & h_7 \end{bmatrix}'$$

where

$$\begin{aligned} h_u &= \sqrt{(x - x_u)^2 + (y - y_u)^2}, \quad u = 1, 2, 3 \\ \dot{h}_u &= \frac{(x - x_u)\dot{x} + (y - y_u)\dot{y}}{\sqrt{(x - x_u)^2 + (y - y_u)^2}}, \quad u = 1, 2, 3 \\ h_4 &= \psi \\ h_5 &= \dot{\psi} \\ h_6 &= \ddot{x}\cos\psi + \ddot{y}\sin\psi \\ h_7 &= -\ddot{x}\sin\psi + \ddot{y}\cos\psi \end{aligned}$$

The coefficient matrices are

$$\mathbf{A} = \begin{bmatrix} 0 & 1 & 0 & 0 & 0 & 0 & 0 & 0 & 0 \\ 0 & 0 & 1 & 0 & 0 & 0 & 0 & 0 & 0 \\ 0 & 0 & 0 & 0 & 0 & 0 & 0 & 0 & 0 \\ 0 & 0 & 0 & 0 & 1 & 0 & 0 & 0 & 0 \\ 0 & 0 & 0 & 0 & 0 & 1 & 0 & 0 & 0 \\ 0 & 0 & 0 & 0 & 0 & 0 & 0 & 0 & 0 \\ 0 & 0 & 0 & 0 & 0 & 0 & 0 & 1 & 0 \\ 0 & 0 & 0 & 0 & 0 & 0 & 0 & 0 & 1 \\ 0 & 0 & 0 & 0 & 0 & 0 & 0 & 0 & 0 \end{bmatrix}, \quad \mathbf{B} = \begin{bmatrix} 0 & 0 & 0 \\ 0 & 0 & 0 \\ 1 & 0 & 0 \\ 0 & 0 & 0 \\ 0 & 0 & 0 \\ 0 & 1 & 0 \\ 0 & 0 & 0 \\ 0 & 0 & 0 \\ 0 & 0 & 1 \end{bmatrix}$$

3.5.2 Estimation

The problem of estimating the states of a dynamical system from outputs and possibly inputs (commonly known as observing the state, hence the name observer) is an important problem in the theory of systems [78]. For linear systems, this problem

has been extensively studied and the results developed are complete. For nonlinear systems, the theory of observers is not as complete or successful. A number of methods have been proposed, such as (i) Lyapunov-based method [79], (ii) extended linearization method [80], (iii) Lie-algebraic approach [81], and (iv) nonlinear least-squares-based estimation [82]. Each of these approaches has its own pros and cons. The Lyapunov-based methods are complicated and require a trial and error search for a Lyapunov function. The extended linearization approach relies on an equilibrium manifold and hence may fail when quasi steady-state operation does not apply. The Lie-algebraic approach reduces the nonlinear observer problem to one that can be handled by linear techniques; the drawbacks are that for this technique to be applicable, the nonlinear system must satisfy non-generic conditions [83] (not mentioned here), and even when this is so, finding the necessary state transformation will most likely be a difficult problem in itself.

In this work, a very simple approach is presented for state estimation of system (27)–(28). The state estimator will be constructed by neglecting the presence of $\mathbf{w}$ and $\mathbf{v}$ in (27) and (28), since these signals are not known or measured. The estimated value of the unmeasured state vector $\mathbf{x}$, which is denoted by $\hat{\mathbf{x}}$, will be obtained by solving the differential equation

$$\dot{\hat{\mathbf{x}}} = \mathbf{A}\hat{\mathbf{x}} - \mathbf{L}\left(\hat{\mathbf{y}} - \mathbf{y}\right) \tag{29}$$

$$\hat{\mathbf{y}} = \mathbf{h}(\hat{\mathbf{x}}) \tag{30}$$

as time evolves. The estimator state equation (29) incorporates a copy of state equation (27) with $\mathbf{w} = 0$, and the estimator output equation (30) is a copy of output equation (28) with $\mathbf{v} = 0$. The assignable gain matrix $\mathbf{L}$ multiplies the output error $\hat{\mathbf{y}} - \mathbf{y}$, and hence two terms combine in (29) to determine future values of $\hat{\mathbf{x}}$; neither of these terms is sufficient individually, since one neglects $\mathbf{w}$ and one neglects $\mathbf{v}$. Gain matrix $\mathbf{L}$ may be adjusted to trade off these competing imperfections; a larger $\mathbf{L}$ is

desired if $\mathbf{w}$ is larger than $\mathbf{v}$, and a smaller $\mathbf{L}$ is desired if $\mathbf{w}$ is smaller than $\mathbf{v}$. The 9×10 gain matrix $\mathbf{L}$ would be preferably constant, in order to maintain simplicity of implementation; analysis leading to its appropriate choice is provided in the following section.

The estimator gain matrix $\mathbf{L}$, assumed here to be constant, must be chosen such that $\hat{\mathbf{x}}$ remains bounded and converges to a suitably small neighborhood of the unmeasured state $\mathbf{x}$ as time proceeds. One complication that arises in the gain selection process is the nonlinearity of $\mathbf{h}(\mathbf{x})$. For the proof-of-concept experiments presented in this work, we have relied on the classical result that the qualitative behavior of the estimation error $(\hat{\mathbf{x}} - \mathbf{x})$, which satisfies a nonlinear time-varying differential equation, is determined by the eigenvalues of the matrix $\mathbf{A} - \mathbf{L}\mathbf{C}(\mathbf{x})$ where $\mathbf{C}(\mathbf{x})$ is the Jacobian matrix associated with $\mathbf{h}(\mathbf{x})$ at $\mathbf{x}$, provided that the rate-of-change of $\mathbf{x}$ is sufficiently small. By analysis, we established that the frozen-in-time eigenvalues remained inside the open left-half of the complex plane for all anticipated values of $\mathbf{x}$, provided that the constant matrix $\mathbf{L}$ is obtained by solving a matrix Riccati equation using a straightforward selection of tuning parameters. Stability analysis using the linearization method, for time-invariant and slowly-varying time-varying systems (as in this case), is discussed in [84].

A signal flow diagram of the motion system and its estimator is shown in Figure 21.

3.5.3 Error Dynamics

The state estimation error is defined by $\mathbf{e} = \hat{\mathbf{x}} - \mathbf{x}$. Differentiating $\mathbf{e}$ and using (27) and (29) results in

$$\dot{\mathbf{e}} = \mathbf{A}\mathbf{e} - \mathbf{L}(\mathbf{h}(\mathbf{e} + \mathbf{x}) - \mathbf{h}(\mathbf{x})) - \mathbf{B}\mathbf{w} + \mathbf{L}\mathbf{v} \tag{31}$$

which is a nonlinear differential equation forced by $\mathbf{w}$ and $\mathbf{v}$, and parameterized by $\mathbf{x}$. Since $\mathbf{w}$ and $\mathbf{v}$ are exogenous signals, they will not influence estimator stability

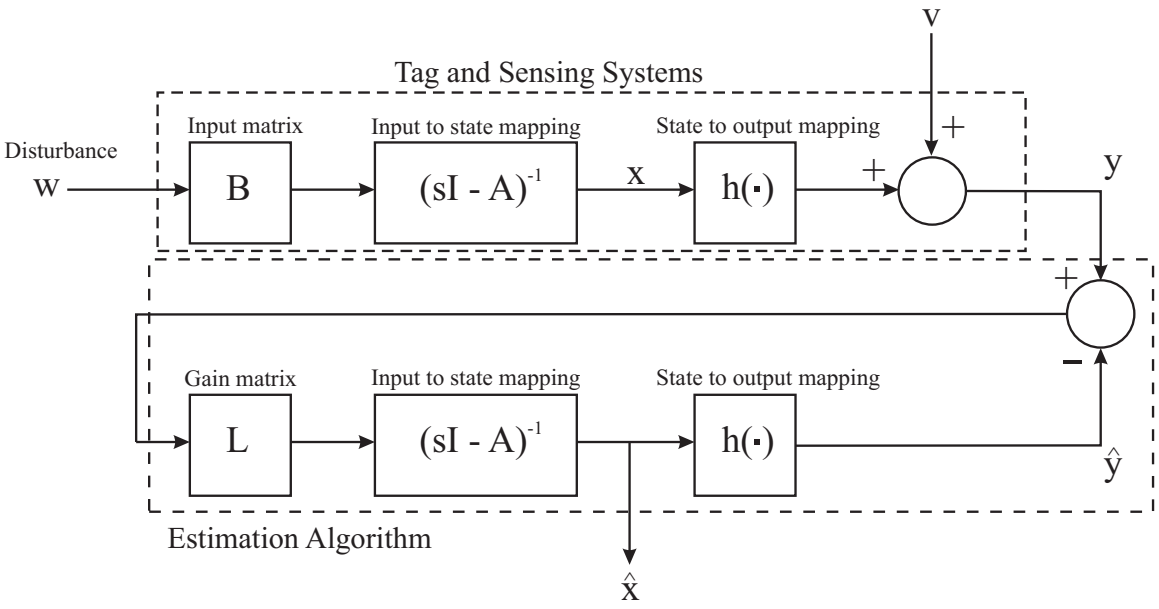

Figure 21: Signal flow diagram of motion system and its estimator.

(even if they do influence estimator performance). Hence, focusing on the special case $\mathbf{w} = 0$ and $\mathbf{v} = 0$, the unforced nonlinear estimation error dynamics

$$\dot{\mathbf{e}} = \mathbf{A}\mathbf{e} - \mathbf{L}(\mathbf{h}(\mathbf{e} + \mathbf{x}) - \mathbf{h}(\mathbf{x})) \tag{32}$$

has an equilibrium point at $\mathbf{e} = 0$, irrespective of $\mathbf{x}$ which may vary with time, since at this point the term $\mathbf{h}(\mathbf{e} + \mathbf{x}) - \mathbf{h}(\mathbf{x})$ reduces to zero. For estimator design, the goal is to determine, if possible, a constant matrix $\mathbf{L}$ such that the equilibrium point of (32) at $\mathbf{e} = 0$ is (locally) exponentially stable. According to Lyapunov's indirect method, this goal will be achieved if the linear approximation of (32) at $\mathbf{e} = 0$ has all eigenvalues in the open left-half of the complex plane. The coefficient matrix of the unforced linear approximate model is

$$\left.\frac{\partial \dot{\mathbf{e}}}{\partial \mathbf{e}}\right|_{\mathbf{e}=0} = \mathbf{A} - \mathbf{L}\mathbf{C}(\mathbf{x}) \tag{33}$$

where

$$\mathbf{C}(\mathbf{x}) = \frac{\partial \mathbf{h}}{\partial \mathbf{x}} \tag{34}$$

where in the rest of the text $\mathbf{C}(\mathbf{x})$ will be wriiten as $\mathbf{C}$ for the sake of simplicity. The stability of the error dynamics at equilibrium point $\mathbf{e} = 0$ is given by

$$\begin{aligned}\dot{\mathbf{e}} &= \mathbf{A}\mathbf{e} - \mathbf{L}(\mathbf{h}(\mathbf{x}+\mathbf{e}) - \mathbf{h}(\mathbf{x})) \\ &= \left(\mathbf{A} - \mathbf{L}\frac{\partial \mathbf{h}(\mathbf{x})}{\partial \mathbf{x}}\right)\mathbf{e} \\ &= (\mathbf{A} - \mathbf{L}\mathbf{C})\,\mathbf{e}\end{aligned} \tag{35}$$

where $\frac{\partial \mathbf{h}(\mathbf{x})}{\partial \mathbf{x}} = \mathbf{C}$. According to (35), the estimator is stable if and only if all eigenvalues of $(\mathbf{A} - \mathbf{L}\mathbf{C})$ are in the open left half plane. The $\mathbf{C}$ can be found by carefully choosing points in the fixed coordinate system with zero velocities and accelerations, but $\mathbf{L}$ remains as a design variable that may be adjusted to meet this stability requirement. Determining a stabilizing $\mathbf{L}$, given $\mathbf{A}$ and $\mathbf{C}$, is always possible provided that the matrix pair (A, C) satisfies observability property, which will now be defined. Assuming that $\dim\{\mathbf{x}\} = n$ and $\dim\{\mathbf{y}\} = p$, the so-called observability matrix

$$\mathbf{O} = \begin{bmatrix} \mathbf{C} \\ \mathbf{C}\mathbf{A} \\ \vdots \\ \mathbf{C}\mathbf{A}^{n-1} \end{bmatrix} \tag{36}$$

has np rows and n columns. The matrix pair $(\mathbf{A}, \mathbf{C})$ is observable if and only if $\text{rank}\{\mathbf{O}\} = n$.

3.5.4 The C–Matrix

As discussed earlier the $\mathbf{C}$ matrix can be calculated by finding the Jacobian of the output equation $\mathbf{h}(\mathbf{x})$ given by

$$\mathbf{C} = \frac{\partial \mathbf{h}(\mathbf{x})}{\partial \mathbf{x}} \tag{37}$$

which yields the following 10×9 matrix:

$$\mathbf{C} = \begin{bmatrix} C_{11} & 0 & 0 & C_{14} & 0 & 0 & 0 & 0 & 0 \\ C_{21} & C_{22} & 0 & C_{24} & C_{25} & 0 & 0 & 0 & 0 \\ C_{31} & 0 & 0 & C_{34} & 0 & 0 & 0 & 0 & 0 \\ C_{41} & C_{42} & 0 & C_{44} & C_{45} & 0 & 0 & 0 & 0 \\ C_{51} & 0 & 0 & C_{54} & 0 & 0 & 0 & 0 & 0 \\ C_{61} & C_{62} & 0 & C_{64} & C_{65} & 0 & 0 & 0 & 0 \\ 0 & 0 & C_{73} & 0 & 0 & C_{76} & C_{77} & 0 & 0 \\ 0 & 0 & C_{83} & 0 & 0 & C_{86} & C_{87} & 0 & 0 \\ 0 & 0 & 0 & 0 & 0 & 0 & C_{97} & 0 & 0 \\ 0 & 0 & 0 & 0 & 0 & 0 & 0 & C_{108} & 0 \end{bmatrix} \tag{38}$$

Each entry of the equation (38) is given in appendix B.

3.5.5 Observability Analysis

The observability matrix calculated using $\mathbf{C}$ and $\mathbf{A}$ in (36) is given in appendix B. The coefficient matrix $\mathbf{A}$ is a *nilpotent* whose $\mathbf{A}^3$ is all zeros, therefore, the size of the observability matrix is 30×9. To find whether the observability matrix has full rank, we can reduce it to row echelon form, which may not be a suitable approach since it may involve dividing certain rows by a factor which under some conditions could be zero resulting in an undefined number. The other approach is to carefully choose certain rows to solve for a nonzero determinant of the observability matrix, implying that the matrix has a full rank. However, different combinations of rows could result in a long and complicated determinant form. The goal is to find a simplest nonzero determinant by carefully choosing different combinations of the matrix rows. It was found during the analysis that the test setup is composed of three readers but the system is observable under any choice of two receivers. This allows flexibility to observability analysis such that if the determinant is zero at a certain point on the

straight line joining the two readers, then by choosing another combination of the readers, it is ensured that the system stays observable. The simplest formulation of the determinants for all combinations of the readers is given in (39)–(44)

3.5.5.1 Receiver 1 and Receiver 2

For the combination of the receivers 1 and 2, the determinant is

$$D1 = -C_{97}{C_{108}}^2 \left(C_{11}C_{34} - C_{14}C_{31}\right)^3 \tag{39}$$

where $D1$ is the determinant formed by choosing rows $R1$, $R3$, $R9$, $R10$, $R11$, $R13$, $R20$, $R21$, and $R23$ of the observability matrix (97). Using the definitions of the $\mathbf{C}$ matrix entries from appendix B, the determinant $D1$ is more elaborately written as

$$D1 = \left(\left(\frac{x - x_1}{h_1}\right)\left(\frac{y - y_2}{h_2}\right) - \left(\frac{y - y_1}{h_1}\right)\left(\frac{x - x_2}{h_2}\right)\right)^3 \tag{40}$$

The determinant $D1$ is zero at the coordinates $\left(\frac{x_1+x_2}{2}, \frac{y_1+y_2}{2}\right)$, which is the midpoint on the straight line joining receivers 1 and 2, in which case the system is still observable by using the other pair of receivers 2 and 3 or receivers 1 and 3.

3.5.5.2 Receiver 2 and Receiver 3

For the combination of the receivers 2 and 3, the determinant is

$$D2 = -C_{97}{C_{108}}^2 \left(C_{31}C_{54} - C_{34}C_{51}\right)^3 \tag{41}$$

where $D2$ is the determinant formed by choosing rows $R3$, $R5$, $R9$, $R10$, $R13$, $R15$, $R20$, $R23$, and $R25$ of the observability matrix (97). Using the definitions of the $\mathbf{C}$ matrix entries from appendix B, the determinant $D2$ is more elaborately written as

$$D2 = \left(\left(\frac{x - x_2}{h_1}\right)\left(\frac{y - y_3}{h_2}\right) - \left(\frac{y - y_2}{h_1}\right)\left(\frac{x - x_3}{h_2}\right)\right)^3 \tag{42}$$

Similar to the previous case, the determinant $D2$ is zero at the coordinates $\left(\frac{x_2+x_3}{2}, \frac{y_2+y_3}{2}\right)$, which is the midpoint on the straight line joining receivers 2 and 3, in which case the system is still observable by using the combination of other pair of receivers 1 and 2 or receivers 1 and 3.

3.5.5.3 Receiver 1 and Receiver 3

For the combination of the receivers 1 and 3, the determinant is

$$D3 = -C_{97}{C_{108}}^2 \left(C_{11}C_{54} - C_{14}C_{51}\right)^3 \tag{43}$$

where $D3$ is the determinant formed by choosing rows $R1$, $R5$, $R9$, $R10$, $R11$, $R15$, $R20$, $R21$, and $R25$ of the observability matrix (97). Using the definitions of the $\mathbf{C}$ matrix entries from appendix B, the determinant $D3$ is more elaborately written as

$$D3 = \left(\left(\frac{x - x_1}{h_1}\right)\left(\frac{y - y_3}{h_2}\right) - \left(\frac{y - y_1}{h_1}\right)\left(\frac{x - x_3}{h_2}\right)\right)^3 \tag{44}$$

Likewise, the determinant $D3$ is zero at the coordinates $\left(\frac{x_1+x_3}{2}, \frac{y_1+y_3}{2}\right)$, which is the midpoint on the straight line joining receivers 1 and 3, in which case the system is still observable by using the combination of other pair of receivers 1 and 2 or receivers 2 and 3.

3.5.6 Riccati Equation

The steps to find the gain matrix $\mathbf{L}$ are similar to the 1D-HIMR case, which are as follows:

1. Assign tuning matrices $\mathbf{W}$ and $\mathbf{V}$ satisfying

$$\mathbf{W} = \mathbf{W}' > 0, \quad \mathbf{V} = \mathbf{V}' > 0. \tag{45}$$

2. Obtain matrix $\mathbf{Y}$ by solving

$$\mathbf{A}\,\mathbf{Y} + \mathbf{Y}\mathbf{A}' - \mathbf{Y}\mathbf{C}'\mathbf{V}^{-1}\mathbf{C}\mathbf{Y} + \mathbf{W} = 0. \tag{46}$$

3. Obtain matrix $\mathbf{L}$ by solving

$$\mathbf{L} = \mathbf{Y}\mathbf{C}'\mathbf{V}^{-1}. \tag{47}$$

The matrices $\mathbf{W}$ and $\mathbf{V}$ are supposed to be real-valued, symmetric and positive definite; this means that (i) the quadratic forms $\alpha'\mathbf{W}\alpha$ and $\alpha'\mathbf{V}\alpha$ evaluate to strictly positive scalar values for every nonzero real-valued vector α, and (ii) the eigenvalues of $\mathbf{W}$ and $\mathbf{V}$ are all real-valued and strictly positive. Any choices satisfying (45) will guarantee estimator stability, so even diagonal matrices may be used in practice, as shown in the experimental results below. If the unmodeled disturbance $\mathbf{w}$ and the sensor noise $\mathbf{v}$ have been statistically characterized, then $\mathbf{W}$ and $\mathbf{V}$ may be interpreted as corresponding covariance (or tuning) matrices, in which case the matrix $\mathbf{L}$ determined in (47) can be shown to minimize the steady-state covariance of the estimation error. Once $\mathbf{W}$ and $\mathbf{V}$ have been statistically evaluated or otherwise assigned, $\mathbf{Y}$ is obtained by solving the continuous-time algebraic Riccati equation (46); numerical methods for this calculation are available, e.g. function `care` of the MATLAB Control System Toolbox.

3.5.7 Model Reduction to One-dimensional Case

Assuming the tag to be a point mass object moving along a straight line on the x-axis towards reader # 1, then the $\mathbf{h}(\mathbf{x})$ vector only consists of h_1, $\dot{h}_1$, and h_4. Since, in the 1D-case we only used one reader, therefore, h_2, $\dot{h}_2$, h_3, and $\dot{h}_3$ are not required. Also, the tag is assumed to be a point mass with $\psi = 0$ implying that h_5, h_6 and h_7 are also zero. Moreover, the $\mathbf{x}$ vector also reduces to x, $\dot{x}$, and $\ddot{x}$. The modified definition of the entries of the reduced $\mathbf{h}(\mathbf{x})$ vector are given as

$$h_1 = x - x_1 \tag{48}$$

$$\dot{h}_1 = \dot{x} \tag{49}$$

$$h_4 = \ddot{x} \tag{50}$$

Finding the Jacobian of $\mathbf{h}(\mathbf{x})$, the coefficient matrix $\mathbf{C}$, and the reduced coefficient matrices $\mathbf{A}$ and $\mathbf{B}$ are given as

$$A = \begin{bmatrix} 0 & 1 & 0 \\ 0 & 0 & 1 \\ 0 & 0 & 0 \end{bmatrix}, \quad B = \begin{bmatrix} 0 \\ 0 \\ 1 \end{bmatrix}, \quad C = \begin{bmatrix} 1 & 0 & 0 \\ 0 & 1 & 0 \\ 0 & 0 & 1 \end{bmatrix} \tag{51}$$

These are exactly the same matrices used for 1D-HIMR in [48] and fulfill the observability criteria, proving the generality of the proposed 2D-HIMR model.

CHAPTER IV

EXPERIMENTS AND ANALYSIS

4.1 Experimental Setup

This chapter explains the experimental layout, the equipment used, the experimental results, and their analysis. Seven different cases were discussed during the analysis where a localization accuracy between 10 - 21 mm was achieved for x and y position coordinates respectively for a tag accelerating and decelerating at 5 m/s^2 in an interval of less than 2 s.

The layout consists of three 5.8 GHz RFID systems in the arrangement illustrated in Figure 22. The three readers were arranged in such away that the tag is continuously illuminated by all the readers throughout its motion. The readers operated on three different frequencies of 5.79 GHz, 5.8 GHz and 5.81 GHz, to avoid mutual interference. The readers were also time synchronized using a common reference and timing source for simultaneous measurements. The experiment was conducted in a rectangular area of 4 $\times$ 3 meters on the roof of the Van Leer building. The lower left edge of the area is considered as the origin of the fixed xy-coordinate system. The location of the readers is given in Table 7. A 9-DOF tag was installed on one edge of 0.31 m long boom mounted on top of a motor shaft.

The motor rotates the boom in the horizontal plane at a pre-programed speed in both counterclockwise and clockwise directions, however, during the analysis and presentation of results, only one stroke of the complete 360° rotation in counterclockwise direction will be considered. This is shown by the circular track inside the rectangular area of interest in Figure 22. The dotted portion of the first quarter of circular track in the figure is to emphasize the fact that the radial distance of the tag

with respect to each reader changes during the course of the motion. The reason to choose a circular motion, which is just a single instance of generic planar motion, is to ensure that measurements from all the sensors aboard the tag could be utilized for the position estimation, since in a circular motion all the inertial sensors, i.e. the accelerometer, the gyroscope and the compass, would be affected respectively. A photo of the experimental setup is shown in Figure 23.

An omnidirectional monopole antenna was used on the tag for continuous tag illumination and backscatter of the tag data during its rotation. The motion apparatus fixture consists of a motor mounted on heavy metal plates to avoid unnecessary jitter during the rotation, moreover, it was also ensured that the boom is horizontally level.

Table 7: Location coordinates of the three RFID systems.

RFID System #	Location (x,y) - m
1 – (x_1,y_1)	(-0.1, 1.5)
2 – (x_2,y_2)	(2, 3.05)
3 – (x_3,y_3)	(2.7, -0.03)

4.1.1 Motor's Motion Trajectory

The motor was programmed to follow a trapezoidal motion profile in the horizontal plane during one complete revolution, i.e. initially static, it accelerates up to a target velocity, then cruises with uniform speed for a small period of time, and then decelerates back to a static condition. It is pertinent to note that although the motor is pre-programmed to move at certain velocity and acceleration, none of this information is known to the readers for position estimation. The localization is solely based on the available sensory information explained earlier in the modeling section. The mathematical details of the motor's motion trajectory are given in appendix C.

For the experiment, the motor was programed to accelerate and decelerate for 0.5 s respectively, whereas it cruised for 0.2 s. However, there was a slight delay of 150 ms between the programmed reference trajectory and the one actually undertaken

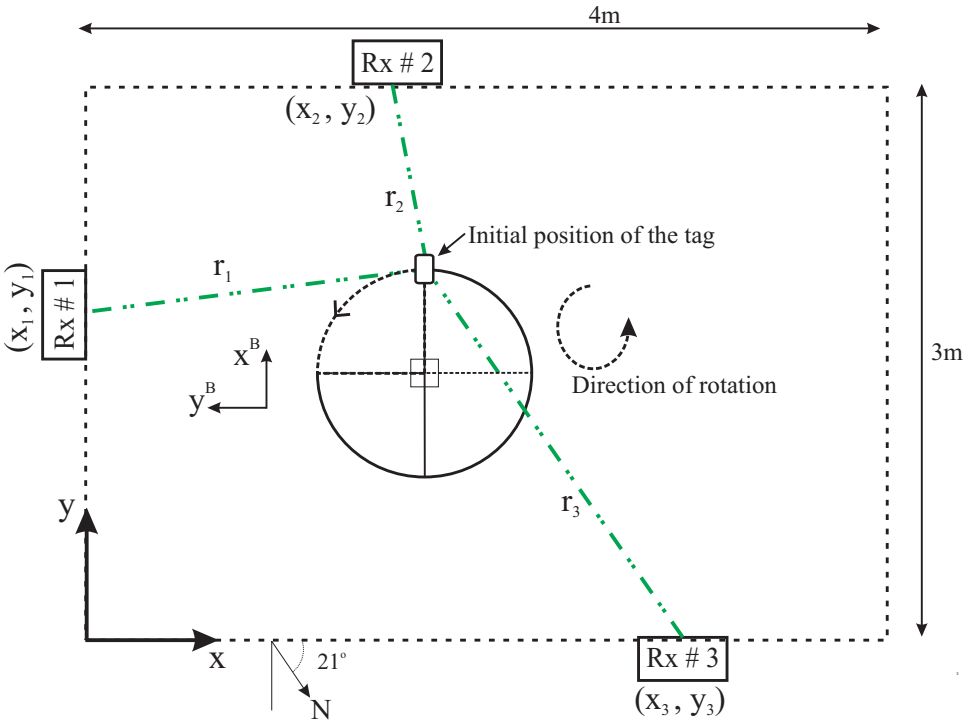

Figure 22: Illustration of the experimental setup to test planar HIMR theory. The measurements were made in a rectangular area of 4 × 3 m. The readers were installed at the positions given in the Table 7. The tag is installed on one edge of a motor mounted boom that moves the tag in a circular track as depicted above. The radial distances from each pylon varies as the tag rotates.

by the motor. The programmed vs the actual trajectory followed by the motor are presented in Figure 24. All the results will be compared with the actual trajectory undertaken by the motor.

4.1.2 Readers Network

This subsection explains the networking details of the three RFID systems. Each RFID system is composed of a pair of transceiver antennas connected to a transceiver board whose inphase (I) and quadrature phase (Q) outputs go to the universal software radio peripheral (USRP) device for signal processing. All the three USRPs are required to be synchronized through common 10 MHz reference and 1 pulse per second (PPS) timing signals to have time synchronized measurements. The processed

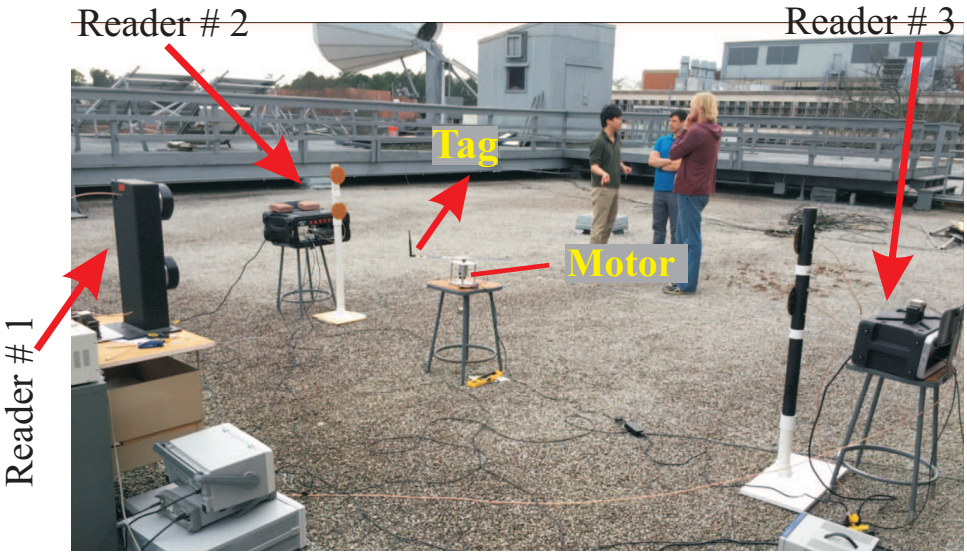

Figure 23: Picture of the experimental layout on the roof top of the Van Leer building. A rectangular area of 4 × 3 m was marked on the roof and the RFID systems were positioned on the three sides of the area for the position estimation. The tag is installed on a boom on top of motor placed inside rectangular area. The tag rotates with motor at pre-programed trapezoidal motion profile.

data from each USRP device is simultaneously collected on a single host computer through a gigabit Ethernet connection. A block diagram of the network is provided in Figure 25. For the purpose of the experiment, the 10 MHz reference signal was generated using an external signal generator by installing a three way 0° RF splitter at its output to provide one reference to each USRP. Whereas, the 1 PPS signal was provided through a three channel arbitrary waveform generator. Both the arbitrary waveform generator and the signal generator shared a common 10 MHz reference clock for synchronized signal generation.

In a practical scenario, many other methods can be used to make meaningful measurements without synchronizing the readers with a single reference source. One example is to add a particular sequence in each backscattered packet that can be used to relate the packets decoded at each reader. This is similar to time-stamping the packets and will help in computing the correct phase, amplitude and inertial

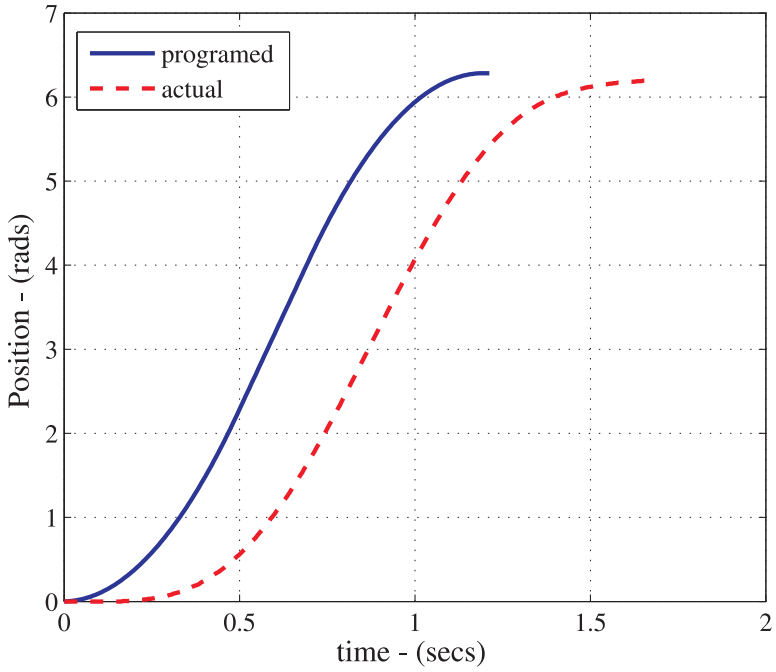

Figure 24: Comparison of the programmed reference trajectory vs the actual trajectory undertaken by the motor.

information at a particular instant. It will also help to avoid expensive equipment and long cables required in readers synchronization and make the system more deployable for practical measurements.

4.2 Experimental Results

This section presents a breakdown of the experimental results of the 2D-HIMR theory. The motor spins the tag whose backscattered data is received at three time synchronous readers. In this work, the data is time stamped and recorded for post processing. The position of the tag will be expressed in terms of its (x, y) coordinates and its orientation. Seven different cases were studied to analyze different aspects of the algorithm, where all cases are variant of the main case (Case 1) as briefly introduced below.

- Case 1–All Measured Data: This is the most fundamental case in which it is

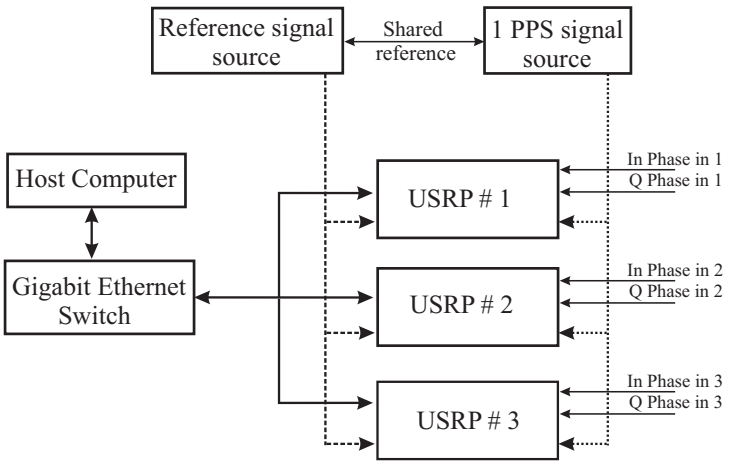

Figure 25: Network of the USRP devices in three RFID systems. All the devices share the same 10 MHz reference signal and 1 PPS timing signal to synchronously make the measurements.

assumed that all the sensed data is always available for the position estimation. Therefore, the data from all the RF and inertial sensors will be used to estimate the position of the tag.

- Case 2–Repetition of Last Measurement: In this case, an interesting scenario is investigated in which it is assumed that the RF link between the reader and the tag is temporarily disrupted due to excessive blockage of a tag or the presence of a strong interference. During the tag blockade, no data is exchanged between the reader and the tag, however, when tag data is properly decoded after a brief period of submersion, normal exchange of the data is reestablished between the tag and reader station. We call this phenomenon of temporary RF link loss as *submarining* and analyze its effect on the position estimation. During the submarining period, the last measured value of each sensed quantity, in the first set of experiments, will be repeated until the tag resurfaces and the new data is received. During the analysis, the effect of submarining was investigated by intentionally replacing a 360 ms length of data (50 data packets) with the last

measured value between 0.39–0.75 s, which is almost one-fourth of the total motion time.

- Case 3–Linear Interpolation based estimation: This is an extension of the previous case of submarining where instead of repeating the last measured value of each sensed quantity, the estimation is carried using linear interpolation until the new data is received after the RF link is reestablished. This was done to investigate which approach yields the best results when faced with submarining, i.e. repetition of last measured value as in previous case or linear interpolation. The duration and time interval for linear interpolation based estimation is identical to the previous case.

  The linear estimation approach is simple in which the gain matrix $\mathbf{L}$ is assumed to be zero for the duration of link loss, resulting the product $\mathbf{L}(\mathbf{h}(\hat{\mathbf{x}}) - \mathbf{h}(\mathbf{x}))$ to be zero in (29), reducing the estimator equation to linear form as

$$\dot{\hat{\mathbf{x}}} = \mathbf{A}\hat{\mathbf{x}} \tag{52}$$

  A benefit of this simplification is that the algorithm does not need to linearly interpolate the measured sensor quantities $\mathbf{y}$, as it is not required in the estimation thereby simplifying the process. Also, all the eigenvalues of the $\mathbf{A}$ matrix are zero, implying that in general the estimator will not explode and will stay in equilibrium.

  Although in this work, post-processing was done on the data to estimate the states, the entire HIMR modelling is generic and should work both in the real time and offline. The first three cases particularly address the real time implementation of the HIMR scheme.

- Case 4–Linear Interpolation for Offline Reconstruction: In this approach, it is assumed that the measured data is recorded on the readers and reused in

an offline scenario to analyze and reconstruct the track of the tagged object. Hence, the measured data is linearly interpolated between the two end points of the link breakage, i.e. the last values before the link loss and the first values after the link is reestablished.

- Case 5–Inertial data replay: In this case it is assumed that the tag has enough memory to store on board inertial sensor data during the submarining period. The inertial sensor data is wirelessly replayed and backscattered by the tag when its connection is reestablished with the reader. However, the RF data such as the received signal strength and the phase of received packet is still lost during the submarining period for this segment of the data. In our analysis, measurements based on the RF link such as approximated distance and radial velocities will repeat the last measured value of the quantities until the link is reestablished. However, instead of repetition, a linear interpolation approach could also be applied in future investigations. This investigation is also useful for offline reconstruction of the estimated position.

- Case 6–Packet rate reduction: The 9-DOF RF tag used for the 2D experiment backscatters 141 packets per sec. This case probes the effect of reduction in the number of available data samples on the 2D-HIMR-based positional estimation. For this purpose, the available data was reused by choosing every other packet, thereby emulating the case of 70 packets per second, which is half of the actual packet rate.

- Case 7–Two readers case: This case investigated the performance of the 2D-HIMR estimator by using the data from two readers instead of all three readers. This scrutiny was based on the fact that the system is observable using two RFID systems as was analyzed in the observability analysis. The observable system means that the states of the dynamic system can be recovered from the

measured sensory data. Therefore, it was necessary to investigate this fact.

The measured quantities and estimated position results for each case are discussed in the following sections.

4.3 Case 1: All measurements

This section discusses the results when all of the measured data is available for estimation, i.e. no data is missing or lost during the measurements due to absence of an RF link. First, the measured quantities are presented followed by position estimation results by using the measured quantities. The tag is installed on a boom mounted on top of a motor shaft which rotates the tag in the horizontal plane. During the motion the tag's on-board single chip-based inertial sensors, i.e. the accelerometer, the gyroscope, and the compass would measure the linear acceleration, angular velocity, and orientation of the tag, respectively. The data is continuously fetched by the microcontroller, packetized, and backscattered to the readers by toggling the RF switch. The readers extract two types of information from the received signal, the received signal strength to approximate the radial distance of the tag from the reader, and the received signal phase to approximate the the radial velocity, and then decode the received packet to extract the inertial information data.

During the rotation the radial distance of the tag varies with respect to each pylon. The radial distance decreases as the tag moves towards a pylon and it increases as the tag moves away from the pylon. This is depicted in Figure 26, which shows the approximated measured distance based on the received signal strength. The blue curve shows the radial distance r_1 from the first reader, the red curve shows the radial distance r_2 from the second reader, and the black curve shows the radial distance r_3 from the third reader. All the curves are noisy as the received signal fluctuates due to noise and multipath.

Figures 27–29 depict the radial velocities $\dot{r}_1$, $\dot{r}_2$ and $\dot{r}_3$ of the tag respectively,

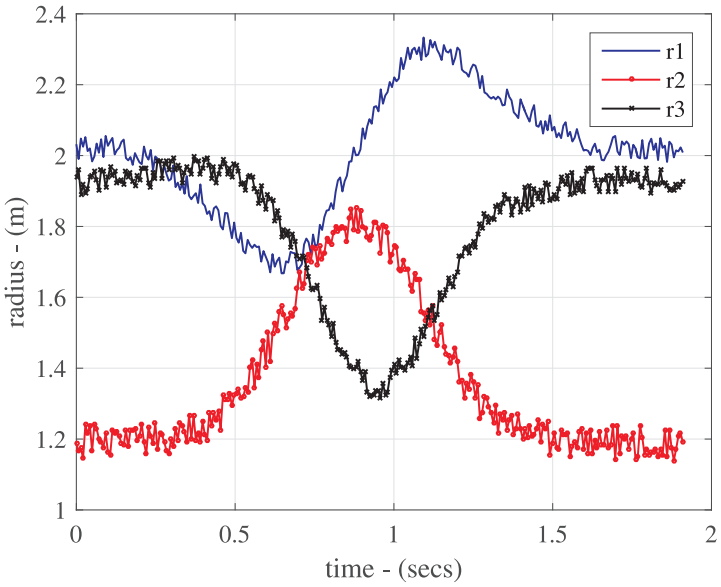

Figure 26: Radial distance of the tag with respect to each pylon approximated from the received signal strength.

approximated using packet-to-packet phase difference of the received signal. Positive velocity means the tag is moving away from the respective pylon whereas the negative velocity means it moves towards the respective pylon. This depends upon the direction of phase rotation on a constellation diagram. The phase rotates in the clockwise direction when the tagged object moves towards a pylon, resulting in a negative radial velocity, whereas the phase rotates in the counterclockwise direction as the tag moves away from the pylon resulting in a positive radial velocity [85].

Figure 30 shows the measured acceleration a_x and a_y along x^B and y^B-axes of the tag. The tag is mounted on the radial boom in such a way that during the counterclockwise rotation its positive y^B-axis is always tangent to its circular motion trajectory while the negative x^B-axis points towards the center of the circular motion trajectory. The tag experiences an acceleration and deceleration of $\pm$ 5 m/s^2 (0.5 g) along the y^B-axis whereas it experiences an acceleration of approximately -21 m/s^2 along its x^B-axis. The linear accelerations measured by the accelerometer are related

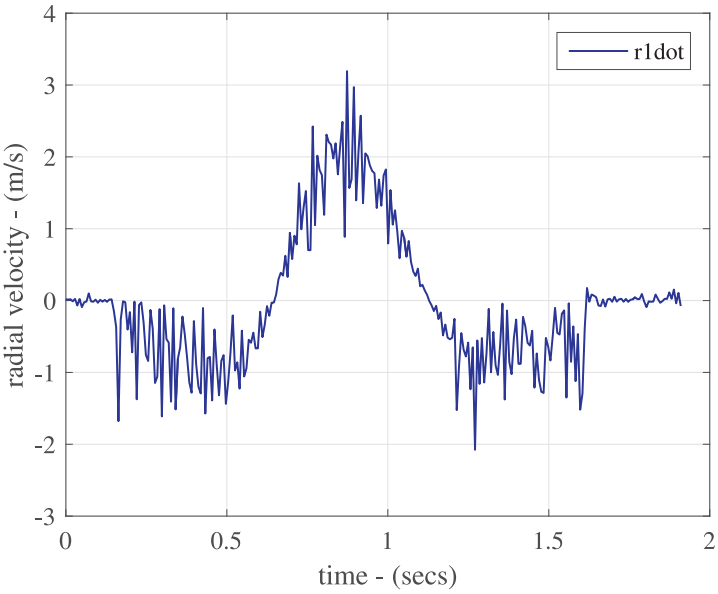

Figure 27: Radial velocity of the tag with respect to the first pylon. Radial velocity is approximated using packet-to-packet phase difference of the received signal.

to angular acceleration by the factor of radius of the circular trajectory.

Figure 31 shows the measured angular velocity ω_z of the tag around its z-axis measured using an on board gyroscope. The tag attains a maximum angular velocity of 8.5 rads per sec.

The last measured quantity is the orientation of the tag with respect to the fixed coordinate axis. The orientation of the tag is measured using the tag's on board compass. In our experiment the orientation of the tag is given by the direction of the tangential velocity vector which is along the tag's y^B-axis which is at angle of 180 degrees or π rads at the start of the motion as illustrated in Figure 22. The measured orientation angle is presented in Figure 32.

4.4 2D HIMR - Implementation

This section describes the steps taken to implement the two dimensional HIMR scheme. The estimation algorithm (29)–(30) has been derived using a continuous-time

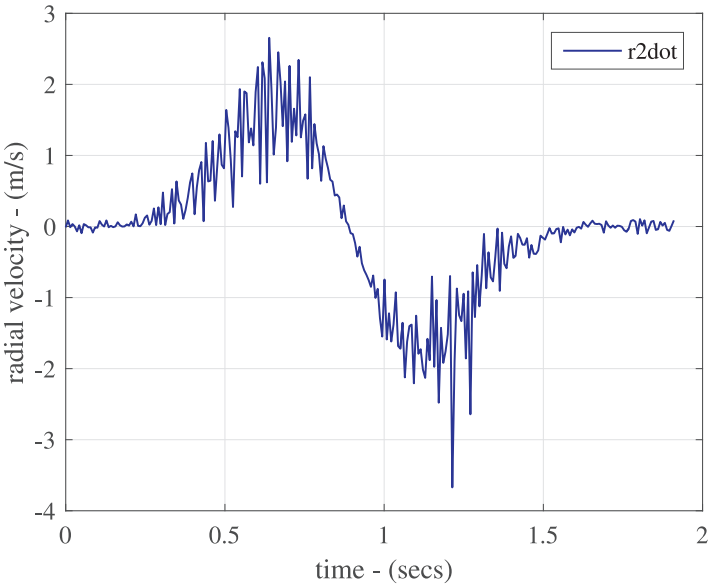

Figure 28: Radial velocity of the tag with respect to the second pylon.

model of the system, but its implementation requires a discrete-time formulation. To this end, the state equation of the estimator is transcribed from a differential equation to a difference equation. There are many methods for doing this, but in the this work the simplest method, known as the forward Euler method, has been used. The result of this procedure is

$$\hat{\mathbf{x}}[\mathbf{k}+\mathbf{1}] = \hat{\mathbf{x}}[\mathbf{k}] + T\left(\mathbf{A}\hat{\mathbf{x}}[\mathbf{k}] + \mathbf{L}\left(\mathbf{y}[\mathbf{k}] - \hat{\mathbf{y}}[\mathbf{k}]\right)\right) \tag{53}$$

$$\hat{\mathbf{y}}[\mathbf{k}] = \mathbf{h}(\hat{\mathbf{x}}[\mathbf{k}]) \tag{54}$$

where T is the fixed time increment between difference equation updates and k is the iteration index. For each increment of k, new measurements $\mathbf{y}$ arrive and new estimates $\hat{\mathbf{x}}$ are computed. Although matrices $\mathbf{A}$ and $\mathbf{L}$ are unchanged by this transcription procedure, their influence on estimator updates is scaled by T.

4.4.1 Choice of the C matrix

In this work, a linear approximation has been used to estimate the states of the system by using a fixed gain matrix $\mathbf{L}$. For calculating the gain matrix, we need the

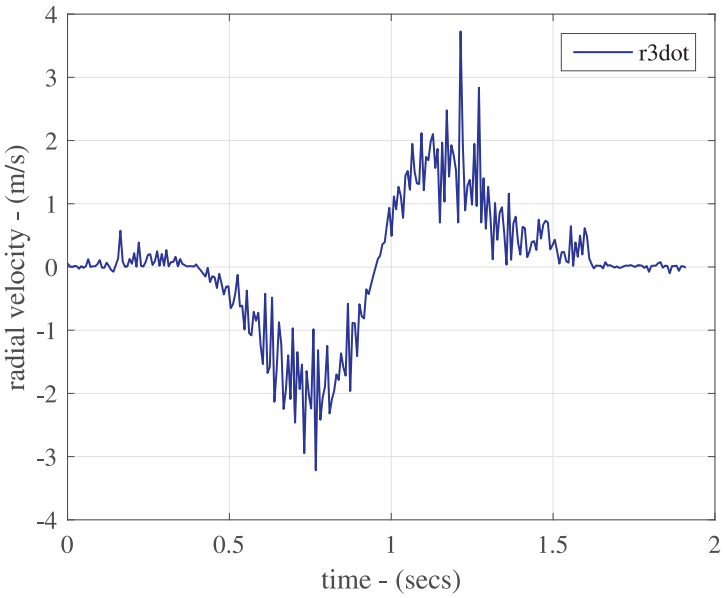

Figure 29: Radial velocity of the tag with respect to the third pylon.

two coefficient matrices **A** and **C** and the covariance matrices **W** and **V**. To this end, we calculated a **C** matrix by choosing a set of coordinates close to the motor coordinates and choosing reasonable motion parameters. To calculate **C** matrix we need carefully picked position coordinates of the tag, position coordinates of the three pylons, $\dot{x}$, $\dot{y}$, $\ddot{x}$, $\ddot{y}$, and the initial orientation of the tag. For our analysis purpose we chose the parameters listed in Table 8.

The resultant **C** matrix using its elements definition from appendix B is given below:

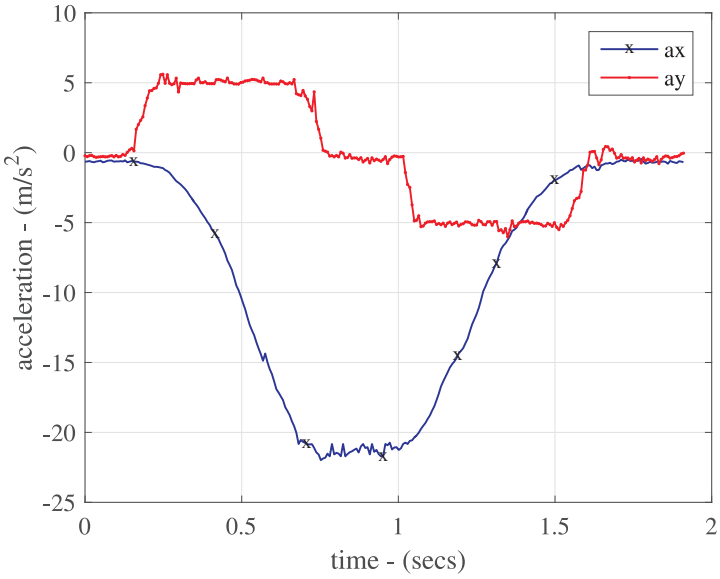

Figure 30: Measured linear acceleration of the tag during the circular motion. Acceleration a_x is along the negative x^B-axis of the tag pointing towards the circular trajectory's center while acceleration a_y is along the y^B-axis of the tag which is tangential at every point during the tag's rotation.

$$\mathbf{C} = \begin{bmatrix} 0.9936 & 0 & 0 & 0.1129 & 0 & 0 & 0 & 0 & 0 \\ 0 & 0.9936 & 0 & 0 & 0.1129 & 0 & 0 & 0 & 0 \\ 0.0767 & 0 & 0 & -0.9971 & 0 & 0 & 0 & 0 & 0 \\ 0 & 0.0767 & 0 & 0 & -0.9971 & 0 & 0 & 0 & 0 \\ -0.3194 & 0 & 0 & 0.9476 & 0 & 0 & 0 & 0 & 0 \\ 0 & -0.3194 & 0 & 0 & 0.9476 & 0 & 0 & 0 & 0 \\ 0 & 0 & -1 & 0 & 0 & 0 & 0 & 0 & 0 \\ 0 & 0 & 0 & 0 & 0 & -1 & 0 & 0 & 0 \\ 0 & 0 & 0 & 0 & 0 & 0 & 1 & 0 & 0 \\ 0 & 0 & 0 & 0 & 0 & 0 & 0 & 1 & 0 \end{bmatrix} \tag{55}$$

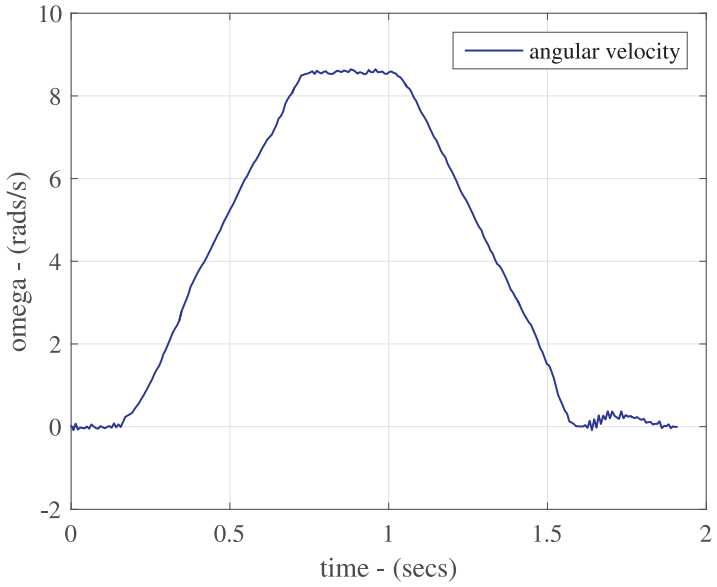

Figure 31: Measured angular velocity of the tag around tag's z-axis using on board gyroscope.

4.4.2 Choice of Tuning Matrices

The next step in the calculation of the gain matrix is to carefully choose the tuning matrices $\mathbf{W}$ and $\mathbf{V}$. The role of tuning matrices is to converge the estimator close to actual states, and reduce the error between the estimated and the actual state. To start with, both the tuning matrices were chosen to be an identity matrix. We only need to tune one matrix to achieve convergence of the estimated state to the actual state. For this purpose we tuned the $\mathbf{W}$ matrix by changing the numbers along the diagonal. Choosing an excessively high number for all entries may excite oscillations and result in large errors. One such case is discussed here, in which the identity matrix $\mathbf{W}$ when multiplied by a factor of 965, generated the oscillations in the estimated x and y coordinates resulting in undesirable errors. This is shown in Figures 33 and 34 where the magenta is the actual position of the tag while the blue is the estimated position. Throughout the discussion of the 2D-HIMR-based estimation results, the magenta curve with cross markers will represent the actual

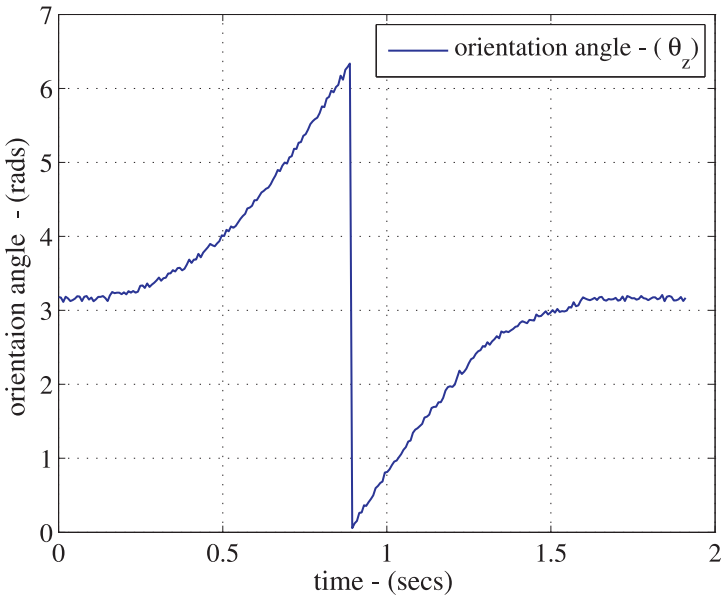

Figure 32: Tag orientation angle measured using compass.

state of the tag while the blue, black, or red curves will represent the estimated state. To start the estimation, the estimator was given an initial conditions of the tag's actual coordinates (2, 1.8048) m, its orientation of π rads, and zero velocity (implies the tag is at rest). Later in the discussion we will also analyze the impact of different initial conditions on the estimator. In Figures 33 and 34, although the estimator performed much better on the y coordinates than the x coordinates, however, we can observe the undesirable oscillations on both the estimated states. The matrices **W** and **L** for the oscillations case are given in section D.1 of appendix D and the eigenvalue analysis is given in section D.3 of appendix D. It can be observed from Figure 82 that for the oscillations case that the real part of eigenvalues becomes positive between 0.41 - 0.78 s. Considering that the eigenvalue analysis was carried out using the programmed reference trajectory of the motor and that there is a slight delay between the programmed vs the actual motion undertaken by the motor, therefore, the oscillations also occurred with a slight delay due to positive values real part of the eigenvalues.

Table 8: Parameters to calculate the matrix **C**. A pylon, in these experiments, is a transmitter and receiver reader antenna and the corresponding reader hardware that connects them.

Parameter	Value	Units	Remarks
(x,y)	(2.1, 1.75)	m	
(x_1,y_1)	(-0.1, 1.5)	m	pylon # 1
(x_2,y_2)	(2, 3.05)	m	pylon # 2
(x_3,y_3)	(2.7, -0.03)	m	pylon # 3
$\dot{x}$	0	m/s	
$\dot{y}$	0	m/s	
$\ddot{x}$	0	m/s^2	
$\ddot{y}$	0	m/s^2	
ψ	π	rads	

To resolve this, the implementation of the 1D-HIMR scheme was revisited [48], where it was learnt that the **W**-matrix does not have equal weighting across the diagonal; instead the position's state has double the weighting than the velocity and acceleration state. Similarly in the 2D case, when the weighting of the x and y position states in the tuning matrix was changed to a factor of 4 as compared to their velocities and accelerations respectively, no oscillations were observed while much better estimation was achieved as presented in Figures 35–37. This makes sense as during the process of formulating the **C** matrix we assumed zero velocities and accelerations, therefore giving these states higher weight in the tuning matrix may result in undesirable results. The gain and tuning matrices along with the eigenvalues for this case are given in section D.2 and section D.3, respectively, of appendix D which will used for Cases 1 – 6.

Figure 35 shows the x-coordinate estimation results with the modified tuning matrix. It can be observed that as the time progresses the x-estimated position curve (blue curve) converges to the x-actual position curve (magenta curve with cross markers). Figure 36 shows the y-coordinate estimation results. Unlike the x-coordinates, the estimator performed much better in estimating the y-coordinates as the estimated curve quickly converged to the actual y-position curve. Figure 37

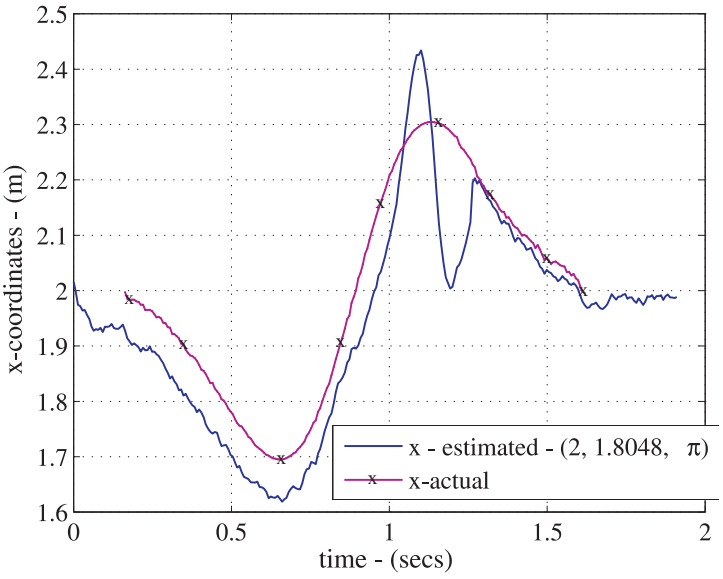

Figure 33: Estimated x-coordinates, oscillations observed in the estimated coordinates because of excessively high values used in $\mathbf{W}$. The initial conditions for the estimator are given in the legend.

presents the results of orientation angle estimation, where it can be observed that the estimator quickly converges to the actual orientation. The orientation of the tag has direct impact on the position estimation of the tag. Minor orientation error in the beginning, approximately between 0.1–0.7 secs, may have affected the relatively slow convergence of x coordinates as compared to y-coordinates.

4.4.3 Initial Conditions

This section discusses the performance of the estimator under two additional initial conditions. In practical implementation, the HIMR-estimator may be given any random initial position and orientation of the tag which may not match the exact location and orientation of the tag or tagged object. Therefore, it is necessary to test the estimator for other initial conditions as well. The initial conditions with the most impact are the position coordinates and the orientation of the tag. Therefore, only these were varied during the analysis. Three sets of initial conditions used for the

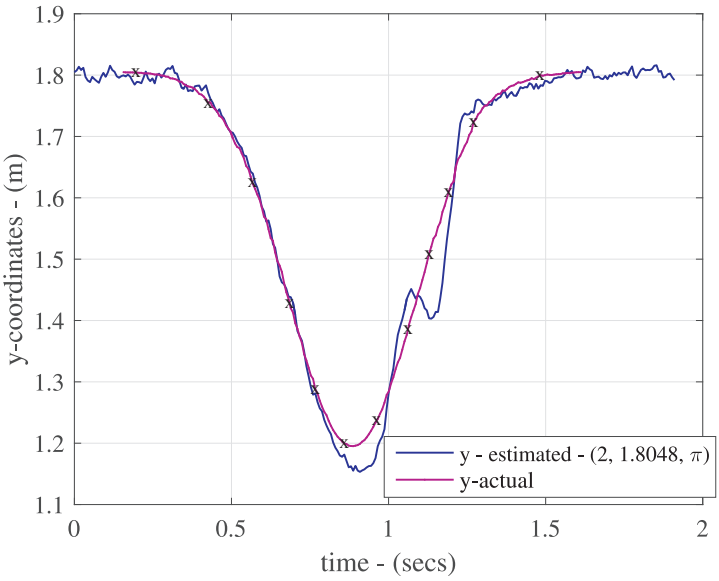

Figure 34: Estimated y-coordinates, oscillations observed in the estimated coordinates because of excessively high values used in $\mathbf{W}$.

analysis are given in Table 9.

The estimated results for the initial conditions given in Table 9 are presented in Figures 38–40. The estimated x-position is given in Figure 38 where the solid curve represents the estimated results for the first set of initial conditions, the dashed curve represents the second, and the dashed-dot curve represents the third. It can be observed that curves for all three conditions converge to one another within 0.2 s

Table 9: List of initial conditions (IC) used for testing the 2D-HIMR.

Parameter	IC # 1	IC # 2	IC # 3	Units
(x,y)	(2, 1.8048)	(1, 1)	(2.5, 2.3)	m
$\dot{x}$	0	0	0	m/s
$\dot{y}$	0	0	0	m/s
$\ddot{x}$	0	0	0	m/s^2
$\ddot{y}$	0	0	0	m/s^2
ψ	π	$\frac{\pi}{2}$	$\frac{3\pi}{2}$	rads
$\dot{\psi}$	0	0	0	rads/s
$\ddot{\psi}$	0	0	0	rads/s^2

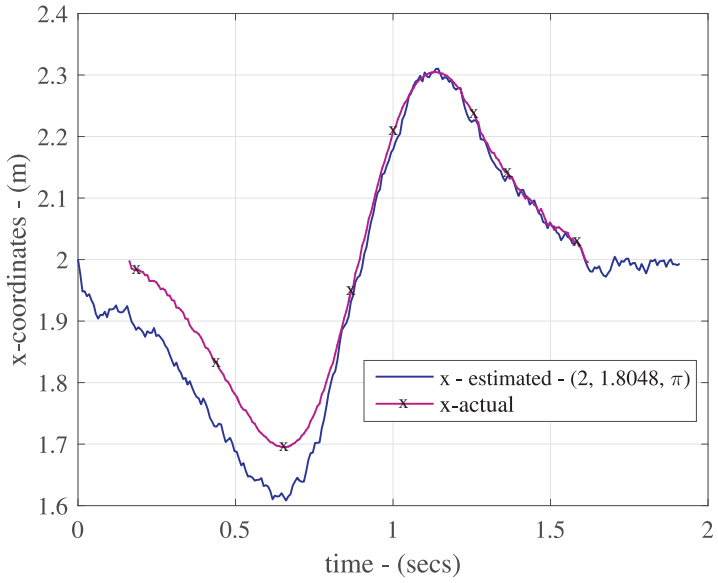

Figure 35: Case 1: Estimated x-coordinates. The estimator's initial conditions are given in the graph's legend. The estimator converged to the actual position after almost 0.8 s.

and together these converge to actual x position within 0.8 s. This depicts that the estimator performs equally well for all initial conditions.

Figure 39 presents the estimated y-position for the three initial conditions which converge within 0.2 s and follow the actual position curve. Figure 40 presents the estimated orientation angle. It can be observed that the convergence time for the estimated curves is 0.35 s, which is greater than the positional estimation curves. However, all estimated results closely follow the actual orientation curve. From here onwards, for all the other cases, we will present the combined results for all initial conditions, just like Figures 38–40.

4.4.4 Case 1: Error Analysis

Before proceeding further it is important to analyze the accuracy of the estimator by finding the error between the actual and the estimated states. Since we are more interested in the position coordinates, only the error in x and y coordinates have been

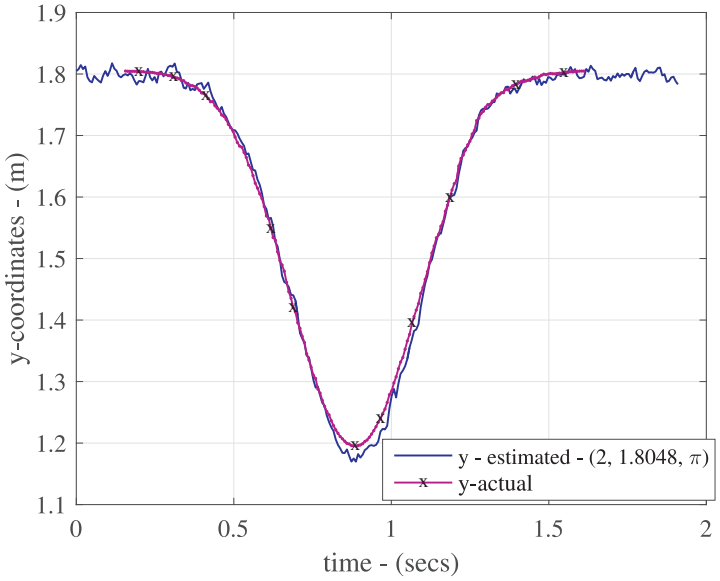

Figure 36: Case 1: Estimated y-coordinates. The estimator showed good convergence for the y-coordinates except slight divergence between 0.8–1.15 s possibly because the actual y curve started changing its slope.

presented here. Further, for the sake of clarity and comparison only the error for the first initial condition has been been presented throughout this work, since estimated curves for the all the initial conditions were close to one another. Figure 41 presents the x-position error. The error is initially 10 cm (0.1 m) but, as the time progresses, the error reduces to less than 2 cm. Similarly, Figure 42 presents the y-position error, which reduces to 1 cm near the end of the motion. It is observed that since the error reduces over time, if the system under observation runs for a longer duration, such as more than 5 s, it is expected that error will further reduce to less than 1 cm for the position coordinates. Finding a mean error may not be the best figure of merit since the error does not fluctuate around zero; rather the error continuously reduces as time advances.

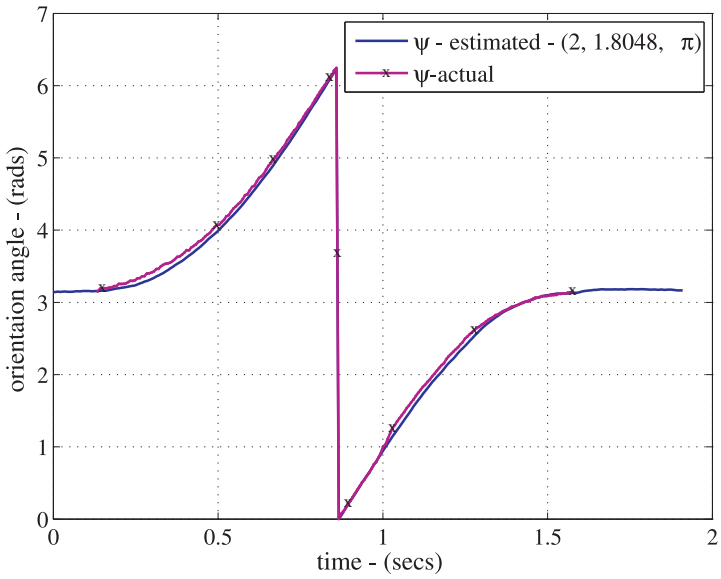

Figure 37: Case 1: Estimated orientation angle. Estimated and actual curves show close agreement.

4.5 Case 2: Tag Submarining - Repeating last measurement

Under an ideal scenario, it is expected that the RF link between tag and the readers is always active meaning that the data from the tag is backscattered at regular intervals. However, practically there can be a scenario under which the RF link is briefly lost or disrupted either due to tag occlusion or interference. This section discusses the performance of the proposed HIMR scheme under such scenarios. In the absence of RF link, the measured data from the tag is not available for the state estimation. This can be dealt by a number of approaches such as:

- By repeating the last measured value of each sensor during the link breakage time. This scenario is discussed in this section (section 4.5).
- By linearly interpolating between the last measured value before the link loss and the first measured value when the link is available. This scenario is discussed in section 4.6 and 4.7.

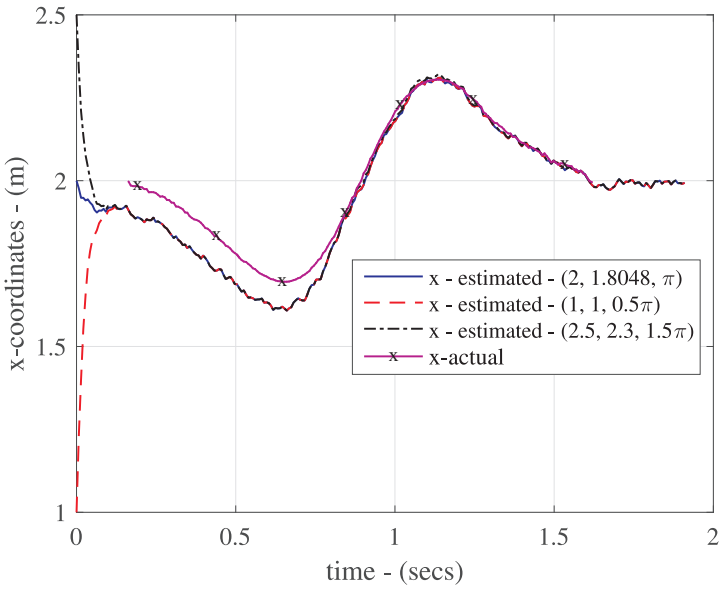

Figure 38: Case 1: Estimated x-position for three different initial conditions. The conditions are given in the figure's legend for reference. The estimator performs equally well for all initial conditions.

- By storing the tag's data in an on board memory and wirelessly replaying the inertial data when the the link is reestablished. This scenario is discussed in section 4.8.

To emulate the first case of tag submarining, a 360 ms length of measured data from each RF and inertial sensor to be used for estimation was intentionally replaced with the last measured value between 0.39–0.75 s, which is almost one fourth of the total motion time. Pictorially, the flawed data from each sensor with repeated last value is shown in Figures 83 – 89 in appendix E.

The estimated position coordinates and orientation results using flawed measured quantities are exhibited in Figures 43 – 45. The results are presented for all three initial conditions considered earlier for the estimator. It can be observed from Figure 43 that the estimated x-position curves converge to the actual position curve in almost 0.1 s after the link is reestablished. However, during the link blockage the estimates

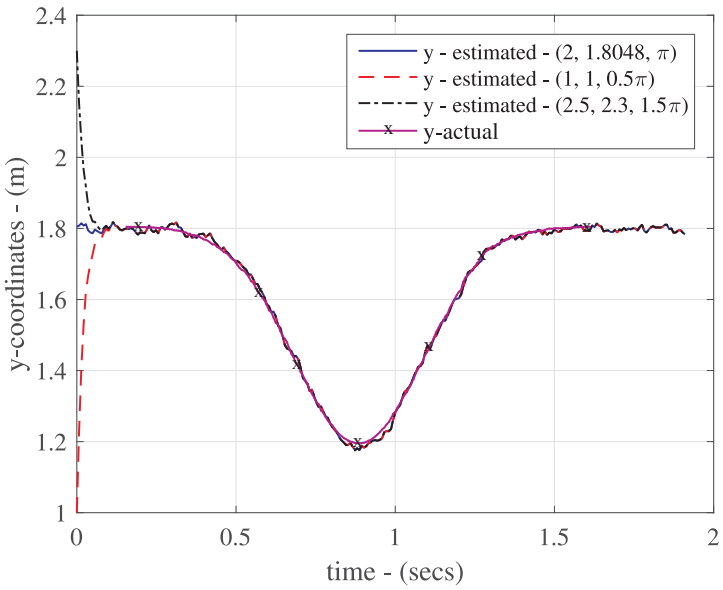

Figure 39: Case 1: Estimated y-position for three different initial conditions. The conditions are given in the figure's legend for reference. The estimator performs equally well for all initial conditions.

stayed constant as the same last state was repeated in each sensed quantity used for estimation. This is expected as repeating the values in the sensed quantities are equivalent to giving a new set of initial conditions during the estimation process and should not affect the estimation process much. Similar results are observed for the estimated y-position and the orientation angle which converged back to actual curves within reasonable time of within 0.2 s after the link is reestablished.

4.5.1 Case 2: Error Analysis

This section details the error analysis of the second case under investigation. The error is only computed for the first initial condition, as mentioned in the error analysis of the previous case. It can be observed from Figures 46 and 47 that the error increases especially for the y-position where it jumps up to 0.5 m during the link breakage but reduces quickly when the link is reestablished and finally decreases down to within 2 cm for the both the position coordinates. Moreover, the amount of error may also

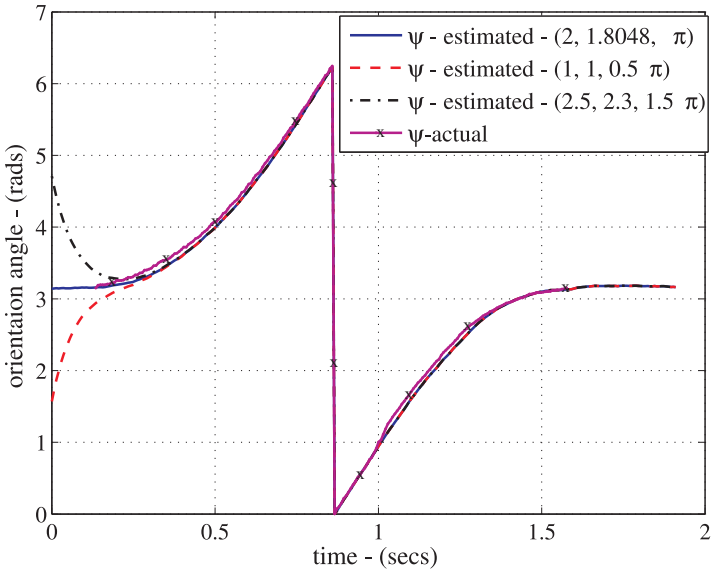

Figure 40: Case 1: Estimated orientation angle for all initial conditions. The convergence time for the estimated curves is 0.35 s, which is greater than the positional estimation curves.

correspond to timing and duration of the link loss.

4.6 Case 3: Tag Submarining - Linear Interpolation

This section continues the investigation of the second approach to mitigate the effects of the link loss. The second approach performs the linear estimation without interpolating the data in the duration of link breakage. The linear estimation was performed between 0.39 s and 0.75 s.

The estimated position and orientation results for this approach are exhibited in Figures 48 – 50. This approach offers modest improvements on the y-position estimation (Figure 49) whose maximum error is reduced to 0.3 m as compared to 0.5 m maximum error on the y-estimate in the previous case. The error on both x and y coordinates converges to within 2 cm over time.

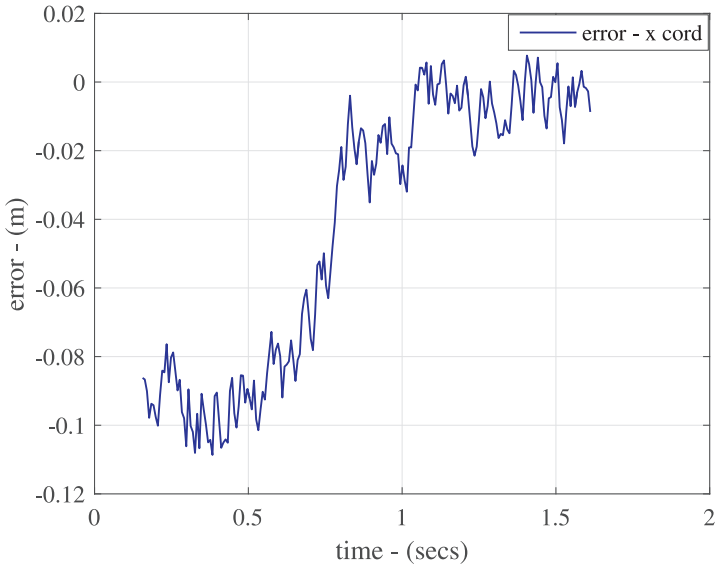

Figure 41: Case 1: Error in x-coordinates.

4.6.1 Case 3: Error Analysis

The graph of the computed positional error for the linear interpolation case is shown in Figures 51 and 52. The maximum error on the x-position is 16 cm which reduces to less than 2 cm over time whereas the maximum error on y-position is 0.3 m which also reduces to less than 2 cm as the motor comes to rest.

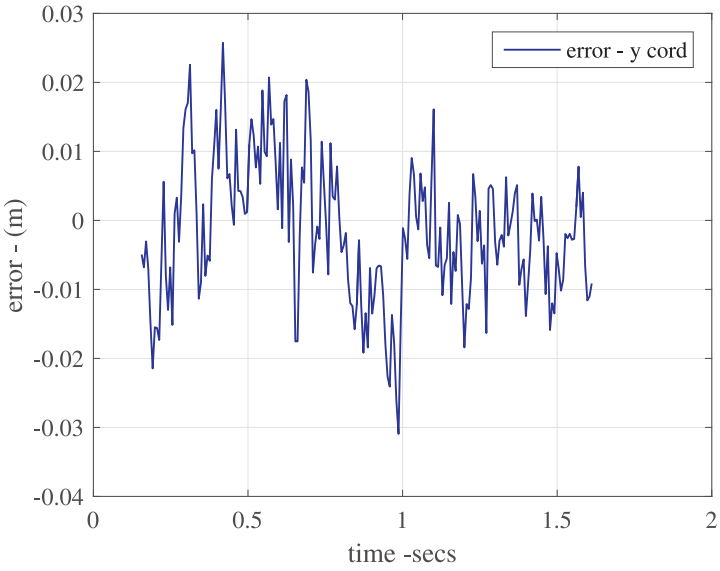

Figure 42: Case 1: Error in y-coordinates.

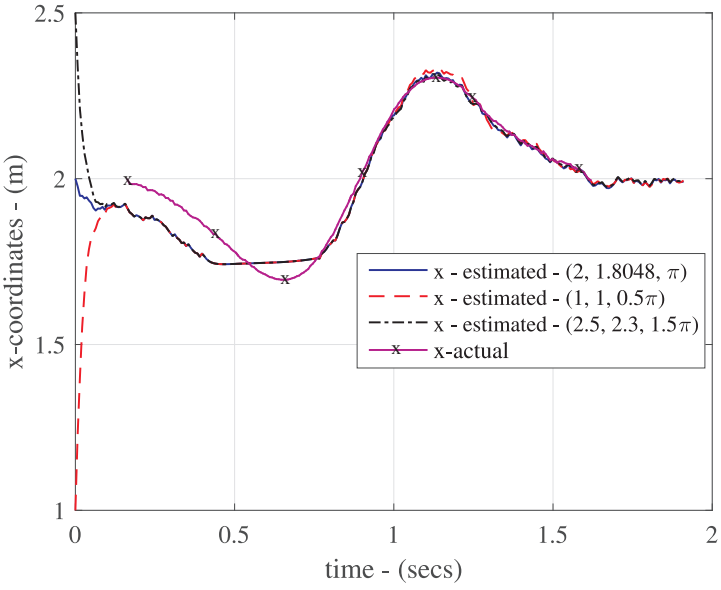

Figure 43: Case 2: Estimated x-position for all initial conditions using value repetition approach on the flawed sensed quantities.

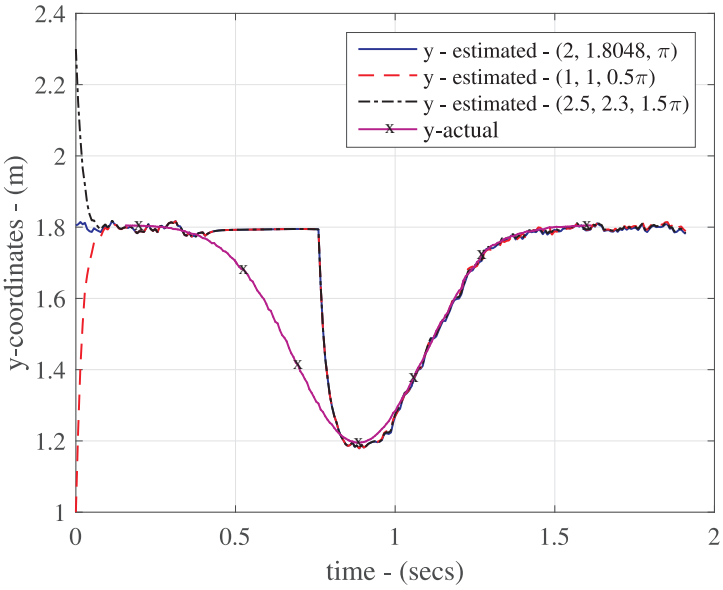

Figure 44: Case 2: Estimated y-position for all initial conditions using value repetition approach on the flawed sensed quantities.

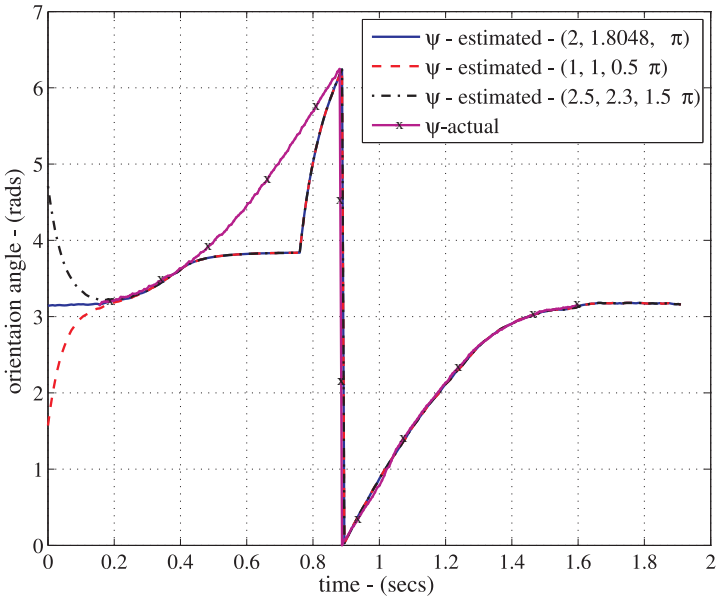

Figure 45: Case 2: Estimated orientation angles for all initial conditions using the value repetition approach on the flawed sensed quantities.

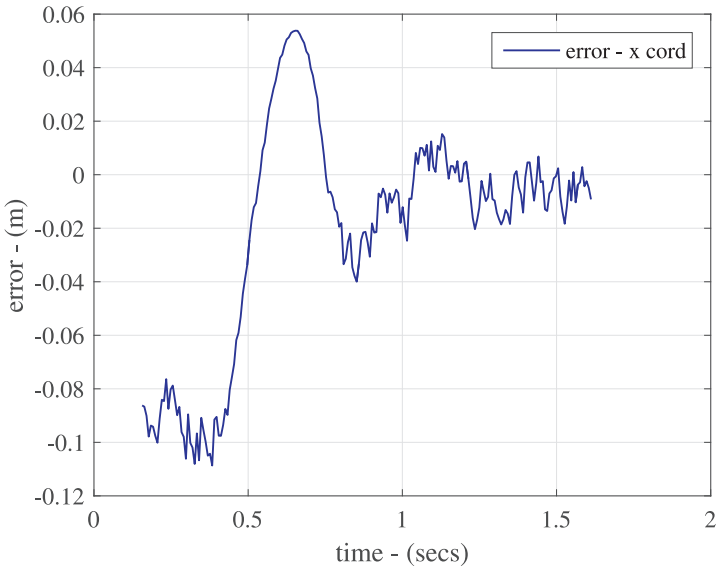

Figure 46: Case 2: Error in x-position due to the value repetition approach as explained above.

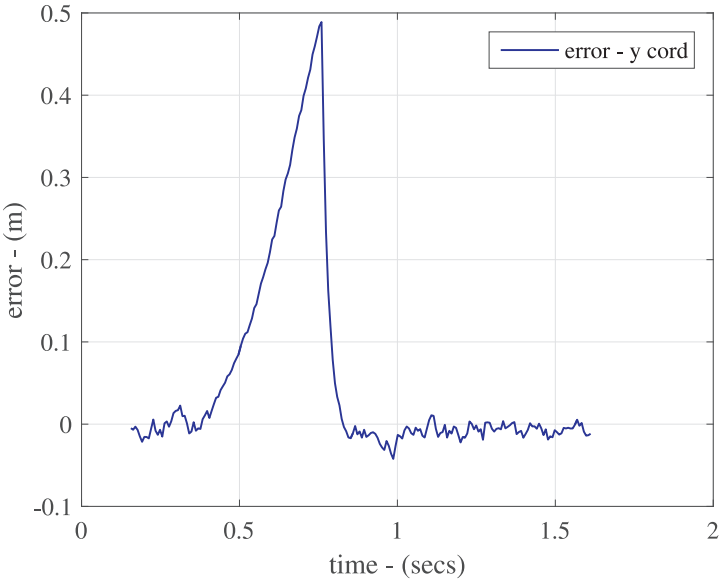

Figure 47: Case 2: Error in y-position due to the value repetition approach as explained above.

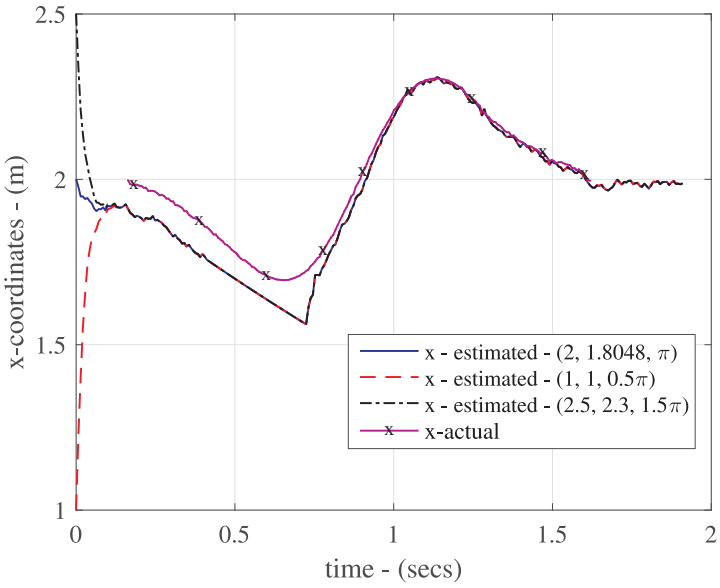

Figure 48: Case 3: Estimated x-position for all initial conditions using the linear interpolation approach.

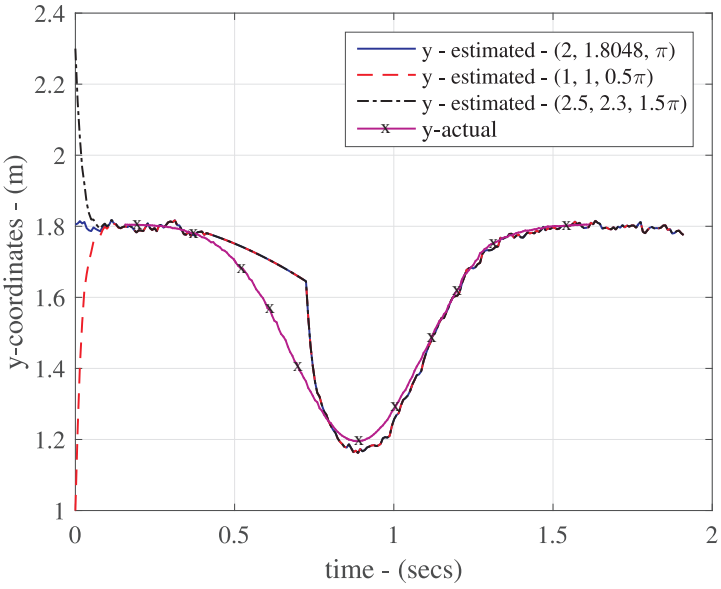

Figure 49: Case 3: Estimated y-position for all initial conditions using a linear interpolation approach.

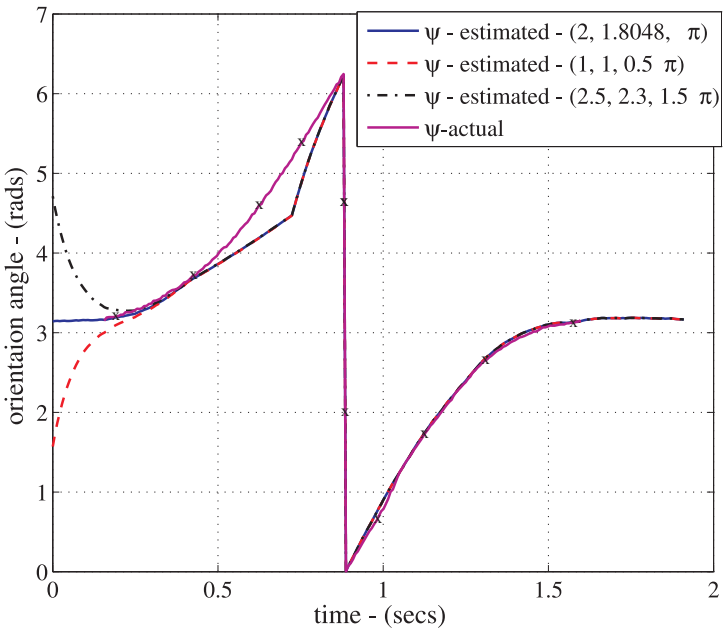

Figure 50: Case 3: Estimated orientation angles for all initial conditions using a linear interpolation approach.

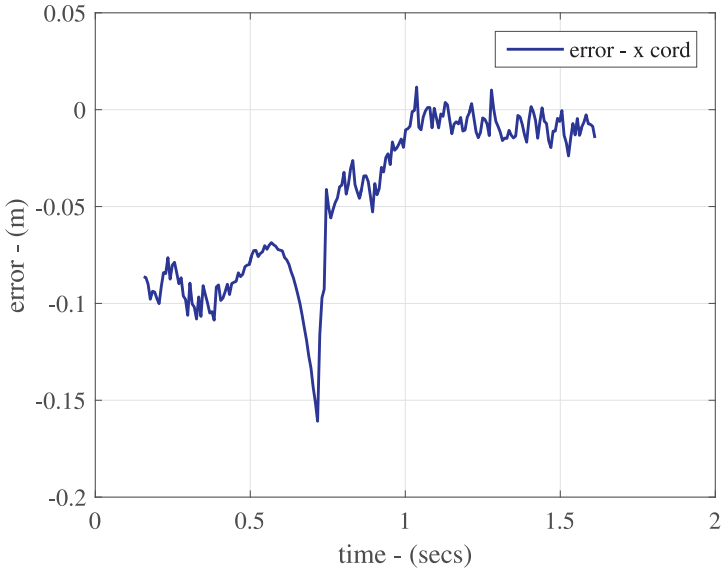

Figure 51: Case 3: Error in x-position using a linear interpolation approach.

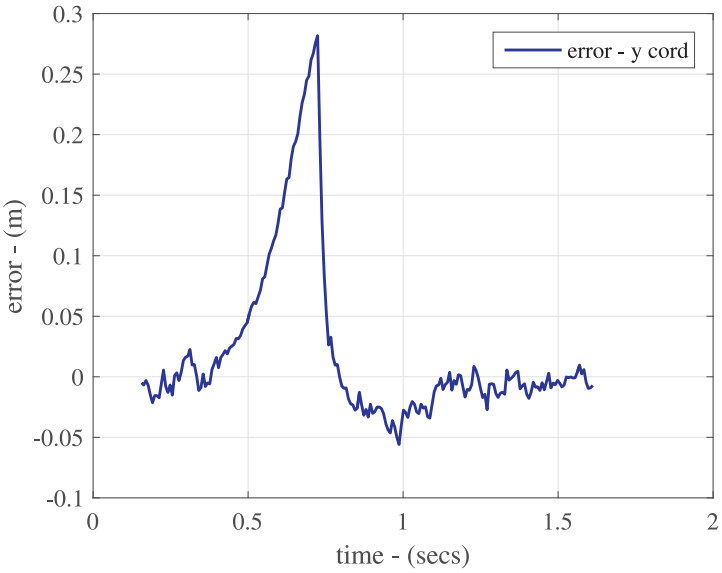

Figure 52: Case 3: Error in y-position using a linear interpolation approach.

4.7 Case 4: Tag Submarining - Linear Interpolation for offline reconstruction

This section analyzes an "offline" approach to reconstruct the tag's position by using the recorded measurement data. It linearly interpolates the data between two end points of the duration of a link breakage instead of repeating the last measured value of the sensed quantity. The linear interpolation was performed between 0.39 s and 0.75 s. Pictorially, the flawed data from each sensor with the linear interpolation approach is shown in Figures 90 – 96 in appendix F.

The estimated position and orientation results for this approach are exhibited in Figures 53 – 55. This approach offers improvement on both the positions and orientation estimation as compared to the previous cases, especially, on y-position estimation (Figure 54) whose curve now closely follows the actual y-position curve similar to Case # 1 where the RF link was always established. The estimated x-position also has visibly less error than the previous cases while the orientation angle estimation outperforms the previous case.

4.7.1 Case 4: Error Analysis

The graph of the computed positional error for the linear interpolation case is shown in Figures 56 and 57. The maximum error in the x-position is 10 cm which reduces to less than 2 cm over time whereas the maximum error in the y-position is 5 cm which also reduces to less than 2 cm as the motors comes to rest.

4.8 Case 5: Tag Submarining - Inertial Data Available

This section describes the results of the another approach in the event of link breakage between the tag and the reader. In this approach, it is assumed that the tag has enough memory to store on board inertial sensor data during the submarining time. The inertial sensor data is replayed and backscattered by the tag when its connection is reestablished with the reader. However, the RF data such as the received

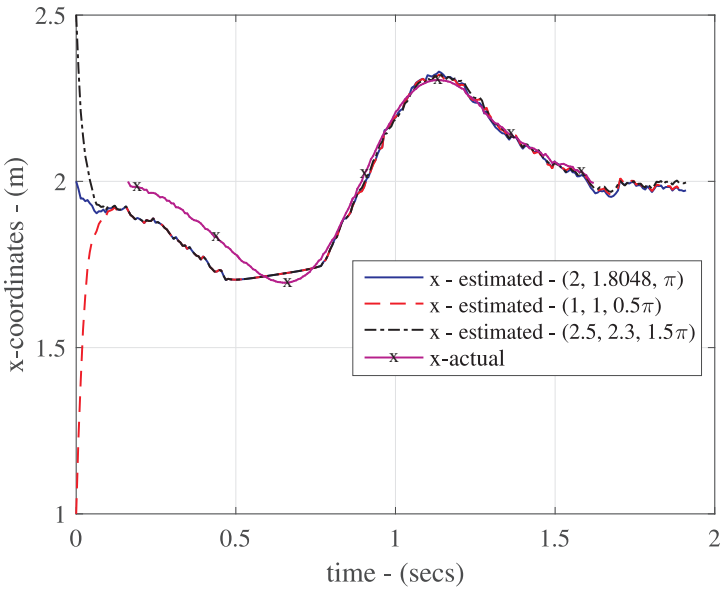

Figure 53: Case 4: Estimated x-position for all initial conditions using a linear interpolation approach on the flawed sensed quantities.

signal strength and the phase of received packet is still lost during the submarining time. In our analysis of this case, the last measurements based on the RF link such as the approximated distance and radial velocities before the link loss will be repeated until the link is reestablished.

The curves for the measured quantities are similar to the one given for Case 2 (radial distance and radial velocity curves) and Case 1 (inertial data curves). Large errors are observed in the position coordinates because of the approach that repeats the last measured value of RF-based sensed quantities. The error can be reduced by using a linear interpolation approach for the RF-based sensed data. It also emphasizes that inertial data alone cannot be used for fine scale position estimation, rather a fusion of both RF and inertial based sensing would yield better accuracy.

The estimated position and orientation results for this case are shown in Figures 58 – 60.

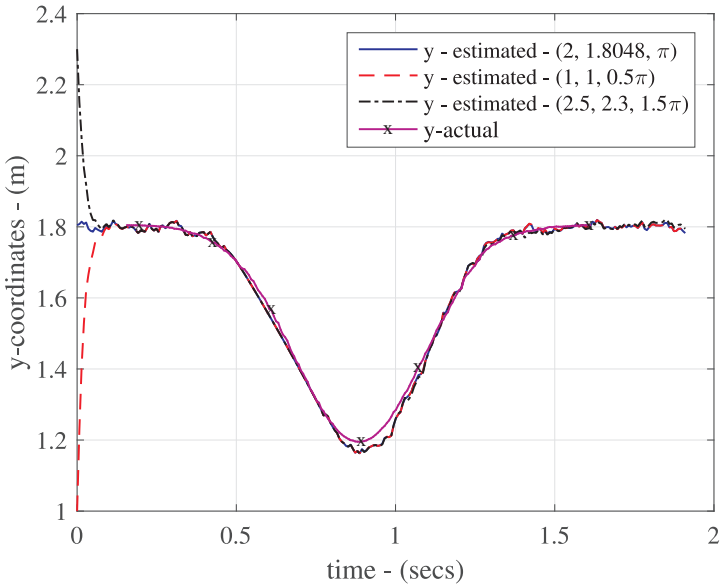

Figure 54: Case 4: Estimated y-position for all initial conditions using a linear interpolation approach on the flawed sensed quantities.

4.8.1 Case 5: Error Analysis

The error graphs of positional accuracy for this case are given in Figures 61 and 62. The error margins are similar to the Case 2 approach based on repeated last measured values. It emphasizes that RF-based sensing is crucial for accurate position sensing. The errors could be reduced using a linear interpolation approach.

4.9 Case 6: Packet rate reduction

This section demonstrates the effect of lower packet rates ($<$ 100 packets per sec) on the HIMR-based 2D position estimation. The 9DOF RF tag used for the 2D experiment backscatters 141 packets per sec. For the purpose of analysis, the available data was reused by choosing every other packet, thereby emulating the case of 70 packets per second which is half of the actual packet rate. The packet rate is determined by a number of factors such as the clocking rate of the tag's microcontroller, the time taken by thet microcontroller to access the inertial sensor's

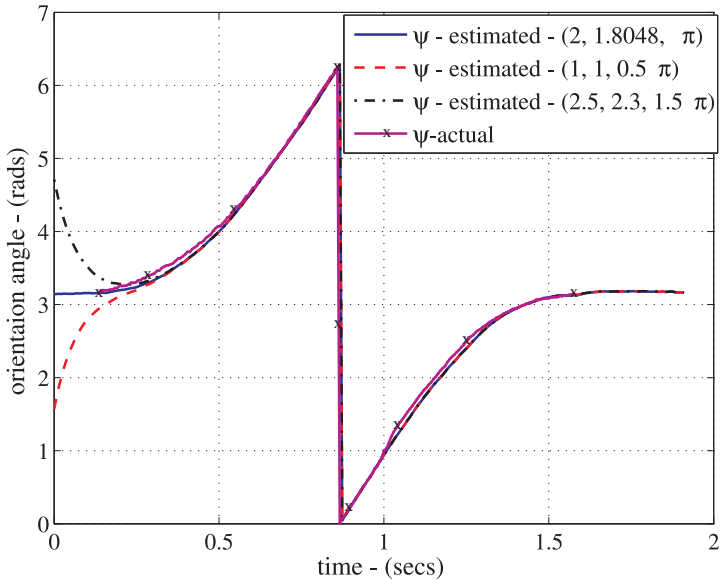

Figure 55: Case 4: Estimated orientation angles for all initial conditions using a linear interpolation approach on the flawed sensed quantities.

data, the arrangement of data to form packets and the time taken to backscatter a single packet.

The estimated position and orientation results for a 70 packets per sec data rate are given in Figures 63 – 65. The rate of convergence of the estimator depends upon two factors, the tuning matrices and the number of available data samples for a given system's states. For fixed tuning matrices, the higher the number of available samples for a given state means earlier convergence of the estimated to the actual state and vice versa. This can be observed from the x and y position estimates which converge to the actual state after almost 1.2 s as compared to all previous cases where x converges in about 0.8 s and y converged instantly.

4.9.1 Case 6: Error Analysis

The x and y positional error graphs for the packet reduction case are shown in Figures 66 and 67. The maximum error in the x-position goes up to 13 cm before reduction to within a 2 cm range. Whereas, the maximum error in the y-position goes

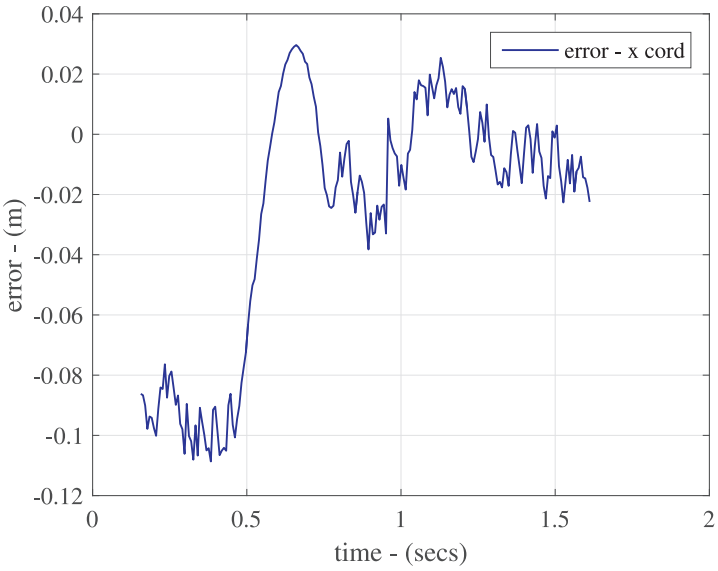

Figure 56: Case 4: Error in x-position using a linear interpolation approach.

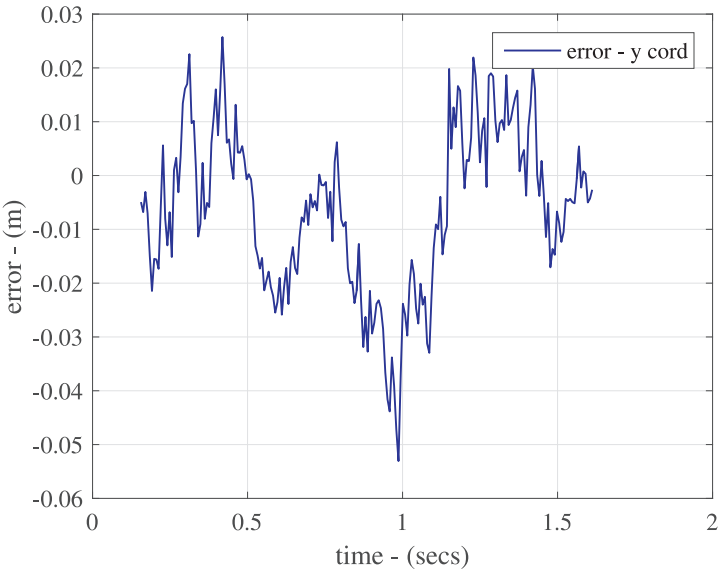

Figure 57: Case 4: Error in y-position using a linear interpolation approach.

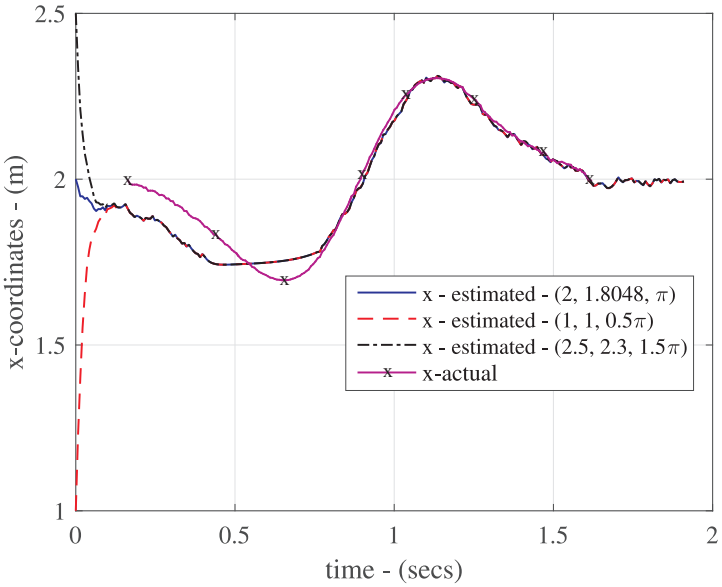

Figure 58: Case 5: Estimated x-position for all initial conditions where inertial data is available while RF-based data is not available.

up to 8 cm before reduction to within a 1 cm range. The error is large up to 1.2 s after which the estimated position converges to the actual position thereby reducing the error.

4.10 Comparison Cases 1–5

This section compares the results of the first five cases. We present the comparison of estimated x and y-positions and their respective errors for all four cases under the first initial condition of the estimator in Figures 68 – 71. Case 1 where all the measured quantities were used for estimation, results in the lowest error whereas the linear interpolation approach gives the best estimation among the link breakage cases. In the legend of all comparison figures, AM means all measurements used for estimation without link loss, 360ms means the duration for which the last measured measurements were repeated in each sensed quantity, LI means that the linear interpolation approach was used and IDP means that the approach where inertial data is available for estimation while RF-based quantities were not used.

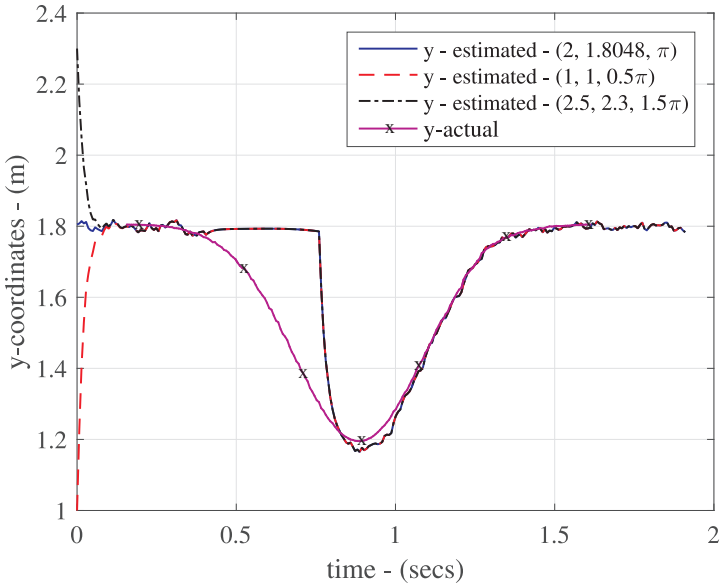

Figure 59: Case 5: Estimated y-position for all initial conditions where inertial data is available while RF-based data is not available.

4.11 Case 7: Estimation using Two Readers

The observability analysis in section 3.5.5 showed that the 2D-HIMR dynamical system is observable by using two readers implying that the states can be estimated using the measured data from two readers. This section presents the estimation results using the pair of readers 1 and 2. For the analysis purpose, we used the reduced order **C**-matrix from (55) by deleting its rows 5 and 6 which are related to the third reader. This reduced the order of the modified **C**-matrix to 8×9 (from 10×9), which required modifying the tuning matrices, and correspondingly computing the new gain matrix. The modified tuning matrices along with the new gain matrix are given in appendix D under the case 7 section.

The estimated position and orientation results for the current case are given in Figures 72 – 74. It can be observed that the estimated x and y-position curves converged to actual position curves in almost 1.1 s. Unlike Cases 1 – 5, the estimated y- position also took longer to converge to the actual position. These observations

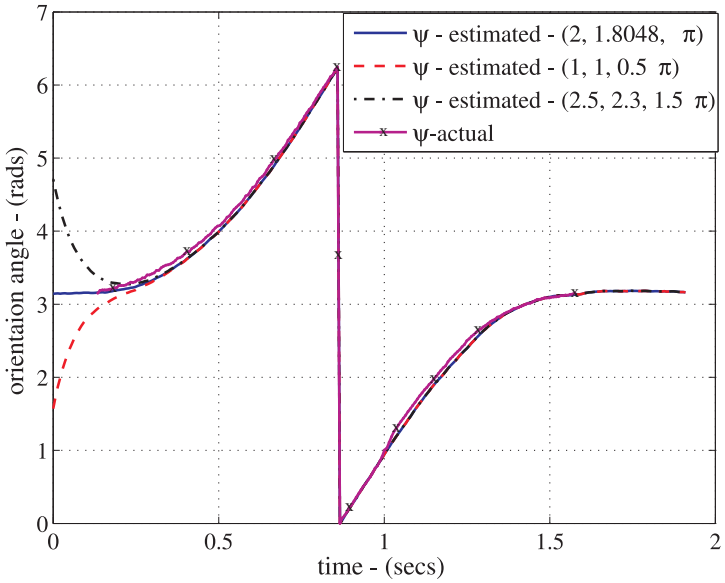

Figure 60: Case 5: Estimated orientation angle for all initial conditions where inertial data is available while RF-based data is not available.

lead to conclusion that although the dynamical system states can be estimated using two readers, using all three readers leads to early convergence of estimated to actual states and reduces overall error by providing an extra set of measurements.

4.11.1 Case 7: Error Analysis

The positional error curves for this case are presented in Figures 75 and 76. The maximum error in the x-position goes up to 13.5 cm before reducing down to within 2 cm after almost 1.1 s. Similarly, the maximum error in the y-position is 10 cm before reducing down to within 2 cm after 1.1 s.

4.12 Conclusion

This chapter presented the theory and experimental results of the 2D-HIMR scheme based tag L&T, and discussed various cases that could arise during the implementation of the technique. A 2 cm positional accuracy on both the x and y coordinates was achieved for all cases using the HIMR algorithm without the use of

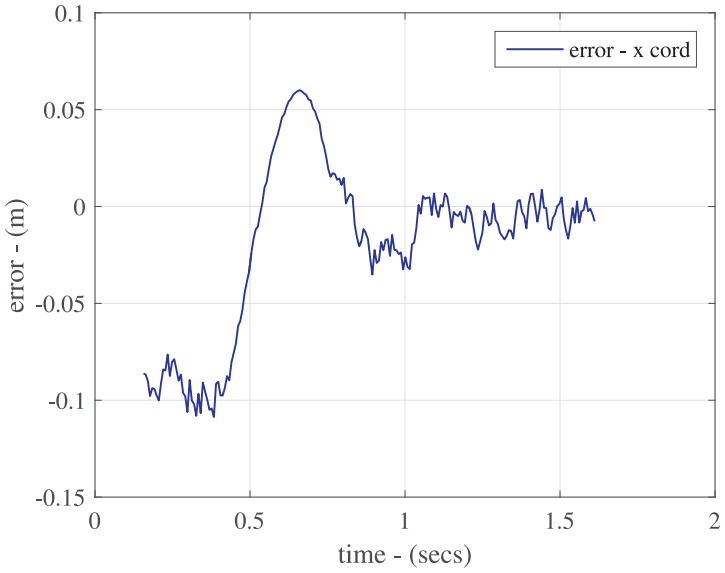

Figure 61: Case 5: Error in x-position.

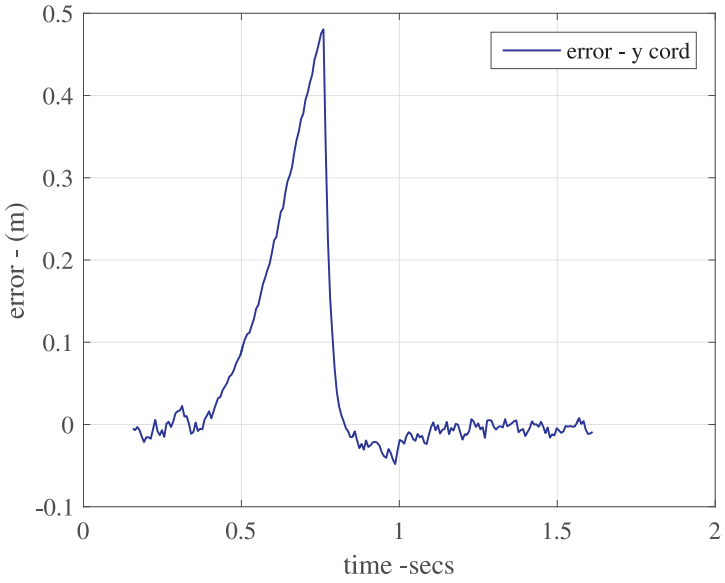

Figure 62: Case 5: Error in y-position.

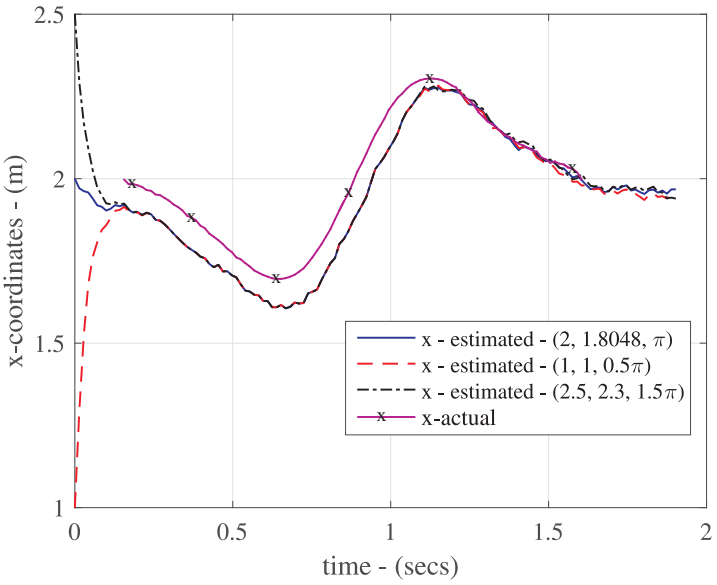

Figure 63: Case 6: Estimated x-position for a lower packet rate scenario.

any reference tags or any other pre-stored, pre-sorted, or pre-measured information. The HIMR scheme provided L&T accuracy based on fusion of RF- and inertial-based measurement data including radial distance approximated through received signal strength, radial velocity approximated through received signal phase, acceleration, angular velocity and compass measurements.

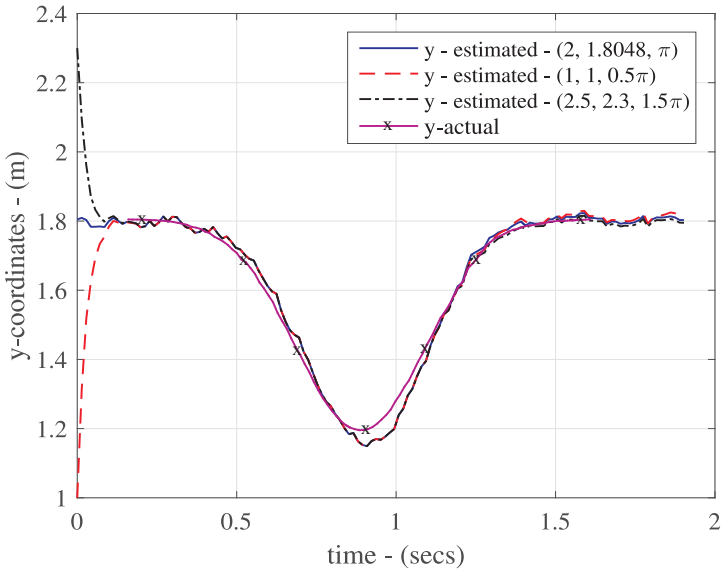

Figure 64: Case 6: Estimated y-position for a lower packet rate scenario.

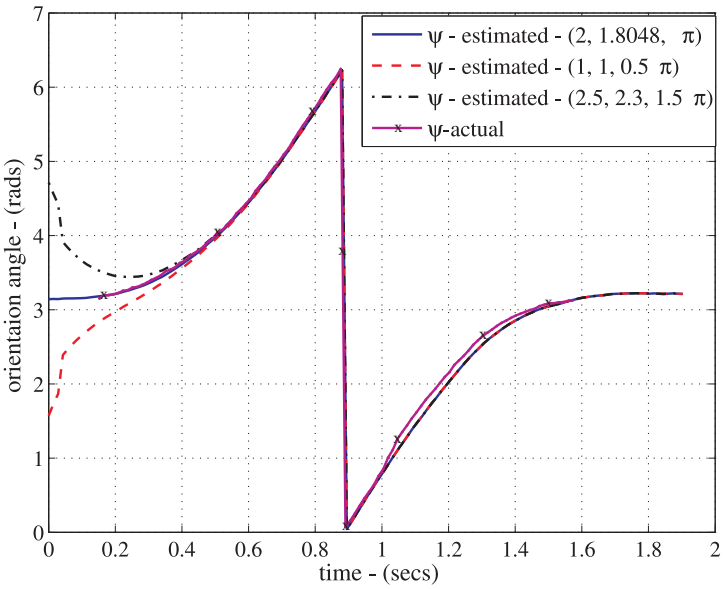

Figure 65: Case 6: Estimated orientation angle for a lower packet rate scenario.

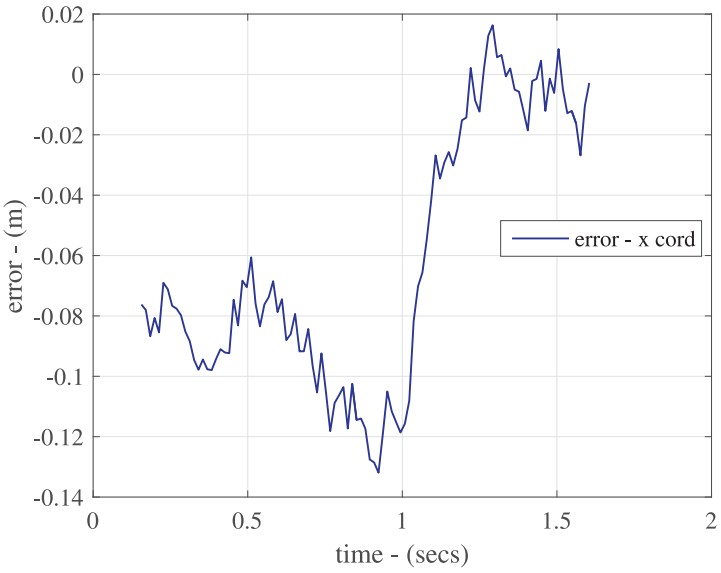

Figure 66: Case 6: Error in x-position

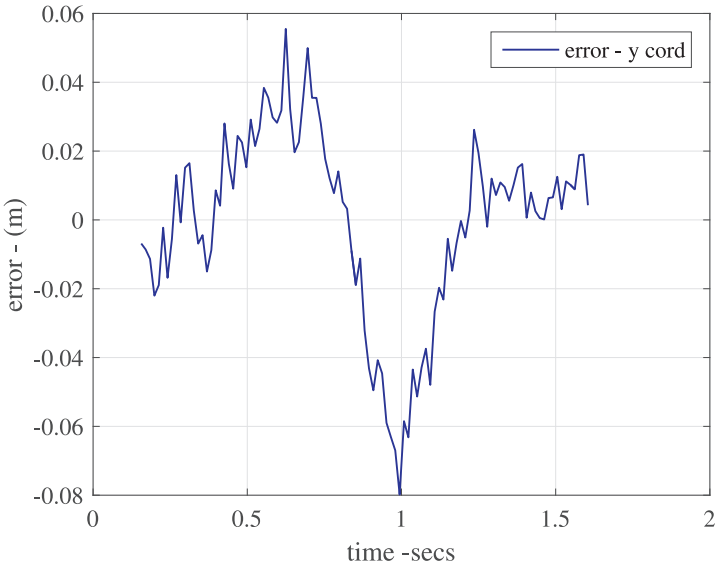

Figure 67: Case 6: Error in y-position

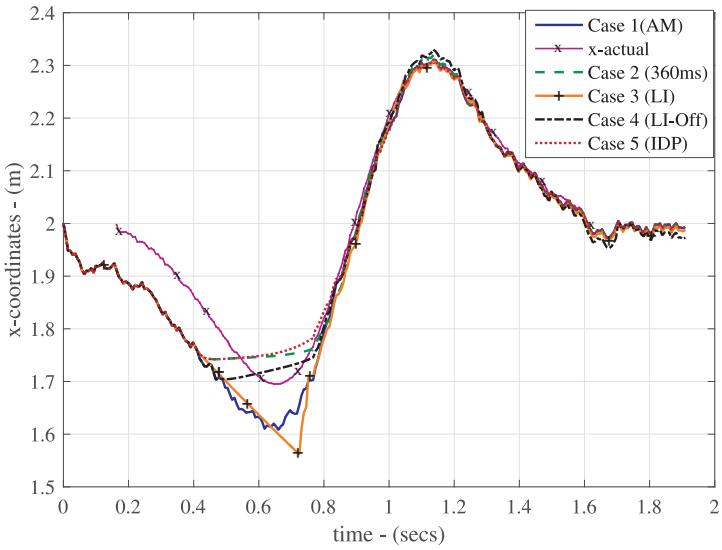

Figure 68: Comparison of the estimated x-positions. All the results are presented for a single initial condition for estimator with (2, 1.8048) m coordinates and π rads orientation.

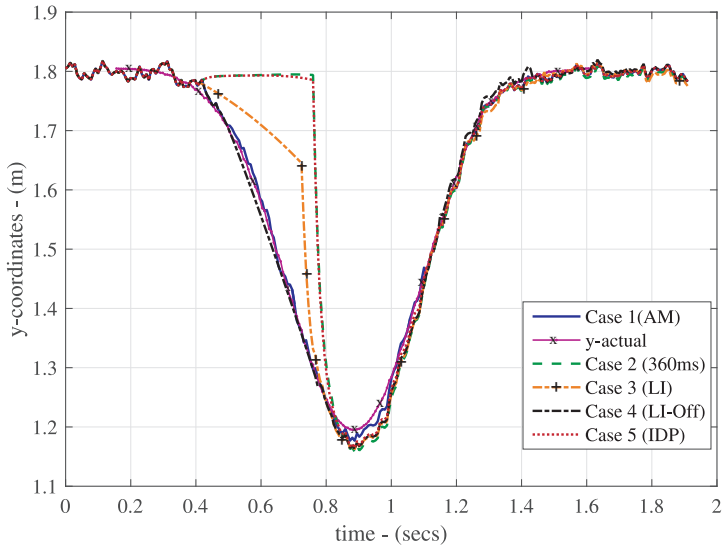

Figure 69: Comparison of the estimated y-positions. All the results are presented for a single initial condition for estimator with (2, 1.8048) m coordinates and π rads orientation.

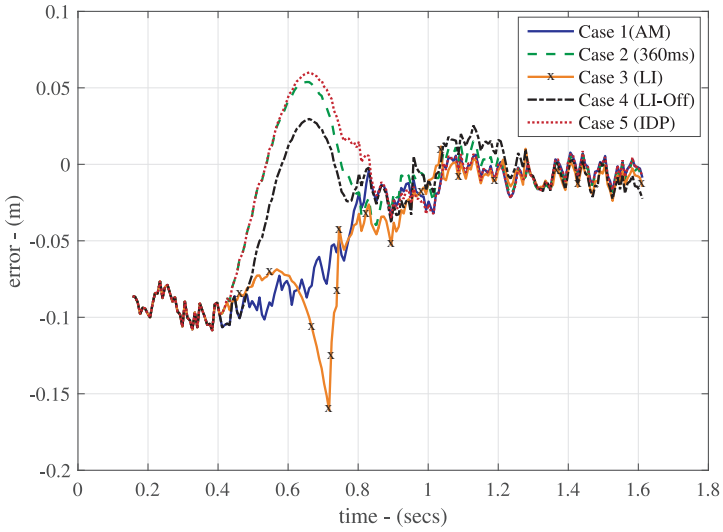

Figure 70: Comparison of error in estimated x-positions vs actual position.

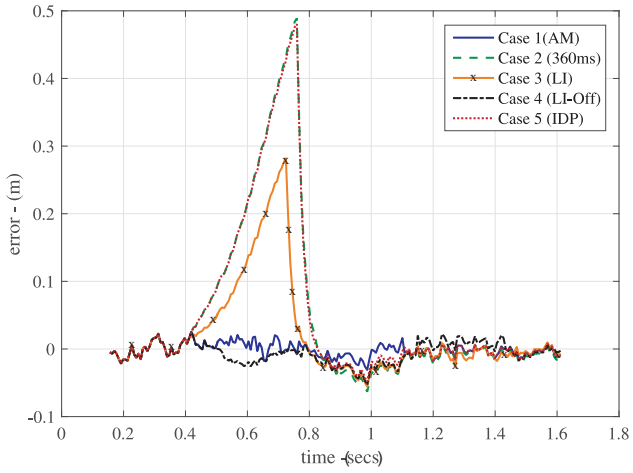

Figure 71: Comparison of error in estimated y-positions vs actual position.

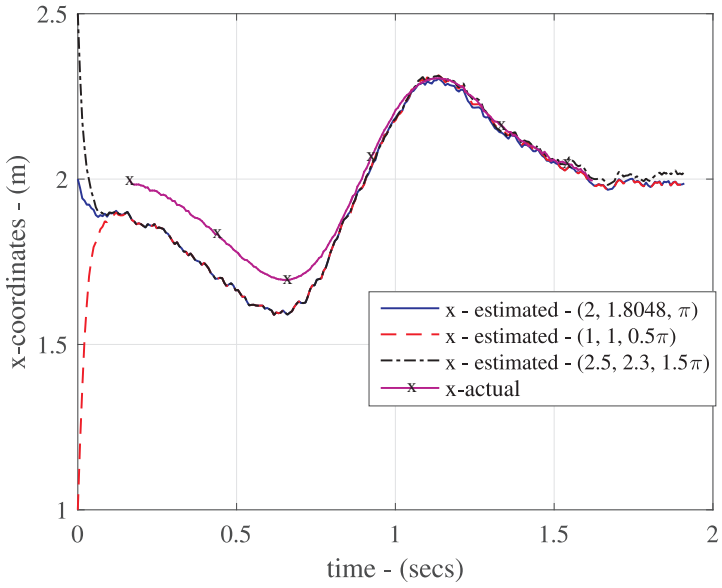

Figure 72: Case 7: Estimated x-position using measured data from two readers.

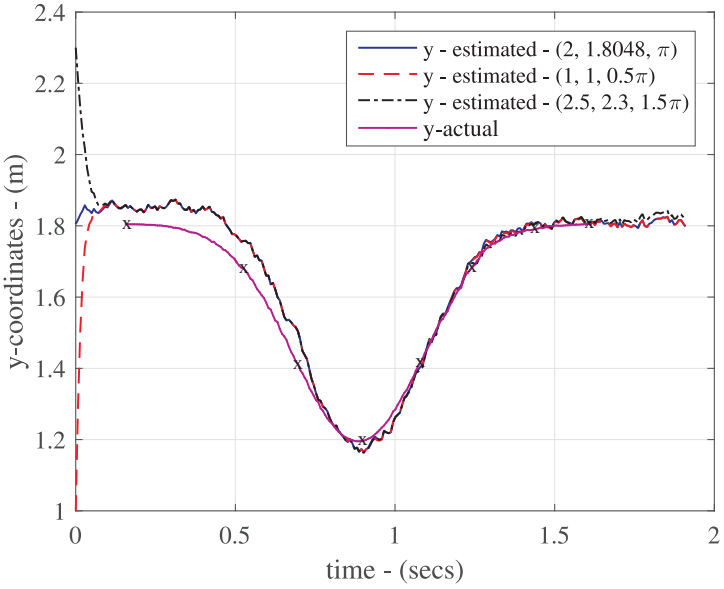

Figure 73: Case 7: Estimated y-position using measured data from two readers.

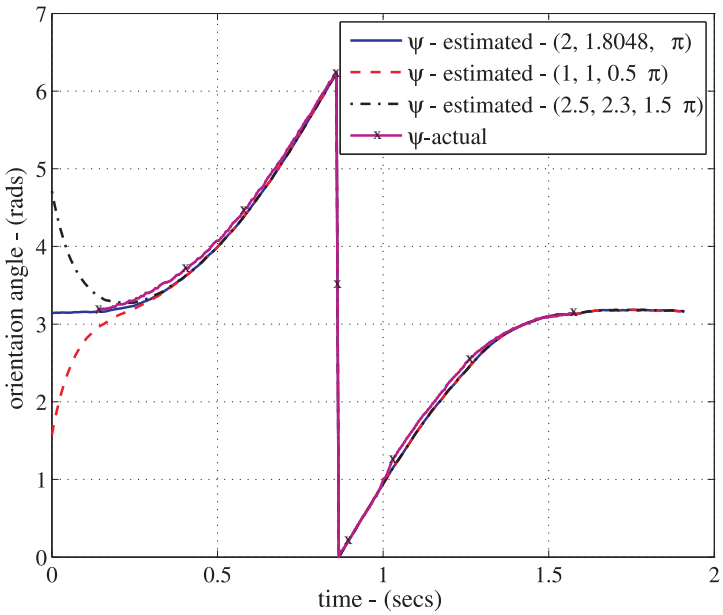

Figure 74: Case 7: Estimated orientation angle using measured data from two readers.

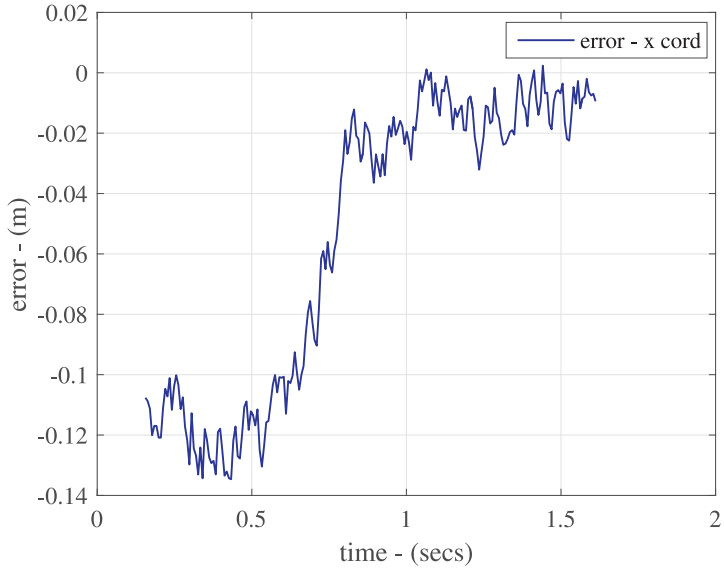

Figure 75: Case 7: Error in x-position.

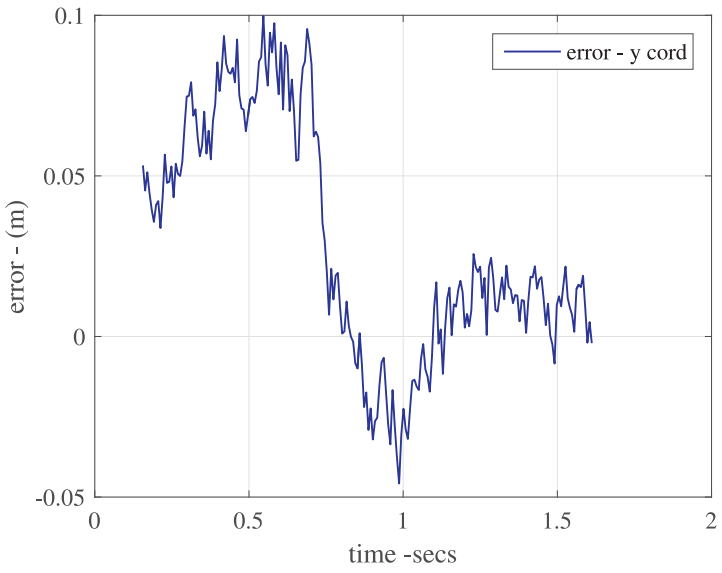

Figure 76: Case 7: Error in y-position.

CHAPTER V

CONCLUSION

5.1 Concluding Remarks

The ubiquitous presence of RFID-based devices permits the utilization of this technology for localization applications. We presented a new type of fine-scale wireless 2D position estimation technology that provides both unprecedented precision and range. Hybrid inertial microwave reflectometry (HIMR), is a wireless localization technique that powerfully illustrates the concept of *sensor fusion* – using multiple, disparate sensor measurements to synthesize a single, superior estimation of position. In HIMR, a microwave reader retrieves multi-axis inertial data from a low-energy microwave backscatter sensor. The HIMR algorithm then fuses both inertial data and the RF signature of the backscattered signal to produce a motion-capture grade estimate of position and/or orientation. Narrowband experiments at 5.8 GHz have demonstrated a system that can produce a one-dimensional accuracy of 2 mm and two-dimensional accuracy within 20 mm.

A motion-capture grade wireless localization system could revolutionize smartphone applications, augmented reality experiences, autonomous vehicle navigation, and unmanned aerial vehicle way-fairing, as well as adding a complete new dimension of functionality to emerging internet-of-things (IoT) devices. As one usage scenario, we envision a low-powered, light-weight drone equipped with an HIMR tag that can effortlessly navigate, monitor, and inventory a vast shipping container field at a port. Another usage could be sport players equipped with tiny HIMR tags that capture the entire choreography of a match for scientific or entertainment purposes. Ubiquitous, motion-capture grade localization technology unlocks an uncountable number

of future applications.

Our work investigated, introduced, and extended the nascent HIMR concept to a three-dimensional technique (adding multiple readers), while adding extra sensor data (gyrometry and mangetometry), enhanced orientation sensing (designing multi-antenna tags [85]), additional RF signature information (through frequency hopping [86]), and overall range (sensors equipped with QTRs [87]).

The HIMR technique is intrinsically cross-cutting and multi-disciplinary. This proposed research cultivates concepts, expertise, skills, and potential inventions that align with exploding consumer and industry interest in low-powered telemetry, ultra-connected sensors, and IoT applications. The results from this work promise to disrupt existing motion-capture grade localization technologies – which have severe range and environmental limitations – using hardware and antennas that already exist in every smartphone. Today's smartphones are already equipped with 9-axis position sensing, a microwave antenna, and RF switches. With little modification, these phones could become HIMR tags; with long-range, ultra-precise localization and orientation capability. An entirely new class of low-powered sensors could also be deployed throughout our environment and incorporated into a next-generation cellular network.

5.2 Major Contributions

Major contributions of this work are as follows:

1. **Motion capture tags**: During the course of research, 6-DOF and 9-DOF motion capture tags were developed for experiments. As per the conducted literature survey, no one has developed such an RFID tag before which can provide the motion parameters such as acceleration, rotation and orientation to be used for L&T. Therefore, the developed motion capture tags are the first of their kind.

2. **Two 5.8 GHz RFID systems**: A total of three RFID systems were required for the experiment and analysis of the two-dimensional HIMR algorithm. Two additional RFID systems were developed besides the one already available in the laboratory. All the systems were networked and integrated using a single reference and timing source for time synchronized measurements at all RFID nodes.

3. **Georgia Tech wireless motion capture protocol**: A Georgia Tech wireless motion capture protocol was developed for motion capture tags to extract the information from inertial sensors and backscatter it in the form of customized packets.

4. **Survey of state-of-the-art L&T techniques**: A literature survey was conducted to investigate the various methods of RFID-based L&T techniques and the position estimation accuracies that were obtained. Using these data, a performance benchmark for HIMR was obtained.

5. **Theoretical model for single and multidimensional HIMR-based L&T**: This work presented the theoretical model and subsequent observability analysis of the single and multidimensional HIMR estimator, which is the first of its kind to be used for L&T of tagged objects.

6. **Experimental setup and results**: The experimental setup required to test the HIMR scheme was presented in detail along with subsequent results. The analysis showed that the proposed HIMR scheme provides orders of magnitude better positional accuracy.

7. **Theoretical CRLBs for magnitude and phase difference**: Theoretical CRLB were derived for the estimation of magnitude and phase difference parameters from the received signal under different SNRs scenarios. These are

given in appendix A.

8. **Easily tunable Sigma-dipole antenna**: An easily tunable Sigma-dipole antenna at 915 MHz was designed, developed and integrated with existing toll tag circuitry for Intel Corporation. The Sigma-dipole antenna is being used by Intel on their products.

5.3 Publications

5.3.1 Journal Articles

- M.B. Akbar, D.G. Taylor, and G.D. Durgin, "Hybrid inertial microwave reflectometry for mm-scale tracking in RFID systems", *IEEE Transactions on Wireless Communications*, Vol. 14, No. 12, December 2015, pp. 6805–6814.

- F. Amato, C.W. Peterson, M.B. Akbar, and G.D. Durgin, "Quantum-tunneling RFID tags for long-range and low-power microwave applications", *IEEE Transactions on Microwave Theory and Techniques*, (Under Review).

5.3.2 Conference Articles (Peer reviewed)

- M.B. Akbar, Cheng Qi, M. Alhassoun, and G.D. Durgin, "Orientation sensing using backscattered phase from multi-aAntenna tag at 5.8 GHz", *IEEE International Conference on RFID*, Orlando, FL, May 2016, pp. 237–244.

- M.B. Akbar, Cheng Qi, and G.D. Durgin, "Analysis of E-patch antenna performance over various dielectric materials at 2.4 GHz", *IEEE International Symposium on Antennas & Propagation*, Fajardo, Puerto Rico, July 2016.

- M.B. Akbar, F. Amato, A. Classen, and G.D. Durgin, "Broadband backscatter based technique to identify the presence of skimming electronics on payment terminals", *IEEE Radio and Wireless Symposium*, Austin, TX, January 2016, pp. 141–144.

- M.B. Akbar, D.G. Taylor, and G.D. Durgin, "Amplitude and phase difference estimation bounds for multisensor based tracking of RFID tags", *IEEE International Conference on RFID*, San Diego, CA, April 2015, pp. 105–112.

- F. Amato, C.W. Peterson, M.B. Akbar, and G.D. Durgin, "Long range and low powered RFID tags with tunnel diode", *IEEE International Conference on RFID Technology and Applications*, Tokyo, Japan, September 2015, pp. 182–187, (**Best Paper Award**).

- M.B. Akbar, F. Amato, G.D. Durgin, G. Pisharody, S-Y. Suh, "RFID tag load impedance measurement using backscattered signal", *IEEE International Symposium on Antennas & Propagation*, Vancouver, Canada, July 2015, pp. 1762–1763.

- G.D. Durgin, C.R. Valenta, M.B. Akbar, M.M. Morys, B.R. Marshall, and Y. Lu, "Modulation and sensitivity limits for backscatter receivers", *IEEE International Conference on RFID*, Orlando, FL, April 2013, pp. 124–130.

- M.M. Morys, M.B. Akbar, and G.D. Durgin, "Malevolent object detection using microwave RFID tags", *IEEE International Conference on RFID*, Orlando, FL, April 2013, pp. 50–57.

- M.B. Akbar, M.M. Morys, C.R. Valenta, and G.D. Durgin, "Range improvement of backscatter radio systems at 5.8GHz using tags with multiple antennas", *IEEE International Symposium on Antennas & Propagation*, Chicago, IL, July 2012, pp. 1–2.

- C.R. Valenta, R. Hasse, M.B. Akbar, W. Hunsicker, K. Naishadham, and G.D. Durgin, "Omnidirectional loop antenna for a 5.8 GHz microwave backscatter RFID tag", *IEEE International Symposium on Antennas & Propagation*, Chicago, IL, July 2012, pp. 1–2

5.3.3 Masters Thesis

M.B. Akbar, "Design and prototype development of motion and shock sensing RF tag at 5.8 GHz", *Masters Thesis, www.smartech.gatech.edu*.

5.3.4 Technical Reports

- M.B. Akbar, F. Amato, and G.D. Durgin, "Electromagnetic Integrity and Security Assay (ELISA)", *Georgia Tech and NCR Corporation*, May 2015.
- M.B. Akbar, F. Amato, and G.D. Durgin, "Intel RFID Toll tag Project: Phase I Final Report", *Georgia Tech and Intel Corporation*, May 2014.
- M.B. Akbar, M.M. Morys, and G.D. Durgin, "FDI-embedded microwave RFID-based skimmer detection system", *Georgia Tech and NCR Corporation*, June 2013.

CHAPTER VI

FUTURE WORK

The following future steps are proposed to enhance and continue the research on the HIMR technique:-

- In this work, the data was recorded and post-processed for analysis. It is recommended that the HIMR algorithm may be incorporated in the reader's software for real time processing of localization and tracking of the tag.

- This work presented the L&T of a tagged object in a plane. In future, the HIMR scheme may be extended for localization and tracking of objects in three dimensions. The state-space model may be developed to incorporate the third dimension and its associated sensory information. Although a new observability analysis would be required to guarantee the suitability of the proposed sensor set, the methods reported in this work would still apply.

  Two-dimensional HIMR requires three pylons to track the tagged object in any type of planar motion. For the three-dimensional HIMR experiments in future, a four-pylon setup may be explored which allows long-range localization and tracking in 2D and 3D. The ability to get absolute position with mm-precision from each of the four pylons indicates operation of a 3D position estimation system that far surpasses any existing technology in terms of accuracy, simplicity, size, and range.

- Interference and tag collision are the common problems in RFID systems which can hamper the HIMR scheme based L&T. This could be mitigated by using frequency hopping RFID systems which are not only more resilient to interference

but also provide an additional set of information that can be used to improve localization accuracy. Frequency hopping capability will also make system more resilient to multipath and fading.

The current reader unit at Georgia Tech works on a single, static frequency within the unlicensed 5.8 GHz band. However, it is flexible and can be programmed to run in a frequency-hopping mode. It is envisioned that a frequency-hopping algorithm will derive more localization information and estimation reliability in the HIMR scheme. Moreover, it would also be suitable for avoiding any potential interferer in this band such as wireless networking signals.

A key task will be to incorporate a frequency-hopping algorithm for the custom Georgia Tech 5.8 GHz frequency synthesizer boards. The existing Georgia Tech 5.8 GHz reader has a programmable microcontroller that drives a crystal-disciplined voltage-controlled oscillator with programmable phase-locked loop controller. The unit can be programmed with a designed frequency-hopping algorithm that uses the full 150 MHz of unlicensed spectrum across the 5.8 GHz band for data collection. Synchronizing the frequency with the data acquisition will allow the collection of truly coherent broadband measurements.

- A tunnel diode-based load modulating HIMR tag using quantum tunneling reflection [87] may be developed and utilized in the investigation of long-range HIMR.

- A stochastic based HIMR-scheme may be investigated in future study and its results may be compared with the work presented in this thesis.

- The efficiency of HIMR may be tested with multiple tagged objects.

- The CRLBs for multi-dimensional HIMR in the presence of colored noise may be developed.

- In this work, three pylons were simultaneously used to perform the RF channel data (received signal amplitude and phase) and inertial measurements, based on *monostatic* measurement where RF information is only recorded at the pylon of origin of the CW signal. In this current work, a *bistatic* RF tag scatter between different pylons is not measured. Thus, for a three-pylon system, there are 3 monostatic links and 6 additional bistatic links that could provide localization information.

  In the future, inclusion of bistatic link measurements could also be incorporated in the estimation process. This will not only add another sensing variable and but will help in mitigating the fading due to interference.

APPENDIX A

AMPLITUDE AND PHASE DIFFERENCE ESTIMATION BOUNDS FOR MULTISENSOR BASED TRACKING OF RFID TAGS

A.1 Introduction

Radio frequency identification (RFID) systems with their inexpensive technology, easy deployment, and maintenance offer practicable solutions for object L&T [88]. The accuracy performance of L&T related applications of RFID technology can be greatly improved by fusing information from multiple sensors [48].

L&T of RFID systems in itself can be regarded as an application of parameter estimation where we estimate the position of an object by gathering the positional data from various sensing sources [89]. To evaluate the accuracy of any estimator, the Cramer-Rao Lower Bound is perceived as a well-established and crucial reference [90]. This chapter presents the Cramer-Rao Lower Bounds (CRLB) for the backscattered signal amplitude and backscattered packet-to-packet phase difference due to propagation in an RFID system. Before formulating the CRLBs, the probability density functions (PDFs) of the above quantities will be discussed in high and low signal-to-noise ratio (SNR) scenarios, respectively. Consequently, the corresponding CRLBs will be derived for both SNR cases. The HIMR scheme utilizes the received signal strength (RSS), received signal phase difference, and inertially sensed backscattered accelerometer data to track and locate the RFID-tagged object. It is therefore essential to determine the lower bounds on the estimation of these parameters used for L&T in HIMR. A large number of bounds such as Hammersley-Chapman-Robbins, Cramer-Rao, McAulay-Hofstetter, Kendall-Stuart,

Bhattacharyya, Seidman, Ziv-Zakai, Bobrovsky-Zakai, Weiss-Weinstein and Kiefer exist in the literature [90–95]. However, CRLB is a more commonly referenced and easily computable bound.

As mentioned earlier, the CRLB is the most commonly referenced bound for localization techniques; therefore, a vast amount of research literature is available for calculating and applying this bound, where a subset relevant to RFID is referenced here [96–101]. [96] introduced the fundamental information on statistical signal processing for localization in wireless sensor networks. The authors discussed in detail the procedures to work out the CRLB on location estimation using a given set of measured position data. [97] used an RSS-based, unscented Kalman filter to locate RF tags and compared its performance with a predefined posterior CRLB for the RSS. [98] studied the accuracy of various RSS-based RFID localization algorithms. For comparison, they derived CRLB using a frequency-dependent path loss model with log-normal PDF. In [99], the authors discussed the performance of their localization estimators in the presence of Gamma and Rayleigh fading. The localization is performed using time-of-arrival-based measurements and compared by deducing the CRLB for such measurements. It was concluded that fading has an adverse effect on the CRLB in such localization scenarios. The effectiveness of target position estimation using coherent Multiple-Input-Multiple-Output (MIMO) radars has been examined in [100], and the CRLB for coherent processing was investigated. It was inferred that the accuracy of the estimation is inversely proportional to the carrier frequency and signal bandwidth. [101] argues the significance of using complex and magnitude data to estimate the signal amplitude and noise variance for maximum likelihood (ML) method.

This chapter calculates CRLB for received signal amplitude and phase difference for RFID tag localization and tracking. Section A.2 discusses probability density functions for amplitude and phase difference for high and low SNR cases. Section

A.3 briefly introduces CRLB followed by derivation of bounds for the parameters and discussion on CRLB.

A.2 Probability Density Function

A.2.1 Received Signal Amplitude

In RFID systems, the received signal has both amplitude and phase and can be expressed by (56), where V is the complex received signal with an in-phase component I and quadrature-phase component Q. It is assumed that both I and Q are modeled as the superposition of a large amplitude components with independent, identically-distributed (i.i.d.) AWGN of variance σ^2.

$$V = I + jQ \tag{56}$$

The magnitude of the measured noisy received signal is calculated by taking the root of the sum of squared I and Q denoted by $v = \sqrt{I^2 + Q^2}$. This nonlinear mapping results in a Rician distribution function for the magnitude v. Such a case occurs when there are strong line-of-sight components along with zero mean AWGN. The PDF of the measured noisy signal denoted by $f_v(v)$ is given by the following [102]:

$$f_v(v) = \frac{v}{\sigma^2} \exp\left(-\frac{(v^2 + {V_o}^2)}{2\sigma^2}\right) I_0\left(\frac{vV_o}{\sigma^2}\right) \tag{57}$$

where V_o is the amplitude of the noiseless signal and $I_0(.)$ is the zeroth order modified Bessel function of the first kind. The plot of $f_v(v)$ for SNR values, $\frac{V_o}{\sigma}$ is illustrated in Figure 77. It is evident from Figure 77 that at low SNR, (SNR $= \frac{V_o}{\sigma}$), $f_v(v)$ resembles a Rayleigh distribution shape but for higher SNR, (i.e. as $\frac{V_o}{\sigma}$ increases), $f_v(v)$ converges to Gaussian distribution with mean and variance properties described by $\mathcal{N}(\sqrt{{V_o}^2 + \sigma^2}, \sigma^2)$ [103]. Therefore, the approximated Gaussian distribution for large SNR can be written as

$$f_v(v) \approx \frac{1}{\sqrt{2\pi\sigma^2}} \exp\left(-\frac{(v - \sqrt{{V_o}^2 + \sigma^2})^2}{2\sigma^2}\right) \tag{58}$$

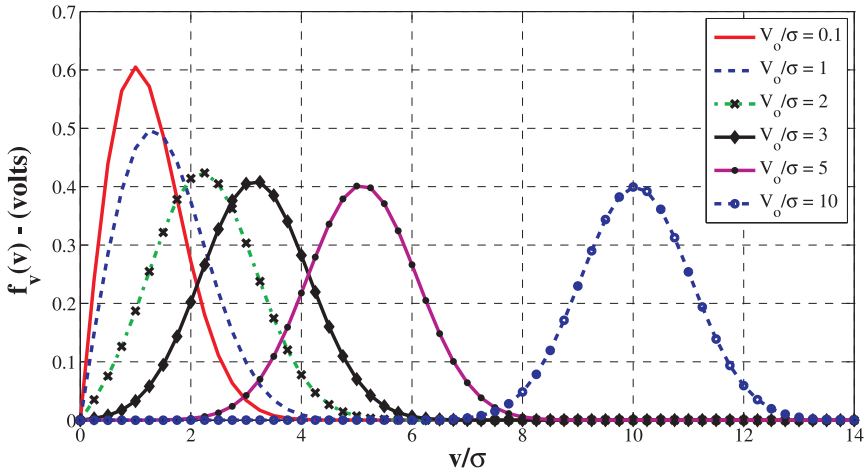

Figure 77: Effect of SNR is illustrated on the Rician distribution. It is observed that for larger $\frac{V_o}{\sigma}$ the Rician distribution converges to Gaussian curve.

[103] also discusses in detail the Gaussian approximation of Rician distribution along with the discussion on the effect of the Rician factor which is given as $K = \frac{{V_o}^2}{2\sigma^2}$.

A.2.2 Received Signal Phase

Using the phase coherence feature of RFID transceivers, the noisy phase ϕ of the received signal can be deciphered using

$$\phi = \arctan\left(\frac{Q}{I}\right) \tag{59}$$

[104] described the PDF of the noisy phase $f_\phi(\phi)$ under the nonlinear arctangent function by the following expression:

$$f_\phi(\phi) = \frac{1}{2\pi}\exp\left(\frac{-{V_o}^2}{2\sigma^2}\right)\left(1 + \frac{V_o}{\sigma}\sqrt{2\pi}\cos\phi\exp\left(\frac{{V_o}^2\cos\phi^2}{2\sigma^2}\right)\right.$$
$$\left.\left[1 - Q_f\left(\frac{V_o\cos\phi}{\sigma}\right)\right]\right) \tag{60}$$

where $Q_f(\cdot)$ describes a Q-function. The intricate expression in (60) can be plotted for various SNR values as illustrated in Figure 78. As evident from Figure 78, for very low and zero SNRs, (60) is simplified to a uniform distribution, which implies

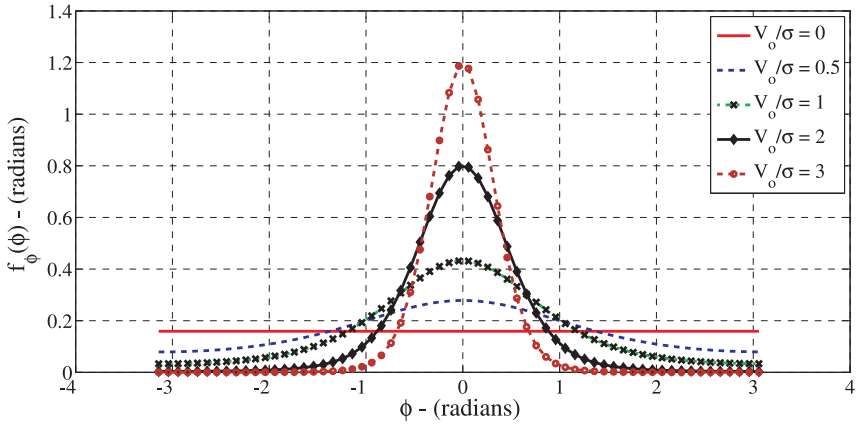

Figure 78: Effect of SNR is illustrated on the phase PDF. It is observed that for larger $\frac{V_o}{\sigma}$ the distribution approximates to Gaussian curve whereas for zero SNR it converges to uniform distribution.

that every phase value is equally likely [102].

$$f_\phi(\phi) = \frac{1}{2\pi} \qquad -\pi < \phi < \pi \tag{61}$$

While, as the SNR increases, the noise will have little effect on the variation of ϕ, as a result $f_\phi(\phi)$ approximates to a Gaussian distribution (Figure 78), which after some manipulation of (60) can be written as [105]

$$f_\phi(\phi) \approx \frac{1}{\sqrt{2\pi(\frac{\sigma}{V_o})^2}} \exp\left(-\frac{\phi^2}{2(\frac{\sigma}{V_o})^2}\right) \tag{62}$$

which shows that for high SNR, the phase distribution expression in (60) is simplified to zero mean Gaussian distribution.

A.2.3 Phase Difference

The HIMR scheme in [48] employs the backscattered packet-to-packet phase difference to discern the velocity of the tagged object. Therefore, the PDF analysis of the phase difference is of more interest than the simple phase itself. The phase difference between the two packets is represented by $\varphi = \phi_k - \phi_{k-1}$ where $k \in \mathbb{N}$. For the case of large SNR, both ϕ_k and ϕ_{k-1} are i.i.d. zero mean Gaussian random

variables, therefore, the resultant phase difference φ is also zero mean Gaussian under linear difference operator. The distribution is exactly represented by (62) where ϕ is replaced by φ. Moreover, we can represent the noiseless phase difference estimate by ϑ.

However, for the low SNR case, both ϕ_k and ϕ_{k-1} are i.i.d. uniform random variables. The difference of two independent standard uniform random variables has the standard triangular distribution [106]. Under this case, the PDF for φ is expressed by (63) with zero mean and variance of $\frac{\pi^2}{6}$, and is shown in Figure79.

$$f_{\varphi}(\varphi) = \frac{(\pi - \mid \varphi \mid)}{\pi^2} U(\pi - \mid \varphi \mid) \qquad -\pi < \varphi < \pi \tag{63}$$

where $U(.)$ is the unit step function.

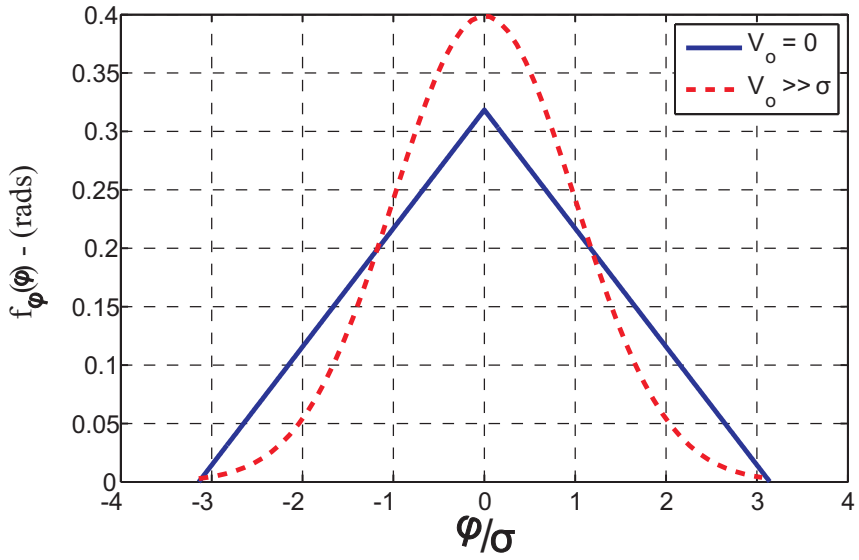

Figure 79: PDF for the phase difference φ for the case $V_o = 0$ and $V_o \gg \sigma$.

A.3 Cramer-Rao Lower Bound

Cramer and Rao devised a method to extract the lower bound (CRLB) on the variance of the unbiased estimators that estimate stochastic parameters [107]. The CRLB states that the variance of an unbiased estimate $\hat{\alpha}$ of parameter α is greater

than or equal to its CRLB i.e. $\sigma^2(\hat{\alpha}) \geq CRLB(\alpha)$ [90]. The CRLB is used to judge the performance of a proposed estimator where an it is not categorized as a good estimator if its variance does not approach its CRLB. On the other hand, if an estimator attains its CRLB, then it is considered as the minimum variance unbiased estimator. The CRLB of an estimator for any parameter α with PDF $f_p(p;\alpha)$ is determined by the following [90]:

$$CRLB(\alpha) = \frac{1}{-E\left[\frac{\partial^2 \ln f_p(p;\alpha)}{\partial \alpha^2}\right]} \tag{64}$$

where $E[.]$ is the expectation taken with respect to $f_p(p;\alpha)$. In our case, we want V_o (noiseless estimate of the received signal amplitude) and ϑ (noiseless estimate of the phase difference), therefore we will use $f_v(v;V_o)$ and $f_\varphi(\varphi;\vartheta)$ PDFs for multiple observations.

A.3.1 CRLB - Received Signal Amplitude Estimation

First, we consider the N independent magnitude data points given by:

$$\mathbf{v} = (v_1, v_2, ..., v_N) \tag{65}$$

with Rician distribution to estimate the amplitude of the signal V_o. The joint Rician distribution can be written as

$$f_{\mathbf{v}}(\mathbf{v};V_o) = \prod_{n=1}^{N} \frac{v_n}{\sigma^2} \exp\left(-\frac{({v_n}^2 + {V_o}^2)}{2\sigma^2}\right) I_0\left(\frac{v_n V_o}{\sigma^2}\right) \tag{66}$$

Applying the definition given in (64) on (66), we can find the $CRLB_a(V_o)$ *for the low SNR* case as

$$CRLB_a(V_o) = \frac{\sigma^2}{N}\left(E\left[\frac{v^2 {I_1}^2\left(\frac{V_0 v}{\sigma^2}\right)}{\sigma^2 {I_0}^2\left(\frac{V_0 v}{\sigma^2}\right)}\right] - \frac{{V_o}^2}{\sigma^2}\right)^{-1} \tag{67}$$

where $CRLB_a(V_o)$ is the CRLB of received signal amplitude for low SNR case and $I_1(.)$ is the first order modified Bessel function of the first kind. Similarly, for *high SNR* we consider the N independent magnitude data points with Gaussian distribution for

estimated amplitude of the signal V_o. The joint Gaussian distribution can be written as

$$f_{\mathbf{v}}(\mathbf{v}; V_o) \approx \prod_{n=1}^{N} \frac{1}{\sqrt{2\pi\sigma^2}} \exp\left(-\frac{(v_n - V_o)^2}{2\sigma^2}\right) \tag{68}$$

Applying (64) on (68), the $CRLB_b(V_o)$ *for high SNR* case is derived as

$$CRLB_b(V_o) = \frac{\sigma^2}{N} \tag{69}$$

where $CRLB_b(V_o)$ is the CRLB of received signal amplitude for high SNR case.

A.3.2 CRLB - Phase Difference Estimation

Again considering N phase difference data points given by:

$$\boldsymbol{\varphi} = (\varphi_1, \varphi_2, ..., \varphi_N) \tag{70}$$

the joint triangular distribution for noiseless phase difference estimate ϑ can be written as

$$f_{\boldsymbol{\varphi}}(\boldsymbol{\varphi}; \vartheta) = \prod_{n=1}^{N} \frac{(\pi - \mid \varphi_n \mid -\vartheta)}{\pi^2} U\left(\pi - \mid \varphi_n \mid\right) \quad -\pi < \varphi_n < \pi \tag{71}$$

The $CRLB_c(\vartheta)$ *for low SNR* case can be found using the definition given in (64) on (71), we get

$$CRLB_c(\vartheta) = \frac{\vartheta^2}{N} \tag{72}$$

where $CRLB_c(\vartheta)$ is the CRLB of the phase difference for *low SNR* case. Similarly for *high SNR*, the joint Gaussian distribution for noiseless phase difference estimate ϑ can be written as

$$f_{\boldsymbol{\varphi}}(\boldsymbol{\varphi}; \vartheta) \approx \prod_{n=1}^{N} \frac{1}{\sqrt{2\pi(\frac{\sigma}{V_o})^2}} \exp\left(-\frac{(\varphi_n - \vartheta)^2}{2(\frac{\sigma}{V_o})^2}\right) \tag{73}$$

We get the $CRLB_d(\vartheta)$ *for high SNR* case as

$$CRLB_d(\vartheta) = \frac{\sigma^2}{N{V_o}^2} \tag{74}$$

where $CRLB_d(\vartheta)$ is the CRLB of the phase difference for *high SNR* case. In matrix form, the combined CRLBs for the amplitude and the phase difference for both SNR cases can be summarized as follows:

Low SNR case

$$CRLB = \begin{bmatrix} CRLB_a(V_o) & 0 \\ 0 & CRLB_c(\vartheta) \end{bmatrix} \tag{75}$$

High SNR case

$$CRLB = \begin{bmatrix} CRLB_b(V_o) & 0 \\ 0 & CRLB_d(\vartheta) \end{bmatrix} \tag{76}$$

A.3.3 Discussion

It can be observed from all CRLB equations that the CRLB is inversely proportional to the number of observations considered for the estimation of the amplitude and phase difference parameters. For the *high SNR case*, the magnitude CRLB (69) is dependent on the variance and number of the observation points while the phase difference CRLB (74) is dependent on the variance, number of observations, and estimated magnitude of the data. For *the low SNR case*, the magnitude CRLB (67) is dependent on the SNR, the number of observations, and the Bessel functions-based expected value which can be evaluated using Monte Carlo simulations. The phase difference CRLB (72) is dependent upon the phase difference itself and the number of observations.

A.4 Conclusion

In this chapter, the probability density functions of the received signal amplitude and the received signal phase were investigated under low and high SNR cases. Under low SNR scenarios, the received signal magnitude showed Rician distribution, while the received signal phase depicted a uniform distribution. Whereas under high SNR

scenarios, both the received signal magnitude and received signal phase showed Gaussian distribution behavior. Moreover, the phase difference required for estimation of the velocity showed triangular and Gaussian distribution in low and high SNR cases respectively. Correspondingly, the CRLB was derived for estimation of received signal amplitude and received signal phase difference. The CRLB was found to be inversely proportional to the number of data points used for the desired parameter estimation.

APPENDIX B

C AND THE OBSERVABILITY MATRIX

This appendix details the **C**-matrix entries and the observability matrix.

B.1 C-matrix entries

$$C_{11} = C_{22} = \frac{(x - x_1)}{h_1} \tag{77}$$

$$C_{14} = C_{25} = \frac{(y - y_1)}{h_1} \tag{78}$$

$$C_{21} = \frac{(y - y_1)\left((y - y_1)\dot{x} - (x - x_1)\dot{y}\right)}{{h_1}^3} \tag{79}$$

$$C_{24} = \frac{(x - x_1)\left((x - x_1)\dot{y} - (y - y_1)\dot{x}\right)}{{h_1}^3} \tag{80}$$

$$C_{31} = C_{42} = \frac{(x - x_2)}{h_2} \tag{81}$$

$$C_{34} = C_{45} = \frac{(y - y_2)}{h_2} \tag{82}$$

$$C_{41} = \frac{(y - y_2)\left((y - y_2)\dot{x} - (x - x_2)\dot{y}\right)}{{h_2}^3} \tag{83}$$

$$C_{44} = \frac{(x - x_2)\left((x - x_2)\dot{y} - (y - y_2)\dot{x}\right)}{{h_2}^3} \tag{84}$$

$$C_{51} = C_{62} = \frac{(x - x_3)}{h_3} \tag{85}$$

$$C_{54} = C_{65} = \frac{(y - y_3)}{h_3} \tag{86}$$

$$C_{61} = \frac{(y - y_3)\left((y - y_3)\dot{x} - (x - x_3)\dot{y}\right)}{{h_3}^3} \tag{87}$$

$$C_{64} = \frac{(x - x_3)\left((x - x_3)\dot{y} - (y - y_3)\dot{x}\right)}{{h_3}^3} \tag{88}$$

$$C_{73} = \cos\psi \tag{89}$$

$$C_{76} = \sin\psi \tag{90}$$

$$C_{77} = -\ddot{x}\sin\psi + \ddot{y}\cos\psi \tag{91}$$

$$C_{83} = -\sin\psi \tag{92}$$

$$C_{86} = \cos\psi \tag{93}$$

$$C_{87} = -\ddot{x}\cos\psi - \ddot{y}\sin\psi \tag{94}$$

$$C_{97} = 1 \tag{95}$$

$$C_{108} = 1 \tag{96}$$

where (x_1, y_1), (x_2, y_2) and (x_3, y_3) are the fixed coordinates of the three readers.

B.2 Observability Matrix

The observability matrix is calculated using $\mathbf{C}$ and $\mathbf{A}$ in (36). The coefficient matrix $\mathbf{A}$ is a *nilpotent* whose $\mathbf{A}^3$ is all zeros, therefore, the size of the observability matrix is 30×9. The observability matrix is as follows:

$$
O = \begin{bmatrix}
C_{11} & 0 & 0 & C_{14} & 0 & 0 & 0 & 0 & 0 \\
C_{21} & C_{11} & 0 & C_{24} & C_{14} & 0 & 0 & 0 & 0 \\
C_{31} & 0 & 0 & C_{34} & 0 & 0 & 0 & 0 & 0 \\
C_{41} & C_{31} & 0 & C_{44} & C_{34} & 0 & 0 & 0 & 0 \\
C_{51} & 0 & 0 & C_{54} & 0 & 0 & 0 & 0 & 0 \\
C_{61} & C_{51} & 0 & C_{64} & C_{54} & 0 & 0 & 0 & 0 \\
0 & 0 & C_{73} & 0 & 0 & C_{76} & C_{77} & 0 & 0 \\
0 & 0 & C_{83} & 0 & 0 & C_{86} & C_{87} & 0 & 0 \\
0 & 0 & 0 & 0 & 0 & 0 & C_{97} & 0 & 0 \\
0 & 0 & 0 & 0 & 0 & 0 & 0 & C_{108} & 0 \\
0 & C_{11} & 0 & 0 & C_{14} & 0 & 0 & 0 & 0 \\
0 & C_{21} & C_{11} & 0 & C_{24} & C_{14} & 0 & 0 & 0 \\
0 & C_{31} & 0 & 0 & C_{34} & 0 & 0 & 0 & 0 \\
0 & C_{41} & C_{31} & 0 & C_{44} & C_{34} & 0 & 0 & 0 \\
0 & C_{51} & 0 & 0 & C_{54} & 0 & 0 & 0 & 0 \\
0 & C_{61} & C_{51} & 0 & C_{64} & C_{54} & 0 & 0 & 0 \\
0 & 0 & 0 & 0 & 0 & 0 & 0 & C_{77} & 0 \\
0 & 0 & 0 & 0 & 0 & 0 & 0 & C_{87} & 0 \\
0 & 0 & 0 & 0 & 0 & 0 & 0 & C_{97} & 0 \\
0 & 0 & 0 & 0 & 0 & 0 & 0 & 0 & C_{108} \\
0 & 0 & C_{11} & 0 & 0 & C_{14} & 0 & 0 & 0 \\
0 & 0 & C_{21} & 0 & 0 & C_{24} & 0 & 0 & 0 \\
0 & 0 & C_{31} & 0 & 0 & C_{34} & 0 & 0 & 0 \\
0 & 0 & C_{41}0 & 0 & C_{44} & 0 & 0 & 0 & \\
0 & 0 & C_{51} & 0 & 0 & C_{54} & 0 & 0 & 0 \\
0 & 0 & C_{61} & 0 & 0 & C_{64} & 0 & 0 & 0 \\
0 & 0 & 0 & 0 & 0 & 0 & 0 & 0 & C_{77} \\
0 & 0 & 0 & 0 & 0 & 0 & 0 & 0 & C_{87} \\
0 & 0 & 0 & 0 & 0 & 0 & 0 & 0 & C_{97}
\end{bmatrix} \tag{97}
$$

APPENDIX C

MOTOR MOTION TRAJECTORY

C.1 Modeling

The motion apparatus is shown in the photo below (80). The motor shaft is vertically oriented, and a plastic beam is symmetrically attached so that rotation of the beam will occur in the horizontal plane; since the construction of the apparatus is imperfect, the rotational motion will not be precisely confined to the horizontal plane. The beam is quite thick and long, and hence it is characterized by a significant inertia. In order to accurately control the motion of the beam, it is necessary to determine both the inertia and the speed-dependent damping of the apparatus.

The dynamics of the apparatus are ideally governed by Newton's law in the horizontal plane along with the quasi-steady-state relationship between armature voltage and armature current. The resulting differential equation is

$$J\frac{d\omega}{dt} = K\left(\frac{v - K\omega}{R}\right) - B\omega$$

where ω is the angular speed, v is the armature voltage, J and B are the inertia and viscous friction coefficient of the rotor and load, K is the magnetic coupling coefficient, and R is the armature resistance. This differential equation may be rewritten in the form

$$\frac{d\omega}{dt} = -\alpha\omega + \beta v, \quad \alpha = \frac{BR + K^2}{JR}, \quad \beta = \frac{K}{JR}$$

where two coefficients, α and β, summarize the influence of the various physical parameters. These two remaining parameters may be identified by a step response test. If a constant voltage V is applied with no initial rotation then the resulting

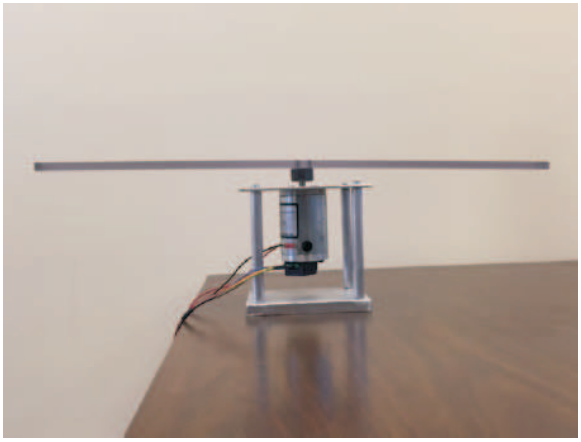

Figure 80: Picture of the motion apparatus. The motor shaft is vertically oriented, and a plastic beam is symmetrically attached so that rotation of the beam will occur in the horizontal plane.

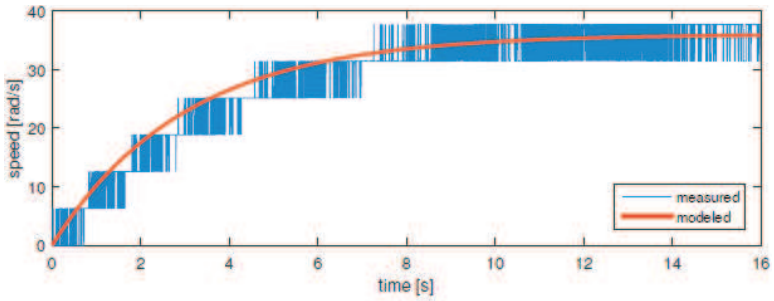

Figure 81: Motor Parameters

response will be the exponential function

$$\omega(t) = V\frac{\beta}{\alpha}\left(1 - e^{-\alpha t}\right), \quad t \geq 0.$$

Values for α and β in this response formula may be adjusted so as to approximately match measured step response behavior. The result of such an effort is shown in the plot comparison below; the noise on the speed measurement arises from the need to differentiate the quantized position measurement. This comparison is based on $V = 8$ [V], and results in the approximated parameters

$$\alpha = \frac{1}{3}\ [\text{rad/s}], \quad \beta = \frac{3}{2}\ [\text{rad/s}^2/\text{V}].$$

C.2 Trajectories

The motion of the apparatus is commanded by a reference trajectory for angular position. There is a positive acceleration region, a cruise region, and a negative acceleration region. Both acceleration regions occur on a time interval of length t_{accel}, with constant accelerations equal to $\pm\ddot{\theta}_{\text{accel}}$. The cruise region occurs on a time interval of length t_{cruise} and corresponds to a cruise speed equal to $\dot{\theta}_{\text{cruise}}$. Motion begins with position θ_{i} at time t_{i} and ends with position θ_{f} at time t_{f}. This motion profile is specified in terms of the interrelated coefficients t_{accel}, $\ddot{\theta}_{\text{accel}}$, t_{cruise}, $\dot{\theta}_{\text{cruise}}$, $t_{\text{f}} - t_{\text{i}}$ and $\theta_{\text{f}} - \theta_{\text{i}}$. By integrating acceleration to obtain speed, one constraint becomes

$$\dot{\theta}_{\text{cruise}} = \ddot{\theta}_{\text{accel}} t_{\text{accel}}.$$

By integrating speed to obtain position, another constraint becomes

$$\theta_{\text{f}} - \theta_{\text{i}} = \dot{\theta}_{\text{cruise}} \left(t_{\text{accel}} + t_{\text{cruise}} \right).$$

Simultaneous solution of these two constraints results in

$$\dot{\theta}_{\text{cruise}} = \frac{\theta_{\text{f}} - \theta_{\text{i}}}{t_{\text{accel}} + t_{\text{cruise}}}, \quad \ddot{\theta}_{\text{accel}} = \frac{\theta_{\text{f}} - \theta_{\text{i}}}{t_{\text{accel}} \left(t_{\text{accel}} + t_{\text{cruise}} \right)}.$$

Therefore, if the user specifies the parameters t_{accel}, t_{cruise}, θ_{i} and θ_{f}, then the reference trajectory for angular position, denoted by $r(t)$, may be expressed in the form

$$r(t) = \begin{cases} \theta_{\text{i}} + \frac{1}{2}\ddot{\theta}_{\text{accel}}(t - t_{\text{i}})^2 & , \ t \in \{\text{positive acceleration time interval}\} \\ \frac{1}{2}\left(\theta_{\text{i}} + \theta_{\text{f}}\right) + \dot{\theta}_{\text{cruise}}\left(t - \frac{1}{2}\left(t_{\text{i}} + t_{\text{f}}\right)\right) & , \ t \in \{\text{cruise time interval}\} \\ \theta_{\text{f}} - \frac{1}{2}\ddot{\theta}_{\text{accel}}(t_{\text{f}} - t)^2 & , \ t \in \{\text{negative acceleration time interval}\} \end{cases}$$

using precomputed values for $\dot{\theta}_{\text{cruise}}$ and $\ddot{\theta}_{\text{accel}}$.

The above type of single-stroke reference trajectory has been implemented with periodic cycling between an initial position θ_{i} and a final position θ_{f}. The travel time of a single stroke is $2t_{\text{accel}} + t_{\text{cruise}}$, and an additional dwell time t_{dwell} is placed at the end of each single stroke, resulting in a round-trip cycle time of $2\left(2t_{\text{accel}} + t_{\text{cruise}} + t_{\text{dwell}}\right)$.

A representative reference trajectory of this type is shown in the plot below, along with its Matlab implementation.

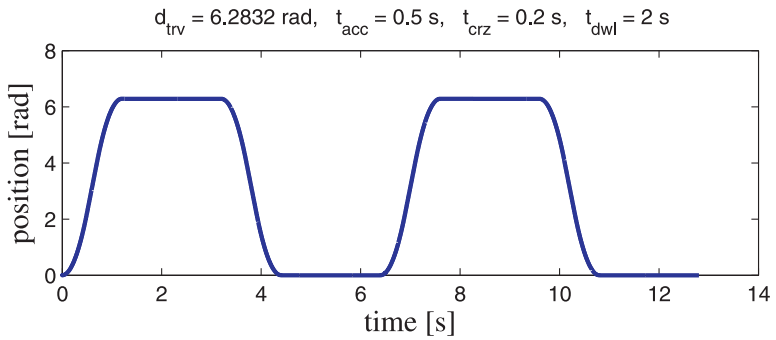


```
%% user input


d_trv = pi/4;

t_acc = 0.1;

t_crz = 0.1;

t_dwl = 0.2;


%% dependent parameters


spd = d_trv/(t_acc+t_crz);

acc = spd/t_acc;


t_trv = 2*t_acc+t_crz;

t_half = t_trv+t_dwl;

t_full = 2*t_half;


%% time trajectory


t = 0:0.001:2*t_full;
```

```
r = NaN(1,length(t));

for i = 1:length(t);

    tmod_full = mod(t(i),t_full);
    if tmod_full < t_half
        di = 0;
        df = d_trv;
        s = spd;
        a = acc;
    else
        di = d_trv;
        df = 0;
        s = -spd;
        a = -acc;
    end

    tmod_half = mod(t(i),t_half);
    if tmod_half < t_acc
        r(i) = di+0.5*a*tmod_half^2;
    elseif tmod_half < t_acc+t_crz
        r(i) = 0.5*d_trv+s*(tmod_half-0.5*t_trv);
    elseif tmod_half < t_trv
        r(i) = df-0.5*a*(t_trv-tmod_half)^2;
    else
        r(i) = df;
    end
```

```
end


%% result plot


subplot(211), plot(t,r,'LineWidth',2)
xlabel('time [s]'), ylabel('position [rad]')
title(strcat([...
    'd_{trv} = ', num2str(d_trv), ' rad,   ',...
    't_{acc} = ', num2str(t_acc), ' s,   ',...
    't_{crz} = ', num2str(t_crz), ' s,   ',...
    't_{dwl} = ', num2str(t_dwl), ' s']))
```

APPENDIX D

CHOICE OF TUNING MATRICES

D.1 Oscillations

The following tuning and resultant gain matrices were used which generated oscillations in the estimated states.

$$\mathbf{W} = \begin{bmatrix} 965 & 0 & 0 & 0 & 0 & 0 & 0 & 0 & 0 \\ 0 & 965 & 0 & 0 & 0 & 0 & 0 & 0 & 0 \\ 0 & 0 & 965 & 0 & 0 & 0 & 0 & 0 & 0 \\ 0 & 0 & 0 & 965 & 0 & 0 & 0 & 0 & 0 \\ 0 & 0 & 0 & 0 & 965 & 0 & 0 & 0 & 0 \\ 0 & 0 & 0 & 0 & 0 & 965 & 0 & 0 & 0 \\ 0 & 0 & 0 & 0 & 0 & 0 & 965 & 0 & 0 \\ 0 & 0 & 0 & 0 & 0 & 0 & 0 & 965 & 0 \\ 0 & 0 & 0 & 0 & 0 & 0 & 0 & 0 & 965 \end{bmatrix} \tag{98}$$

$$\mathbf{L} = \begin{bmatrix} 30.2 & 0.48 & 0.004 & 4.98 & 0.1 & 6.6 \times 10^{-4} & -1.1 \times 10^{-16} & -2.83 \times 10^{-15} & -1.4 \times 10^{-14} \\ 0.48 & 30.2 & 0.49 & 0.1 & 4.98 & 0.07 & -7.7 \times 10^{-16} & -2.4 \times 10^{-15} & -1.63 \times 10^{-16} \\ -0.1 & -0.03 & -3.63 \times 10^{-5} & -22.53 & -0.27 & -0.003 & -2.14 \times 10^{-15} & -1.31 \times 10^{-16} & -1.11 \times 10^{-15} \\ -0.03 & -0.1015 & 0.015 & -0.27 & -22.53 & -0.42 & 3.573 \times 10^{-15} & 3.21 \times 10^{-15} & -4.72 \times 10^{-16} \\ -7.33 & -0.09 & -9.25 \times 10^{-4} & 20.82 & 0.24 & 0.003 & 2.2 \times 10^{-15} & 8.24 \times 10^{-16} & 4.61 \times 10^{-15} \\ -0.09 & -7.33 & -0.14 & 0.24 & 20.82 & 0.4 & -3.31 \times 10^{-15} & -2.56 \times 10^{-15} & 5.01 \times 10^{-16} \\ -0.004 & -0.4911 & -31.07 & -3.36 \times 10^{-4} & -0.023 & -4 \times 10^{-4} & -2.5 \times 10^{-15} & 3.54 \times 10^{-15} & 3.86 \times 10^{-15} \\ -3.36 \times 10^{-4} & -0.023 & -4 \times 10^{-4} & -0.003 & -0.422 & -31.06 & 1.04 \times 10^{-14} & 1.1 \times 10^{-15} & 1.34 \times 10^{-14} \\ -3.51 \times 10^{-16} & -3.67 \times 10^{-16} & 2.51 \times 10^{-15} & 2.12 \times 10^{-15} & -3.62 \times 10^{-15} & -1.04 \times 10^{-14} & 31.08 & 0.52 & 0.48 \\ -2.84 \times 10^{-15} & -1.97 \times 10^{-15} & -3.54 \times 10^{-15} & -8.66 \times 10^{-17} & -3.37 \times 10^{-15} & -1.1 \times 10^{-14} & 0.52 & 32.05 & 31.07 \end{bmatrix} \tag{99}$$

D.2 Cases 1–6

$$\mathbf{W} = \begin{bmatrix} 579 & 0 & 0 & 0 & 0 & 0 & 0 & 0 & 0 \\ 0 & 137 & 0 & 0 & 0 & 0 & 0 & 0 & 0 \\ 0 & 0 & 149 & 0 & 0 & 0 & 0 & 0 & 0 \\ 0 & 0 & 0 & 479 & 0 & 0 & 0 & 0 & 0 \\ 0 & 0 & 0 & 0 & 127 & 0 & 0 & 0 & 0 \\ 0 & 0 & 0 & 0 & 0 & 119 & 0 & 0 & 0 \\ 0 & 0 & 0 & 0 & 0 & 0 & 191 & 0 & 0 \\ 0 & 0 & 0 & 0 & 0 & 0 & 0 & 67 & 0 \\ 0 & 0 & 0 & 0 & 0 & 0 & 0 & 0 & 67 \end{bmatrix} \tag{100}$$

$$\mathbf{L} = \begin{bmatrix} 23.38 & 0.32 & 0.01 & 3.6 & 0.065 & 0.0017 & 1.26 \times 10^{-17} & -3.42 \times 10^{-17} & 8.89 \times 10^{-18} \\ 0.32 & 11.4 & 0.5 & 0.065 & 1.83 & 0.07 & 8 \times 10^{-16} & -8.92 \times 10^{-17} & 5.2 \times 10^{-16} \\ -0.004 & -0.02 & -1.6 \times 10^{-4} & -15.88 & -0.19 & -6.6 \times 10^{-3} & -1.91 \times 10^{-17} & 1.07 \times 10^{-17} & 8.1 \times 10^{-17} \\ -0.021 & -0.024 & 0.016 & -0.181 & -8.2 & -0.42 & 3.53 \times 10^{-16} & -6.81 - 16 & 1.16 \times 10^{-15} \\ -5.75 & -0.06 & -2.1 \times 10^{-3} & 14.64 & 0.16 & 0.006 & 1.56 \times 10^{-17} & -2.02 \times 10^{-18} & -8.15 \times 10^{-17} \\ -0.06 & -2.78 & -0.14 & 0.16 & 7.57 & 0.4 & -5.41 \times 10^{-16} & 6.88 \times 10^{-16} & -1.26 \times 10^{-15} \\ -0.01 & -0.5 & -12.2 & -8.6 \times 10^{-4} & -0.023 & -1.1 \times 10^{-3} & 7.6 \times 10^{-16} & -7.74 \times 10^{-16} & -3.6 \times 10^{-15} \\ -9.5 \times 10^{-4} & -0.024 & -1.1 \times 10^{-3} & -6.7 \times 10^{-3} & -0.42 & -10.9 & -4.26 \times 10^{-16} & -3.3 \times 10^{-16} & 5 \times 10^{-15} \\ 1.04 \times 10^{-17} & 8.4 \times 10^{-16} & -7.6 \times 10^{-16} & 2 \times 10^{-17} & -2.9 \times 10^{-16} & 4.25 \times 10^{-16} & 13.85 & 0.42 & 0.35 \\ -3.3 \times 10^{-17} & -1.7 \times 10^{-16} & 7.8 \times 10^{-16} & -1.32 \times 10^{-17} & 6.7 \times 10^{-16} & 3.3 \times 10^{-16} & 0.42 & 9.12 & 8.2 \end{bmatrix} \tag{101}$$

D.3 Eigenvalue Analysis

This section discusses the eigenvalue analysis of the circular motion undertaken by the motor. The analysis was carried out by evaluating the **C**-matrix at every point of the programmed reference trajectory of the motor. This would help in evaluating the systems stability for different choices of tuning and gain matrices. The result of the analysis using the tuning (**W**) and gain matrices (**L**) given in the previous sections using the **C**-matrix at each point of the programmed motion trajectory is illustrated

in Figure 82. For the simplicity of understanding only the maximum value od the real part of each eigenvalue out all nine eigenvalues is plotted here. It is observed that for the tuning and gain matrices choice of section D.1 that resulted in oscillations on the estimated x and y positions (33 and 34) was due the positive real part of the eigenvalues. However, when the tuning matrices were properly chosen this defect was overcome as the resultant real part of the eigenvalues stayed negative throughout the programmed trajectory resulting in stable estimation of the state variables as evident from the results of Cases 1–6.

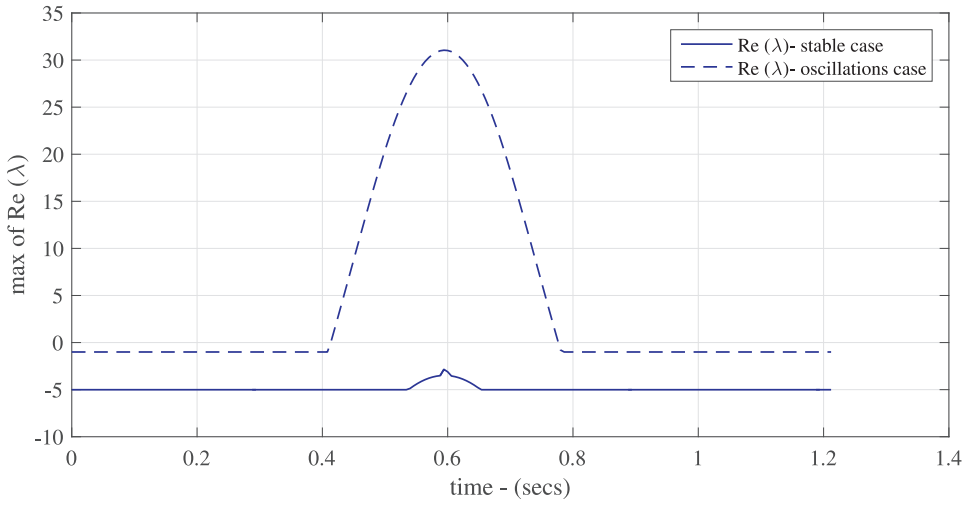

Figure 82: Eigenvalues analysis of oscillations versus stable case. For the simplicity of understanding only the maximum values of the real part of each eigenvalue out all nine eigenvalues is plotted here. It can be observed that for the oscillations case the real part of eigenvalues becomes positive momentarily and swing back to negative whereas for the stable case it stays negative throughout the motion.

D.4 Case 7

The **V** matrix for this case is an 8 x 8 identity matrix where the **W** is unchanged from the previous case. However, since the **C** and **V** have changed, the gain matrix is also different than the previous cases. The new gain matrix **k** of size 8 x 9 is given below:

$$\mathbf{L} = \begin{bmatrix} 23.98 & 0.33 & 0.01 & 2.06 & 0.027 & 9 \times 10^{-4} & 3.77 \times 10^{-17} & -5.2 \times 10^{-17} & 1.83 \times 10^{-16} \\ 0.33 & 11.68 & 0.51 & 0.027 & 1.07 & 0.051 & -1.47 \times 10^{-17} & -1.23 \times 10^{-16} & -1.3 \times 10^{-15} \\ 2.27 & 0.038 & 9.2 \times 10^{-4} & -21.81 & -0.34 & -9.82 \times 10^{-3} & -1.36 \times 10^{-17} & 6.55 \times 10^{-17} & 5.7 \times 10^{-17} \\ 0.038 & 1.11 & 0.044 & -0.34 & -11.25 & -0.49 & -8.69 \times 10^{-16} & -2.95 \times 10^{-16} & 2.14 \times 10^{-15} \\ -9.5 \times 10^{-3} & -0.51 & -12.2 & 1.9 \times 10^{-4} & 4.3 \times 10^{-3} & 1.2 \times 10^{-4} & -8.27 \times 10^{-16} & -1.95 \times 10^{-15} & 9.12 \times 10^{-16} \\ 2.12 \times 10^{-4} & 4.7 \times 10^{-3} & 1.9 \times 10^{-4} & -9.8 \times 10^{-3} & -0.49 & -10.9 & -2.55 \times 10^{-16} & -2.4 \times 10^{-15} & 1.1 \times 10^{-15} \\ 3.61 \times 10^{-17} & -1.13 \times 10^{-16} & 8.27 \times 10^{-16} & 1.64 \times 10^{-17} & 8.63 \times 10^{-16} & 2.55 \times 10^{-16} & 13.85 & 0.42 & 0.35 \\ -4.45 \times 10^{-17} & -1.56 \times 10^{-16} & -1.95 \times 10^{-15} & -6.9 \times 10^{-17} & 2.84 \times 10^{-16} & 2.4 \times 10^{-15} & 0.42 & 9.2 & 8.2 \end{bmatrix} \tag{102}$$

Corresponding eigenvalues of $\mathbf{A} - \mathbf{LC}$ and their plot are given below:

$$-24.05, -21.88, -13.81, -11.98 \pm 0.43j, -11.1 \pm 0.45, -8.2, -1.01 \tag{103}$$

APPENDIX E

TAG SUBMARINING DATA - REPEAT LAST MEASUREMENT

This appendix displays the graphs of the measured data of tag's submarining case where the last measured value of each quantity to be used for estimation is repeated in the duration of the link absence.

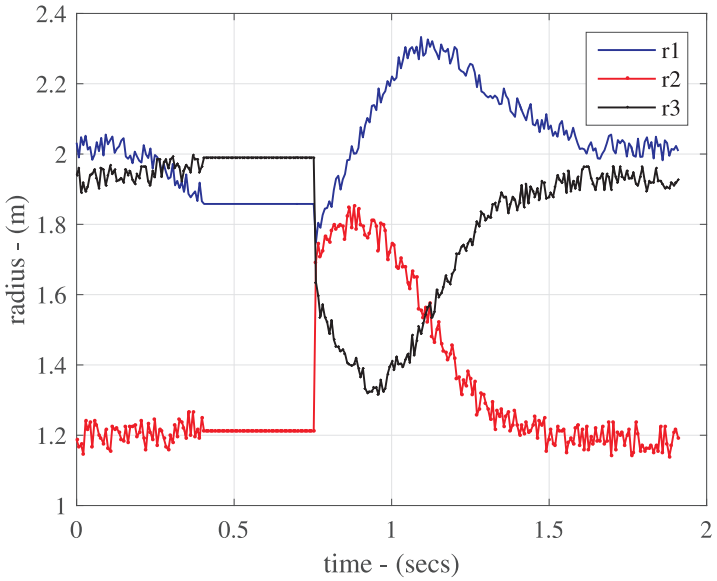

Figure 83: Radial distance with respect to each pylon in the absence of the RF link. The last measured radial distance valued, before the link loss, is repeated during the tag blockade.

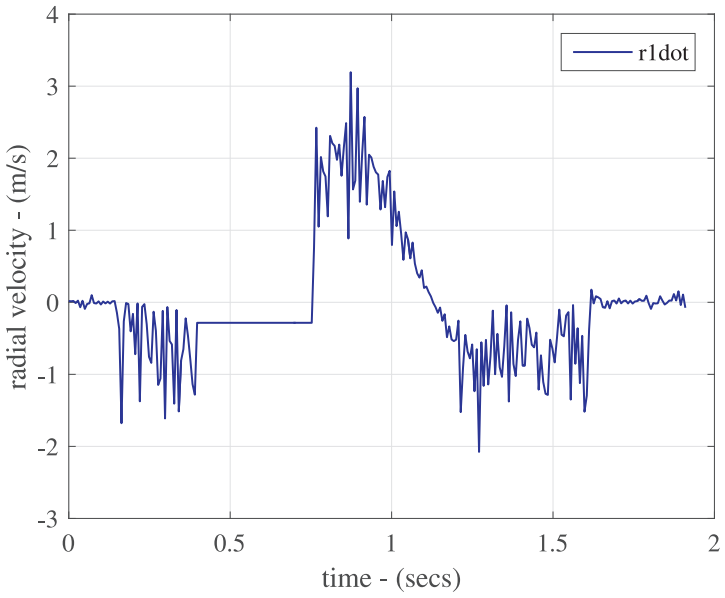

Figure 84: Radial velocity with respect to the first pylon.

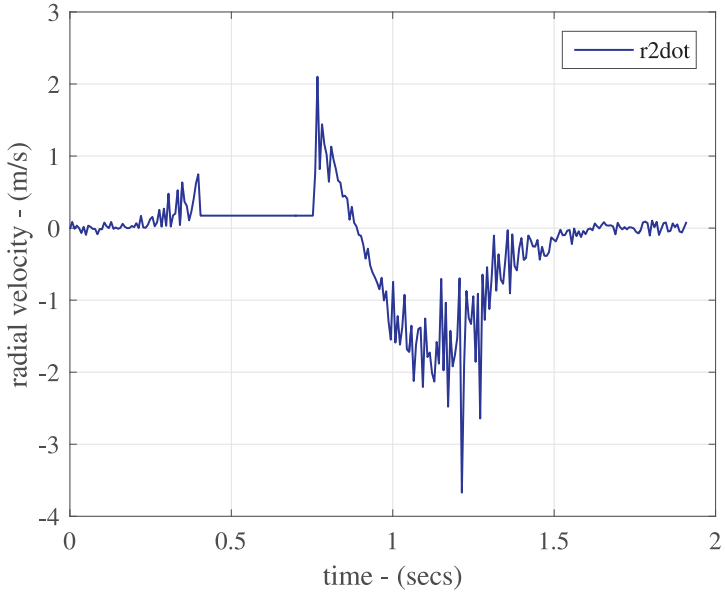

Figure 85: Radial velocity with respect to the second pylon.

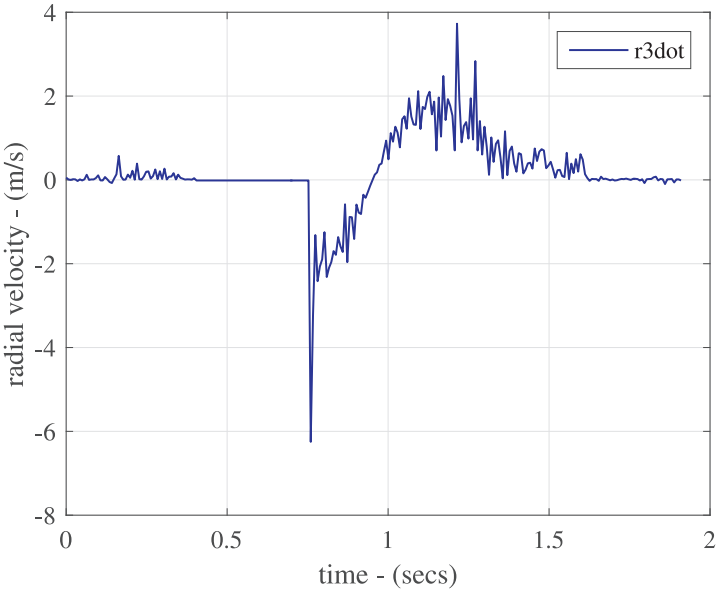

Figure 86: Radial velocity with respect to the third pylon.

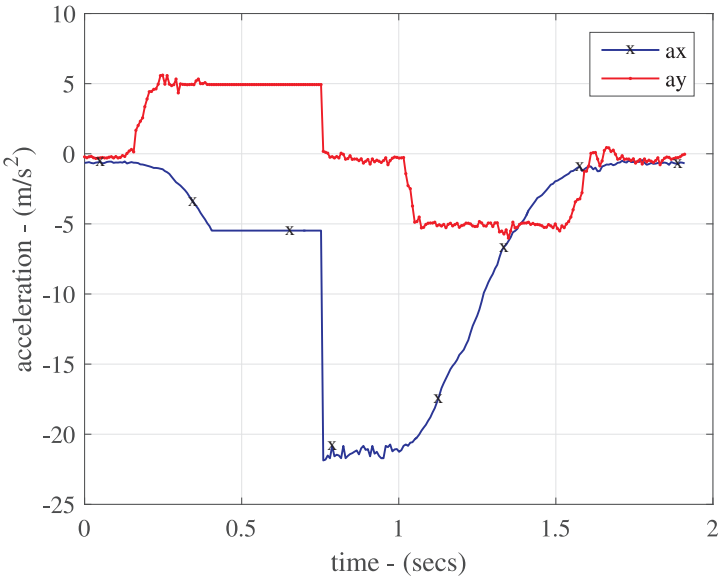

Figure 87: Measured linear acceleration of the tag from on board accelerometer during the circular motion.

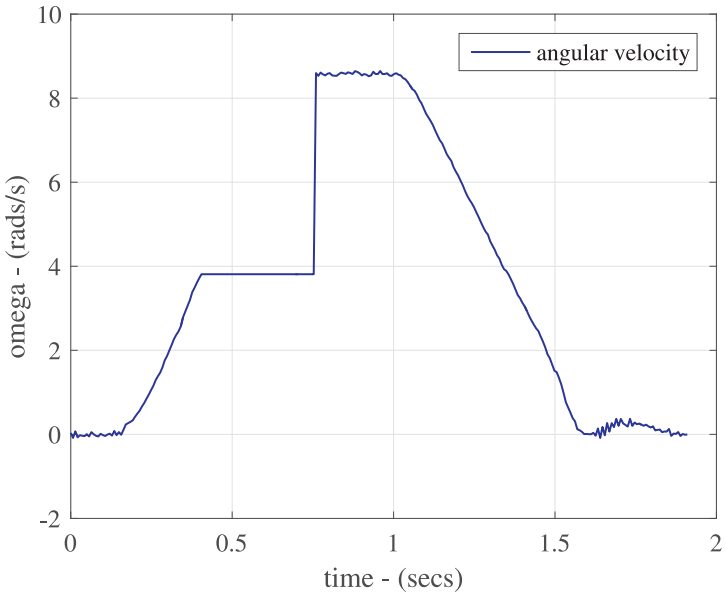

Figure 88: Measured angular velocity of the tag around tag's z-axis using on board gyroscope.

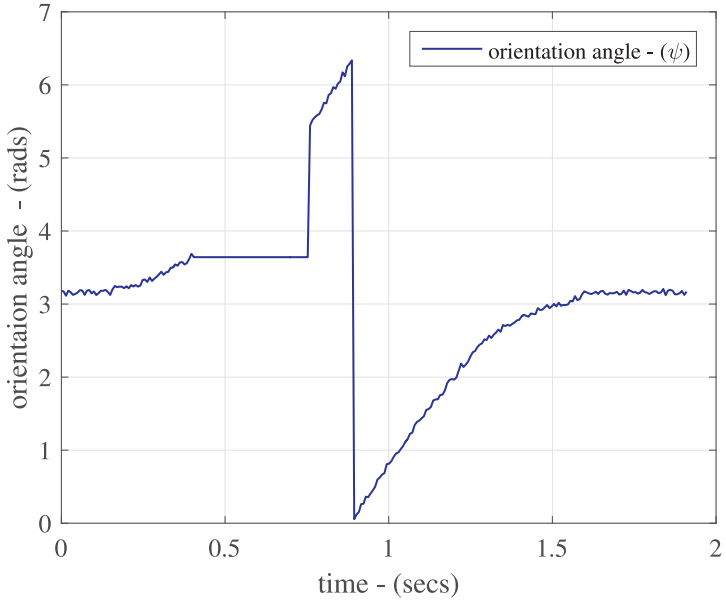

Figure 89: Tag orientation angle measured using on board compass.

APPENDIX F

TAG SUBMARINING - LINEAR INTERPOLATION

Measurements for Linear Interpolation

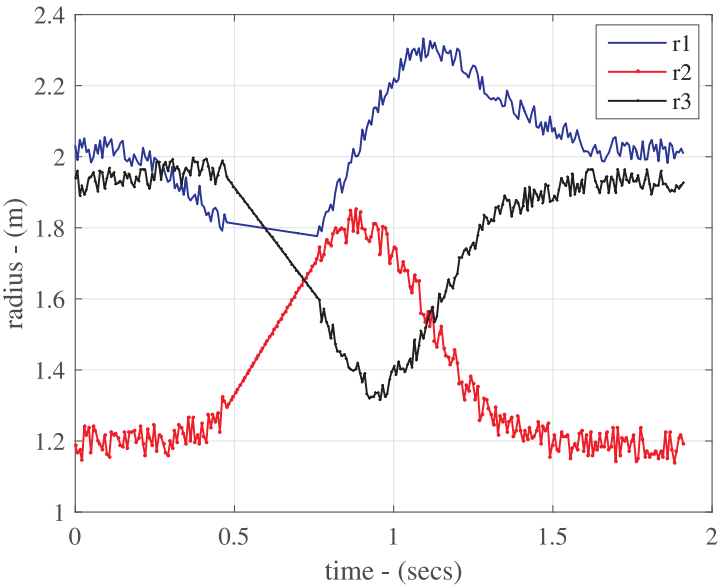

Figure 90: Radial distance with respect to each pylon in the absence of the RF link. The last measured radial distance valued, before the link loss, is repeated during the tag blockade.

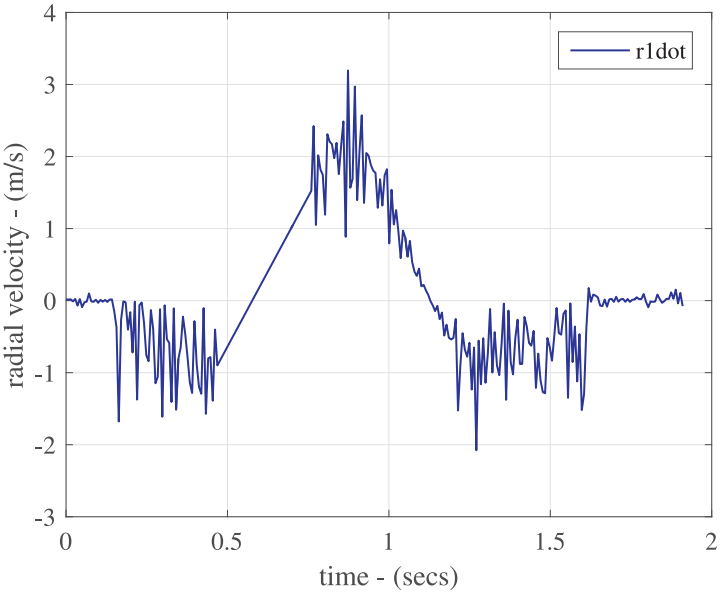

Figure 91: Radial velocity with respect to the first pylon.

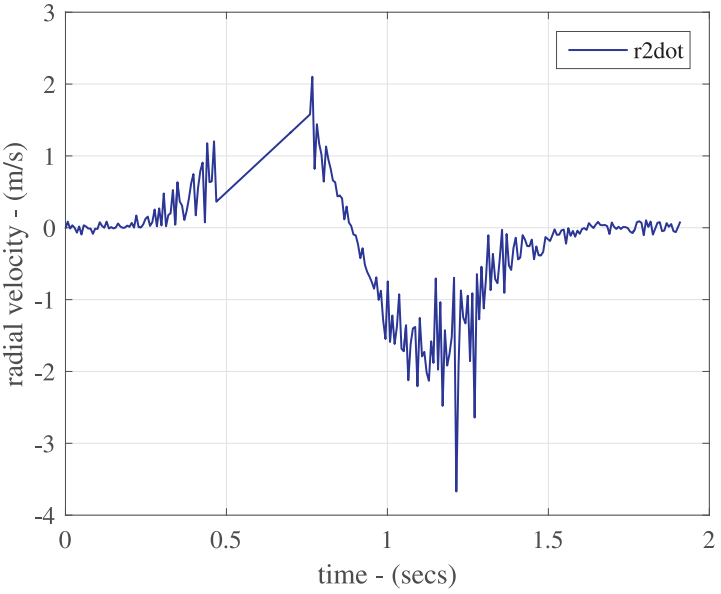

Figure 92: Radial velocity with respect to the second pylon.

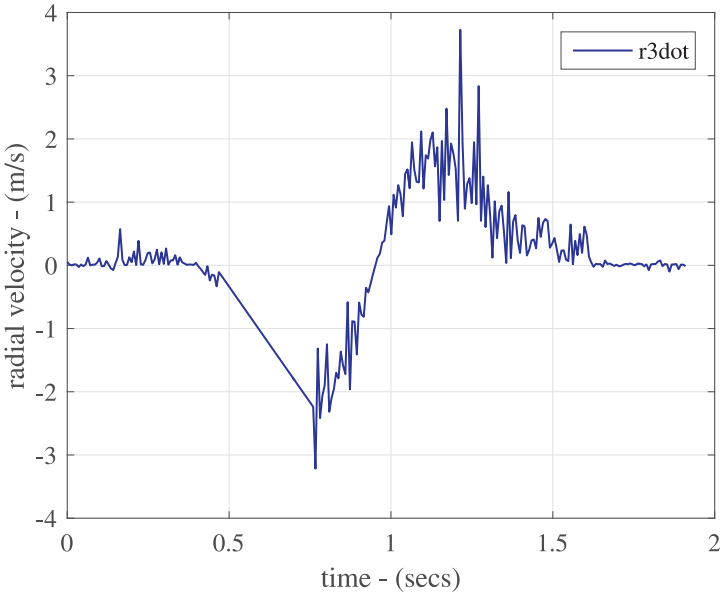

Figure 93: Radial velocity with respect to the third pylon.

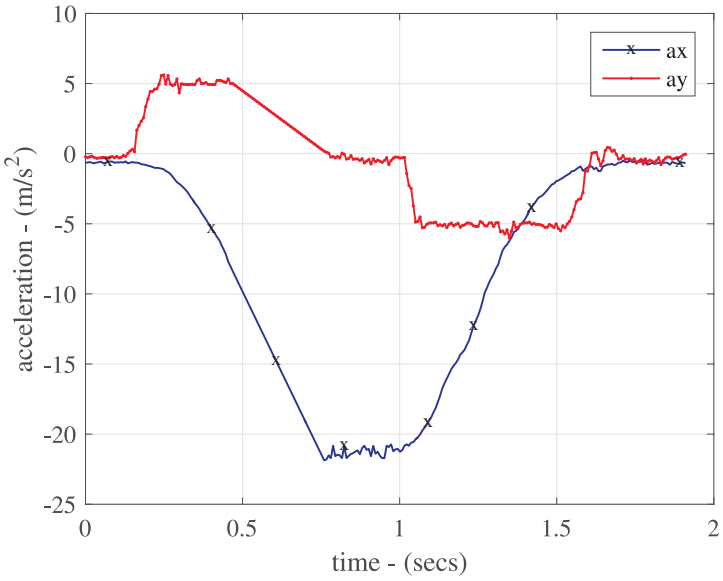

Figure 94: Measured linear acceleration of the tag from on board accelerometer during the circular motion.

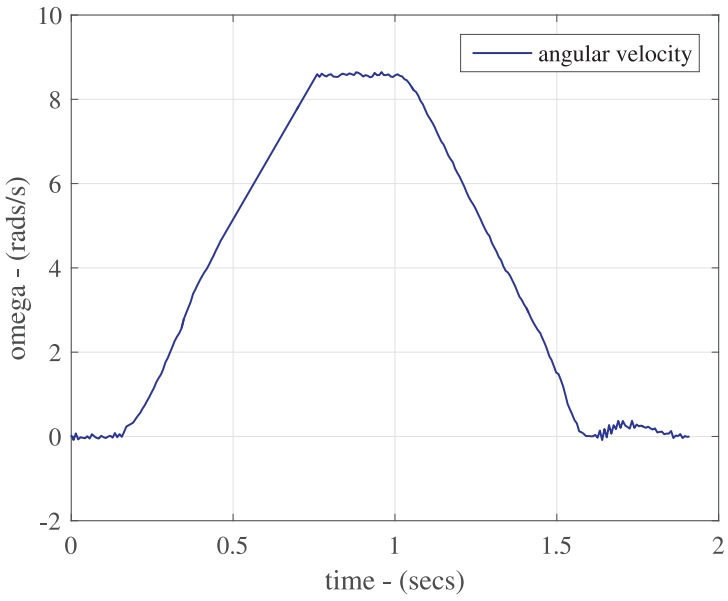

Figure 95: Measured angular velocity of the tag around tag's z-axis using on board gyroscope.

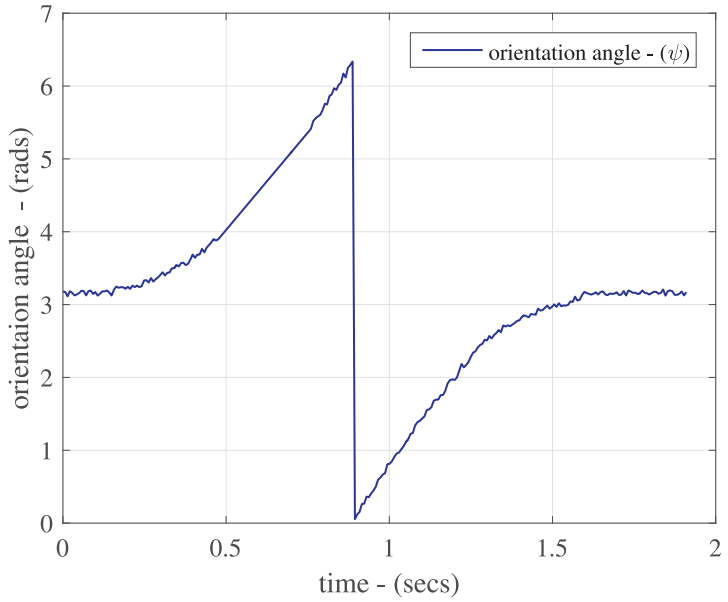

Figure 96: Tag orientation angle measured using on board compass.

REFERENCES

[1] S. A. R. Zekavat and R. M. Buehrer, *Handbook of Position Location: Theory, Practice, and Advances*, 1st ed. U.S.: Wiley and IEEE Press, 2012.

[2] J. E. A. Timothy Pratt, Charles W. Bostian, *Satellite Communications* , 2nd ed. U.S.: Wiley, 2003.

[3] L. Koski, T. Perala, and R. Piche, "Indoor positioning using wlan coverage area estimates," in *Indoor Positioning and Indoor Navigation (IPIN), 2010 International Conference on*, Sept 2010, pp. 1–7.

[4] K. Saneyoshi, "Drive assist system using stereo image recognition," in *Intelligent Vehicles Symposium, 1996., Proceedings of the 1996 IEEE*, Sep 1996, pp. 230–235.

[5] M. Richard, *Prociples of Modern Radar*, 2nd ed. U.S.: SciTech Publishing, 2010.

[6] M. Bouet and A. dos Santos, "RFID tags: Positioning principles and localization techniques," in *Wireless Days, 2008. WD '08. 1st IFIP*, 2008, pp. 1–5.

[7] J. Zhou and J. Shi, "RFID localization algorithms and applicationsa review," *Journal of Intelligent Manufacturing, Springer Link*, vol. 20, pp. 695–707, December 2009.

[8] D. Macagnano, G. Destino, and G. Abreu, "A comprehensive tutorial on localization: Algorithms and performance analysis tools," *International Journal of Wireless Information Networks*, vol. 19, pp. 290–314, December 2012.

[9] R. Want, A. Hopper, V. Falco, and J. Gibbons, "The active badge location system," *ACM Transactions on Information Systems*, vol. 10, no. 1, pp. 91–102, 1992.

[10] A. Ward, A. Jones, and A. Hopper, "A new location technique for the active office," *Personal Communications, IEEE*, vol. 4, no. 5, pp. 42–47, 1997.

[11] N. B. Priyantha, C. Anit, and H. Balakrishnan, "The cricket location-support system," in *Mobile Computing and Networking, 6th ACM International Conference on*, August, 2000.

[12] X. Liu, J. Peng, and T. Liu, "A novel indoor localization system based on passive RFID technology," in *Electronic and Mechanical Engineering and Information Technology (EMEIT), 2011 International Conference on*, vol. 8, 2011, pp. 4285–4288.

[13] S. Park and S. Hashimoto, "An intelligent localization algorithm using read time of RFID system," *Advanced Engineering Informatics, Elsevier*, vol. 24, no. 4, pp. 490–497, 2010.

[14] D. Boontrai, T. Jingwangsa, and P. Cherntanomwong, "Indoor localization technique using passive RFID tags," in *Communications and Information Technology, 2009. ISCIT 2009. 9th International Symposium on*, 2009, pp. 922–926.

[15] M. Bouet and G. Pujolle, "L-virt: Range-free 3-d localization of RFID tags based on topological constraints," *Computer Communications, Elsevier*, vol. 32, p. 14851494, 2009.

[16] Y. Zhao, Y. Liu, and L. Ni, "Vire: Active RFID-based localization using virtual reference elimination," in *Parallel Processing, 2007. ICPP 2007. International Conference on*, 2007, pp. 56–56.

[17] L. Ni, Y. Liu, Y. C. Lau, and A. Patil, "Landmarc: indoor location sensing using active RFID," in *Pervasive Computing and Communications, 2003. (PerCom 2003). Proceedings of the First IEEE International Conference on*, 2003, pp. 407–415.

[18] S. Soonjun, D. Boontri, and P. Cherntanomwong, "A novel approach of RFID based indoor localization using fingerprinting techniques," in *Communications, 2009. APCC 2009. 15th Asia-Pacific Conference on*, 2009, pp. 475–478.

[19] J. S. Choi, B. R. Son, H. K. Kang, and D. H. Lee, "Indoor localization of unmanned aerial vehicle based on passive UHF RFID systems," in *Ubiquitous Robots and Ambient Intelligence (URAI), 2012 9th International Conference on*, 2012, pp. 188–189.

[20] J. Hightower, R. Want, and G. Borriello, "Spoton: An indoor 3d location sensing technology based on rf signal strength," *UW CSE Technical Report 2000-02-02*, 2000.

[21] A. Bekkali and M. Matsumoto, "RFID indoor tracking based on inter-tags distance measurement," in *Wireless Telecommunications Symposium, 2007. WTS 2007*, 2007, pp. 1–1.

[22] Y. Zhang, M. G. Amin, and S. Kaushik, "Localization and tracking of passive rfid tags based on direction estimation," *International Journal of Antennas and Propagation, Hindawi Publishing Corporation*, vol. 2007, 2007.

[23] T. Nick, J. Gotze, W. John, and G. Stoenner, "Localization of UHF RFID labels with reference tags and unscented kalman filter," in *RFID-Technologies and Applications (RFID-TA), 2011 IEEE International Conference on*, 2011, pp. 168–173.

[24] D. Lieckfeldt, J. You, and D. Timmermann, "Exploiting rf-scatter: Human localization with bistatic passive UHF RFID-systems," in *Wireless and Mobile Computing, Networking and Communications, 2009. WIMOB 2009. IEEE International Conference on*, 2009, pp. 179–184.

[25] X. Li, Y. Zhang, and M. Amin, "Multifrequency-based range estimation of RFID tags," in *RFID, 2009 IEEE International Conference on*, 2009, pp. 147–154.

[26] C.-H. Ko, "RFID 3d location sensing algorithms," *Automation in Construction, Elsevier*, vol. 19, no. 5, p. 588595, August, 2010.

[27] P. Kamol, S. Nikolaidis, R. Ueda, and T. Arai, "RFID based object localization system using ceiling cameras with particle filter," in *Future Generation Communication and Networking (FGCN 2007)*, vol. 2, 2007, pp. 37–42.

[28] E. DiGiampaolo and F. Martinelli, "Mobile robot localization using the phase of passive UHF RFID signals," *Industrial Electronics, IEEE Transactions on*, vol. 61, no. 1, pp. 365–376, 2014.

[29] H. Wang, G. Bauer, F. Kirsch, and M. Vossiek, "Hybrid RFID system-based pedestrian localization: A case study," in *Positioning Navigation and Communication (WPNC), 2013 10th Workshop on*, 2013, pp. 1–6.

[30] A. Papapostolou and H. Chaouchi, "Simulation-based analysis for a heterogeneous indoor localization scheme," in *Consumer Communications and Networking Conference (CCNC), 2010 7th IEEE*, 2010, pp. 1–5.

[31] A. Ruiz, F. Granja, J. Honorato, and J. Rosas, "Pedestrian indoor navigation by aiding a foot-mounted IMU with RFID signal strength measurements," in *Indoor Positioning and Indoor Navigation (IPIN), 2010 International Conference on*, 2010, pp. 1–7.

[32] Y. Zhou and W. Liu, "Preliminary research on indoor mobile robot localization using laser-activated RFID," in *RFID, 2007. IEEE International Conference on*, 2007, pp. 78–85.

[33] R. Miesen, F. Kirsch, and M. Vossiek, "UHF RFID localization based on synthetic apertures," *Automation Science and Engineering, IEEE Transactions on*, vol. 10, no. 3, pp. 807–815, 2013.

[34] P. Nikitin, R. Martinez, S. Ramamurthy, H. Leland, G. Spiess, and K. V. S. Rao, "Phase based spatial identification of uhf RFID tags," in *RFID, 2010 IEEE International Conference on*, 2010, pp. 102–109.

[35] R. Miesen, F. Kirsch, and M. Vossiek, "Holographic localization of passive UHF RFID transponders," in *RFID (RFID), 2011 IEEE International Conference on*, 2011, pp. 32–37.

[36] V. Viikari, P. Pursula, and K. Jaakkola, "Ranging of UHF RFID tag using stepped frequency read-out," *Sensors Journal, IEEE*, vol. 10, no. 9, pp. 1535–1539, 2010.

[37] C. Hekimian-Williams, B. Grant, X. Liu, Z. Zhang, and P. Kumar, "Accurate localization of RFID tags using phase difference," in *RFID, 2010 IEEE International Conference on*, 2010, pp. 89–96.

[38] A. Parr, R. Miesen, F. Kirsch, and M. Vossiek, "A novel method for UHF RFID tag tracking based on acceleration data," in *RFID (RFID), 2012 IEEE International Conference on*, 2012, pp. 110–115.

[39] B.-S. Choi, J.-W. Lee, and J.-J. Lee, "An improved localization system with RFID technology for a mobile robot," in *Industrial Electronics, 2008. IECON 2008. 34th Annual Conference of IEEE*, 2008, pp. 3409–3413.

[40] S. Shao and R. Burkholder, "Passive UHF RFID tag localization using reader antenna spatial diversity," in *Wireless Information Technology and Systems (ICWITS), 2012 IEEE International Conference on*, 2012, pp. 1–4.

[41] K.-C. Lee, A. Oka, E. Pollakis, and L. Lampe, "A comparison between unscented kalman filtering and particle filtering for rssi-based tracking," in *Positioning Navigation and Communication (WPNC), 2010 7th Workshop on*, 2010, pp. 157–163.

[42] T. Nick, J. Goetze, W. John, and G. Stoenner, "Comparison of extended and unscented kalman filter for localization of passive uhf RFID labels," in *General Assembly and Scientific Symposium, 2011 XXXth URSI*, 2011, pp. 1–4.

[43] D. Hahnel, W. Burgard, D. Fox, K. Fishkin, and M. Philipose, "Mapping and localization with RFID technology," in *Robotics and Automation, 2004. Proceedings. ICRA '04. 2004 IEEE International Conference on*, vol. 1, 2004, pp. 1015–1020 Vol.1.

[44] A. Papapostolou and H. Chaouchi, "RFID-assisted indoor localization and the impact of interference on its performance," *Journal of Network and Computer Applications, Elsevier*, vol. 34, no. 3, pp. 902–913, May 2011.

[45] T. Sanpechuda and L. Kovavisaruch, "A review of RFID localization: Applications and techniques," in *Electrical Engineering/Electronics, Computer, Telecommunications and Information Technology, 2008. ECTI-CON 2008. 5th International Conference on*, vol. 2, 2008, pp. 769–772.

[46] A. Bouzakis and L. Overmeyer, "RFID tag positioning with the aid of an active electronically-steered array," in *Personal Indoor and Mobile Radio Communications (PIMRC), 2012 IEEE 23rd International Symposium on*, 2012, pp. 2483–2488.

[47] M. B. Akbar, D. G. Taylor, and G. D. Durgin, "Amplitude and phase difference estimation bounds for multisensor based tracking of RFID tags," in *IEEE International Conference on RFID*, April 2015, pp. 105–112.

[48] ——, "Hybrid inertial microwave reflectometry for mm-scale tracking in RFID systems," *IEEE Transactions on Wireless Communications*, vol. 14, no. 12, pp. 6805–6814, Dec 2015.

[49] H. Liu, H. Darabi, P. Banerjee, and J. Liu, "Survey of wireless indoor positioning techniques and systems," *Systems, Man, and Cybernetics, Part C: Applications and Reviews, IEEE Transactions on*, vol. 37, no. 6, pp. 1067–1080, Nov 2007.

[50] D. Arumugam, J. Griffin, and D. Stancil, "Experimental demonstration of complex image theory and application to position measurement," *Antennas and Wireless Propagation Letters, IEEE*, vol. 10, pp. 282–285, 2011.

[51] Microsoft, *X-box Kinect*, 1st ed. U.S.: Microsoft, 2011.

[52] F. Raab, E. Blood, T. Steiner, and H. Jones, "Magnetic position and orientation tracking system," *Aerospace and Electronic Systems, IEEE Transactions on*, vol. AES-15, no. 5, pp. 709–718, Sept 1979.

[53] P. Gulden, S. Roehr, and M. Christmann, "An overview of wireless local positioning system configurations," in *Wireless Sensing, Local Positioning, and RFID, 2009. IMWS 2009. IEEE MTT-S International Microwave Workshop on*, Sept 2009, pp. 1–4.

[54] D. M. Dobkin, *The RF in RFID, UHF RFID in Practice*, 2nd ed. U.S.: Newnes, 2012.

[55] S. Blackman and R. Popoli, *Design and analysis of modern tracking systems*. Wiley, 2012.

[56] G. Donald and S. Novak, "RFID Tags / Planar Inductors as Chemical Sensor Platforms in Liquid Sensing Applications," *Master's Thesis, Marquette University*, December 2009.

[57] B. R. Marshall, G. D. Durgin, and A. J. Kirsch, *Wireless Wearable Moisture Sensor Final Report*. Propagation Group, ECE, Georgia Institute of Technolgy, Atlanta, 2013.

[58] M. B. Akbar, "Design and prototype development of motion and shock sensing RF tags," *Master's Thesis, Georgia Institute of Technology, Atlanta, https://smartech.gatech.edu/handle/1853/43666*, May 2012.

[59] A. Bekkali, H. Sanson, and M. Matsumoto, "RFID indoor positioning based on probabilistic RFID map and Kalman filtering," in *Third IEEE International Conference on Wireless and Mobile Computing, Networking and Communications*, 2007, pp. 21–21.

[60] S. House, S. Connell, I. Milligan, D. Austin, T. Hayes, and P. Chiang, "Indoor localization using pedestrian dead reckoning updated with RFID-based fiducials," in *Annual International Conference of the IEEE Engineering in Medicine and Biology Society,*, 2011, pp. 7598–7601.

[61] S. Sarkka, V. Viikari, M. Huusko, and K. Jaakkola, "Phase-Based UHF RFID tracking With nonlinear Kalman filtering and smoothing," *IEEE Sensors Journal,*, vol. 12, no. 5, pp. 904–910, 2012.

[62] D.-B. Shin, G. young Choi, and D.-Y. Kim, "Design and implementation of wireless sensing platform based on UHF RFID technology," in *Digest of Technical Papers International Conference on Consumer Electronics (ICCE),*, Jan 2010, pp. 297–298.

[63] L. Catarinucci, R. Colella, and L. Tarricone, "Sensor data transmission through passive RFID tags to feed wireless sensor networks," in *IEEE MTT-S International Microwave Symposium Digest (MTT),*, May 2010, pp. 1772–1775.

[64] J. Mitsugi, H. Hada, T. Inaba, K. Ihara, G. Kojima, and T. Kondo, "Enabling globally unique sensor id with dual-interface RF tag," in *IEEE Sensors,*, Oct 2011, pp. 1628–1631.

[65] P. Kalansuriya, R. Bhattacharyya, and s. sarma, "A novel communication method for semi-passive RFID based sensors," in *IEEE International Conference on Communications (ICC),*, June 2014, pp. 5902–5907.

[66] J. Griffin and G. Durgin, "Complete link budgets for backscatter-radio and RFID systems," *Antennas and Propagation Magazine, IEEE*, vol. 51, no. 2, pp. 11–25, 2009.

[67] J. P. Hespanha, *Linear System Theory*. U.S.: Princeton University Press, 2009.

[68] T. F. Bechteler and H. Yenigun, "2-D localization and identification based on SAW ID-tags at 2.5 ghz," *IEEE Transactions on Microwave Theory and Techniques*, vol. 51, no. 5, pp. 1584–1590, May 2003.

[69] V. P. Munishwar, S. Singh, X. Wang, C. Mitchell, K. Gopalan, and N. B. Abu-Ghazaleh, "On the accuracy of RFID-based localization in a mobile wireless network testbed," in *IEEE International Conference on Pervasive Computing and Communications*, March 2009, pp. 1–6.

[70] M. Scherhaufl, M. Pichler, and A. Stelzer, "UHF RFID localization based on phase evaluation of passive tag arrays," *IEEE Transactions on Instrumentation and Measurement*, vol. 64, no. 4, pp. 913–922, April 2015.

[71] M. Scherhufl, M. Pichler, E. Schimbck, D. J. Mller, A. Ziroff, and A. Stelzer, "Indoor localization of passive UHF RFID tags based on phase-of-arrival evaluation," *IEEE Transactions on Microwave Theory and Techniques*, vol. 61, no. 12, pp. 4724–4729, Dec 2013.

[72] F. H. Raab, "Quasi-static magnetic-field technique for determining position and orientation," *IEEE Transactions on Geoscience and Remote Sensing*, vol. GE-19, no. 4, pp. 235–243, Oct 1981.

[73] D. D. Arumugam, J. D. Griffin, and D. D. Stancil, "Experimental demonstration of complex image theory and application to position measurement," *IEEE Antennas and Wireless Propagation Letters*, vol. 10, pp. 282–285, April 2011.

[74] D. D. Arumugam, J. D. Griffin, D. D. Stancil, and D. S. Ricketts, "Two-dimensional position measurement using magnetoquasistatic fields," in *IEEE-APS Topical Conference on Antennas and Propagation in Wireless Communications*, Sept 2011, pp. 1193–1196.

[75] ——, "Three-dimensional position and orientation measurements using magneto-quasistatic fields and complex image theory [measurements corner]," *IEEE Antennas and Propagation Magazine*, vol. 56, no. 1, pp. 160–173, Feb 2014.

[76] R. Miesen, F. Kirsch, and M. Vossiek, "UHF RFID localization based on synthetic apertures," *IEEE Transactions on Automation Science and Engineering*, vol. 10, no. 3, pp. 807–815, July 2013.

[77] G. Durgin, C. Valenta, M. Akbar, M. Morys, B. Marshall, and Y. Lu, "Modulation and sensitivity limits for backscatter receivers," in *IEEE International Conference on RFID,*, Apr. 2013, pp. 124–130.

[78] J. Primbs, "Survey of nonlinear observer design techniques," *Penn State Notes*, vol. 1, no. 1, pp. 1–18, Jan 1996.

[79] S. R. Kou, D. L. Elliott, and T. J. Tarn, "Exponential observers for nonlinear dynamic systems," *Information and Control (Elsevier)*, vol. 29, no. 3, pp. 204–216, November 1975.

[80] W. Baumann and W. Rugh, "Feedback control of nonlinear systems by extended linearization," *IEEE Transactions on Automatic Control*, vol. 31, no. 1, pp. 40–46, Jan 1986.

[81] H. Keller, "Nonlinear observer design by transformation into a generalized observer canonical form," *International Journal of Control*, vol. 46, no. 6, pp. 1915–1930, 1987.

[82] D. Taylor, "Design of nonlinear least-squares velocity estimation algorithms for automotive vehicles," in *49th IEEE Conference on Decision and Control (CDC),*, Dec 2010, pp. 6409–6414.

[83] A. Isidori, *Nonlinear Control Systems*. U.S.: Springer-Verlag, 1995.

[84] M. Vidyasagar, *Nonlinear Systems Analysis*, 2nd ed. U.S.: Prentice Hall, 1993.

[85] M. B. Akbar, Q. Cheng, M. Alhassoun, and G. D. Durgin, "Orientation sensing using backscattered phase from Multi-Antenna tag at 5.8 GHz," in *IEEE International Conference on RFID*, May 2016, pp. 237–244.

[86] M. B. Akbar, F. Amato, A. Claessen, and G. D. Durgin, "Broadband backscatter based technique to identify the presence of skimming electronics on payment terminals," in *2016 IEEE Radio and Wireless Symposium (RWS)*, Jan 2016, pp. 141–144.

[87] F. Amato, C. W. Peterson, M. B. Akbar, and G. D. Durgin, "Long range and low powered RFID tags with tunnel diode," in *RFID Technology and Applications (RFID-TA), 2015 IEEE International Conference on*, Sept 2015, pp. 182–187.

[88] P. Yang, W. Wu, M. Moniri, and C. Chibelushi, "Efficient object localization using sparsely distributed passive RFID tags," *IEEE Transactions on Industrial Electronics*, vol. 60, no. 12, pp. 5914–5924, Dec 2013.

[89] X. Shi, Z. Yang, and J. Chen, "Localization accuracy of range-only sensors with additive and multiplicative noise," in *IEEE Global Communications Conference (GLOBECOM)*, Dec 2013, pp. 195–200.

[90] S. M. Kay, *Fundamental of Statistical Signal Processing: Estimation Theory*, 1st ed. Prentice Hall, 1993.

[91] H. Van Trees and K. L. Bell, *Bayesian Bounds for Parameter Estimation and Nonlinear Filtering/Tracking*, 1st ed. Wiley-IEEE Press, 2007.

[92] D. Dardari, M. Luise, and E. Falletti, *Satellite and Terrestrial Radio Positioning Techniques*, 1st ed. Elsevier, 2012.

[93] H. Peksen, "Performance analysis of signal-to-noise ratio estimates for additive white gaussian noise and time-selective fading channels," Master's thesis, School of Electrical and Computer Engineering, Texas A&M University, 2008.

[94] L. Seidman, "Performance limitations and error calculations for parameter estimation," *Proceedings of the IEEE*, vol. 58, no. 5, pp. 644–652, May 1970.

[95] A. Stuart, *Kendall's Advanced Theory of Statistics*, 3rd ed. Wiley, 2010.

[96] N. Patwari, J. Ash, S. Kyperountas, A. Hero, R. Moses, and N. Correal, "Locating the nodes: cooperative localization in wireless sensor networks," *IEEE Signal Processing Magazine*, vol. 22, no. 4, pp. 54–69, July 2005.

[97] T. Nick and J. Gotze, "Posterior cramer-rao lower bounds of RFID localization," in *20th International Conference on Software, Telecommunications and Computer Networks (SoftCOM),*, Sept 2012, pp. 1–6.

[98] X. Zheng, H. Liu, J. Yang, Y. Chen, R. Martin, and X. Li, "A study of localization accuracy using multiple frequencies and powers," *IEEE Transactions on Parallel and Distributed Systems,*, vol. 25, no. 8, pp. 1955–1965, Aug 2014.

[99] X. Zhang, C. Tepedelenlioglu, M. Banavar, and A. Spanias, "Crlb for the localization error in the presence of fading," in *IEEE International Conference on Acoustics, Speech and Signal Processing (ICASSP),*, May 2013, pp. 5150–5154.

[100] H. Godrich, A. Haimovich, and R. Blum, "Cramer rao bound on target localization estimation in MIMO radar systems," in *42nd Annual Conference on Information Sciences and Systems,*, March 2008, pp. 134–139.

[101] J. Sijbers and A. J. D. Dekker, "Maximum likelihood estimation of signal amplitude and noise variance from MR data," *Magnetic Resonance in Medicine*, vol. 51, no. 3, pp. 586–594, 2004.

[102] A. Papoulis and S. U. Pillai, *Probability, Random Variables and Stochastic Processes*, 4th ed. McGraw-Hill, 2002.

[103] G. D. Durgin, *Space Time Wireless Channels*, 1st ed. Prentice Hall, 2002.

[104] B. P. Lathi and Z. Ding, *Modern Digital and Analog Communication Systems*, 4th ed. Oxford University Press, 2009.

[105] H. Gudbjartsson and S. Patz, "The rician distribution of noisy MRI data," *Magnetic Resonance in Medicine*, vol. 34, no. 6, pp. 910–914, 1995.

[106] G. Casella and R. L. Berger, *Statistical Inference*, 2nd ed. Thomson Learning, 2002.

[107] H. Cramer, *Mathematical Methods of Statistics*, 1st ed. Princeton University Press, 1999.